1-1-2017

Fundamental Investigation Of The Electrocatalytic Activity Of Layered Mixed Metal Oxides For Low Temperature Oxygen Electrocatalysis

Ayad M. Nacy
Wayne State University,

FUNDAMENTAL INVESTIGATION OF THE ELECTROCATALYTIC ACTIVITY OF LAYERED MIXED METAL OXIDES FOR LOW TEMPERATURE OXYGEN ELECTROCATALYSIS

by

AYAD M. NACY

DISSERTATION

Submitted to the Graduate School

of Wayne State University

Detroit, Michigan

in partial fulfillment of the requirements

for the degree of

DOCTOR OF PHILOSOPHY

2017

MAJOR: CHEMICAL ENGINEERING

Approved By:

_____

Advisor Date

_____

_____

_____

DEDICATION

To my late father Manhal Nacy

My lovely mother – Hanaa Nacy

My wonderful aunt – Lilian Nacy

My sisters – Tamara and Ban Nacy

And to all my family and all my friends

ACKNOWLEDGEMENTS

I would like to thank my advisor Dr. Eranda Nikolla whom for without her patience, guidance and understanding, I wouldn't have made it this far. Her knowledge in catalysis, reaction design and electrochemistry was a consistent nourishment to my research. Dr. Nikolla have continually conveyed the spirit of excitement and passion in regard to teaching and scientific innovation.

I would also like to thank my committee members: Prof. Charles Manke, Prof. Sandro da Rocha and Prof. Stephanie L. Brock for the friendly guidance, constructive suggestions and their valuable time serving on my committee.

Many thanks go to the staff and faculty of the Chemical Engineering and Materials Science department at Wayne State University for providing a comfortable environment to work and study at. I also send many thanks to the current department chair Dr. Mao for providing me with advice and guidance throughout my study. I would like to thank Dr. Zhi Mei at Lumigen Instrument Center, Department of Chemistry for his help and training on the scanning electron microscopy. I would also like to thank Dr. Kai Sun at University of Michigan for his help in collecting high-resolution transmission electron microscopy images.

I would like to thank all my friends and colleagues, who have enriched my journey with joy and scientific discussions, Doctors-to-be Juliana Carniero, Bingwen Wang, Mohamad Soroush Barhaghi, Ümit Özer and Samji Samira. Special thanks go to brilliant undergraduate students that I've had the chance to work with. I would like to thank Suzana Meira for her help in optimizing the thin film deposition for rotating disk electrode studies and cathode preparation for battery studies. I would like to thank Mariana de Souza for her help in synthesizing different catalyst presented in this study. I would also like to thank Monty Diaz for her help in catalyst synthesis,

cathode preparation and battery testing. I would also like to acknowledge all the hard work John Carl Camayang provided for the last part of this thesis, and wish him all the luck on his studies.

I can't appreciate enough the endless support and scientific discussion Dr. Layan Savithra have provided me during my study, he was more like a brother to me than a friend. I would also like to thank the postdoctoral fellows in Prof. Nikolla's group, Dr. Asha Hitihami Mudiyanselage, Dr. Anirban Das and Dr. Xiangkui Gu.

I would like to express my gratitude to my friends for their support during my study, Shawn Shaheen, Sarmed Najim, Bashar Danial, Nenos Akther, Fadi Sabah, Joseph Shaheen and Alex Najim, they have been my family here in Michigan. I will never forget about all the efforts my friends Bakir Ali and Mustafa Nameer had to put in to help my parents in Iraq during the good and the bad times, and for them I will be in debt forever.

I would also like to thank my family in Texas, uncle Sameer Al-Jazrawi and his family, Bassam Al-Jazrawi and his family, Loreen Nacy, my cousin Diana Nacy and her husband Omar Jawdat and would like to congratulate them on their new family member, my cousin Jasmin Nacy and her husband Mossa, and my little cousin Leena Nacy for all their support, love and good time.

I can never forget the unconditional love, support and inspiration my late father had provided me throughout my entire life and especially during my graduate study. Dad, I love you so much, you will always be my hero. I would also like to thank both my sisters Tamara and Ban Nacy for their love, support and good times. Last but not least, I would like express my gratitude to both my mother Hanaa Nacy and my aunt Lilian Nacy. Thank you for being the most effective pain-reliever throughout my entire life.

TABLE OF CONTENTS

DEDICATION ii

ACKNOWLEDGEMENTS iii

LIST OF TABLES xi

LIST OF FIGURES xii

CHAPTER 1. INTRODUCTION 1

1.1. Summary 1

1.2. Global Warming and Energy Utilization 1

1.3. Energy Storage: Batteries 4

1.4. Electrochemistry of Li-air Batteries 7

1.5. Scope of the Thesis 10

CHAPTER 2. BACKGROUND AND LITERATURE REVIEW 14

2.1. Summary 14

2.2. Introduction 14

2.3. Oxygen Electrocatalysis in Metal-Air Batteries 15

2.4. ORR Electrocatalysis in alkaline media for Fuel Cells 19

2.4.1. Platinum and Platinum Alloy Catalysts 19

2.4.2. Carbon-Based Catalysts 21

2.4.3. Transition Metal Oxides 22

2.4.4. Perovskites 23

2.4.5. First-series Ruddlesden-Popper oxides 25

CHAPTER 3. EXPERIMENTAL TECHNIQUES 28

3.1. Summary 28

3.2. Synthesis and Reactor Design 28

3.2.1. Reverse-Microemulsion Synthesis 28

3.2.2. Cathode Fabrication for Li-O_2 Battery 30

3.2.3. Battery Design and Assembly 30

3.2.4. Thin-Film preparation for Rotating Disk Voltammetry Studies 32

3.2.5. Rotating Disk Electrochemical Cell Design 33

3.3. Structural and Physical Characterization 34

3.3.1. X-Ray Diffraction (XRD) 34

3.3.2. Field Emission Scanning Electron Microscopy (FESEM) and Energy Dispersive Spectroscopy (EDS) 35

3.3.3. X-ray Photoelectron Spectroscopy (XPS) 36

3.3.4. Scanning Transmission Electron Microscopy (STEM) and Transmission Electron Microscopy (TEM) 38

3.3.5. Electron Energy Loss Spectroscopy (EELS) 39

3.3.6. Thermogravimetric Analysis (TGA) 40

3.3.7. Brunauer-Emmett-Teller (BET) measurement 40

3.4. Electrochemical Techniques 41

3.4.1. Galvanostatic Discharge/Charge 41

3.4.2. Cyclic Voltammetry (CV) 42

3.4.3. Slow Anodic Sweep Voltammetry (SASV) 43

3.4.4. Electrochemical Cycling..... 43

3.4.5. Electrochemical Potential Impedance Spectroscopy (EPIS) 43

3.4.6. Rotating Disk and Ring-Disk Electrode Voltammetry (RDE and RRDE)..... 44

3.4.7. Ring Electrode Collection Efficiency Determination..... 46

3.4.8. Hg/HgO Reference Electrode Calibration 47

3.4.9. Hydrogen Peroxide Electrochemical Reduction Reaction (HPRR) 48

CHAPTER 4. INVISTIGATION OF THE ELECTROCATALYTIC ACTIVITY OF A-SITE DOPED NICKELATES IN Li-O_2 BATTERY 49

4.1. Summary 49

4.2. Introduction 49

4.3. Experimental 51

4.3.1. Catalysts Synthesis 51

4.3.2. Cathode Preparation 52

4.3.3. Battery Assembly 52

4.3.4. Characterization..... 53

4.3.5. Electrochemical Testing 53

4.4. Results and Discussion..... 54

4.4.1. Catalyst Synthesis..... 54

4.4.2. Electrochemical Characterization..... 56

4.5. Conclusions 62

CHAPTER 5. NANOSTRUCTURED La_2NiO_4 AS EFFICIENT AND STABLE CATHODE ELECTROCATALYST FOR Li-O_2 BATTERY 63

5.1. Summary 63

5.2. Introduction 63

5.3. Experimental Details 64

5.3.1. Catalyst Synthesis 64

5.3.2. Cathode Fabrication 65

5.3.3. Battery Assembly 66

5.3.4. Characterization 66

5.3.5. Electrochemical Testing 67

5.4. Results and Discussions 68

5.4.1. Controlling the Catalyst Morphology 68

5.4.2. Galvanostatic Discharge-Charge 71

5.4.3. Impact of LNO on Li_2O_2 Formation 74

5.4.4. Impact of LNO Nanorods on the Oxygen Evolution Kinetics 75

5.4.5. Electrochemical Cycling 77

5.5. Conclusions 79

CHAPTER 6. TUNING THE ACTIVITY OF NANOSTRUCTURED, NON-PRECIOUS METAL OXIDES FOR LOW TEMPERATURE ELECTROCHEMICAL OXYGEN REDUCTION 80

6.1. Summary 80

6.2. Introduction 80
6.3. Experimental Details 83
6.3.1. Catalyst Synthesis 83
6.3.2. Thin-Film Preparation 83
6.3.3. Electrochemical Measurements 84
6.3.4. Characterization 86
6.4. Results and Discussion 86
6.4.1. Catalyst Synthesis 86
6.4.2. Electrochemical Performance 88
6.4.3. Electrocatalytic Activity of Inherent Metal Oxides (NiO, MnO and Mn_2O_3) 91
6.4.4. ORR Kinetic Model 93
6.4.5. Hydrogen Peroxide Reduction Reaction 97
6.4.6. Electrochemical Cycling Stability Tests 99
6.5. Conclusions 100
CHAPTER 7. GENERAL CONCLUSIONS AND FUTURE WORK 102
7.1. Summary 102
7.2. General Conclusions 102
7.3. Future Work Directions 104
APPENDIX STANDARD ELECTRODE POTENTIALS 106
REFERENCES 107

ABSTRACT 129

AUTOBIOGRAPHICAL STATEMENT 132

LIST OF TABLES

Table 1.1 Theoretical voltages and energy densities of lithium oxide/peroxide formation 9

Table 2.1 Thermodynamic electrode potentials of electrochemical O_2 reductions[22,23] 15

Table 3.1 Collection efficiency values at varying rotational speeds 47

LIST OF FIGURES

Figure 1.1 (a) The CO_2 levels during the last three glacial cycles, as reconstructed from ice cores.[1,3] (b) The change in global surface temperature relative to 1951-1980 average temperatures.[2] 2

Figure 1.2 The pie chart represents the U.S. annual energy consumption by sector, while the bar chart represents the energy source of the transportation sector. The total U.S. average annual energy consumption is about 98 quadrillion Btu.[5] 3

Figure 1.3 (a) Specific energies and energy densities of rechargeable battery systems and internal combustion engines. The highest data points represent the theoretical value of active materials based strictly on thermodynamics, while the lowest data points represent the current practical value of the battery.[9] (b) The theoretical and practical specific energies (Wh/kg) for various types of rechargeable batteries compared to gasoline.[4] 7

Figure 1.4 Schematic representation of the four different architectures of Li-air battery based on the electrolyte type employed.[4] 10

Figure 2.1 The polarization curves for two pairs of the key energy-related electrochemical reactions and their overall reaction equations. Red and blue curves refer to the hydrogen-involving and oxygen-involving reactions, respectively. The lines are not drawn to scale.[21] 15

Figure 2.2 (a) and (b), Proposed reactions for the shuttling process at the end of charge. For EC in the electrolyte, the solvated O^{2-} reacts with it, forming an intermediate radical A, the radical then diffuses to the anode and acquires electrons to become A^{2-}, which diffuses back and imparts the electron; the A/A^{2-} redox cycle thus provides the shunting current through the liquid electrolyte. (c) Cycling performance of charge/discharge capacity and Coulombic efficiency against Li metal anode under 120 A kg^{-1}.[128] 19

Figure 2.3 (a) Illustration of the unit cell of the perovskite structure.[157] (b) Experimental voltage at 25μA cmox-2 as function of estimated e_g occupancy of the $LaBO_3$ series and other relevant perovskites.[17] 25

Figure 2.4 Stoichiometric crystal structure of A_2BO_4-type oxides, where A is lanthanum (green atoms) and B is nickel (gray atoms).[193] 26

Figure 3.1 Schematic illustration of the synthesis of La_2NiO_4 nanorods..... 29

Figure 3.2 Schematic of the battery design and the contents of the button cell..... 31

Figure 3.3 Catalyst/carbon thin-film deposited on glassy carbon disk electrode. 32

Figure 3.4 Rotating ring-disk electrochemical cell design 33

Figure 3.5 Schematic representation of the process that occurs in an X-ray diffraction experiment. 35

Figure 3.6 Schematic representation of the process that occurs in the energy dispersive x-ray spectroscopy experiment..... 36

Figure 3.7 Schematic representation of the process that occurs in XPS experiment..... 37

Figure 3.8 Four consecutive discharge/charge cycles of non-aqueous Li-O_2 cell with Ketjen black carbon cathode with 1M $LiPF_6$ dissolved in carbonated based electrolyte, using 100 mA/g_{carbon} current density. 42

Figure 3.9 Illustration of the oxygen reduction reaction occurring during RRDE experiment ... 45

Figure 3.10 Chronoamperometry experiment of Pt-ring and glassy carbon disk electrodes in 0.1 M KCl electrolyte containing 4 mmole of $K_3\{Fe(CN)_6\}$. The ring and disk electrodes were held at a constant potential of 1.5 V and 0.1 V, respectively..... 47

Figure 3.11 (a) OCV plot of H_2-saturated 0.1 M KOH, (b) cyclic voltammogram of H_2-saturated 0.1 M KOH electrolyte using Pt-gauze as both working and reference electrode and Hg/HgO as counter electrode..... 48

Figure 4.1 X-ray diffraction patterns of the synthesized lanthanide nickelate catalysts and their respective standard JCPDS data..... 55

Figure 4.2 SEM images of the synthesized Ln_2NiO_4 oxides: a) La_2NiO_4, b) $LaPrNiO_4$, c) Pr2NiO4, d) $PrNdNiO_4$ and e) Nd_2NiO_4 56

Figure 4.3 Discharge–charge profiles of Li–O_2 batteries composed of carbon-only and 40% electrocatalysts (LNO, LPNO, PNO, PNNO and PNO) supported on carbon cathodes 57

Figure 4.4 (a) CV anodic scans of carbon and Ln_2NiO_4/carbon cathodes using 0.1 mVs^{-1} scan rate. (b) The corresponding peak potentials of the anodic scan as a function of the oxide composition. The dashed line represents the theoretical potential for OER (Li_2O_2 decomposition)..... 58

Figure 4.5 (a) CV anodic scans of carbon and Ln_2NiO_4/carbon cathodes using 0.1 mVs^{-1} scan rate. (b) The corresponding peak potentials of the anodic scan as a function of the oxide composition. The dashed line represents the theoretical potential for OER (Li_2O_2 decomposition)..... 59

Figure 4.6 (a) X-ray diffraction patterns of the synthesized $Ca_{0.25}La_{1.75}NiO_4$, $Sr_{0.25}La_{1.75}NiO_4$ and $Ba_{0.25}La_{1.75}NiO_4$. SEM images of the synthesized (b) $Ca_{0.25}La_{1.75}NiO_4$, (c) $Sr_{0.25}La_{1.75}NiO_4$ and (d) $Ba_{0.25}La_{1.75}NiO_4$..... 60

Figure 4.7 Full discharge/charge performance using 40% catalyst loading on Ketjen Black carbon cathodes with a carbon loading on each cathode of 0.985 mg_{carbon}/cathode. The constant

current density used was 50 mA/g_{carbon} with discharge and charge cutoff voltages of 2 and 4.5 volts, respectively. (b) X-ray diffraction patterns after full charge/discharge studies of the cathodes containing $Ca_{0.25}La_{1.75}NiO_4$, $Sr_{0.25}La_{1.75}NiO_4$ and $Ba_{0.25}La_{1.75}NiO_4$ 61

Figure 5.1 (a) Crystal structure of stoichiometric A_2BO_4 showing the perovskite-like and rocksalt-like layers. (b) Schematic illustration of the synthesis of LNO nanorods and nanospheres..... 69

Figure 5.2 (a) XRD patterns of (i) LNO nanorods, (ii) LNO nanospheres and (iii) the standard data for $La_2NiO_{4+\delta}$ (JCPDS No. 34-0314). SEM images of (b) LNO nanorods and (c) LNO nanospheres..... 70

Figure 5.3 (a) Bright-field (BF) TEM image of an individual LNO nanorod. (b) High-resolution (HR) TEM image of the edge of an individual LNO nanorod. The inset in image (b) shows the corresponding fast Fourier transform (FFT) pattern of the image..... 70

Figure 5.4 TGA curves of impregnated LNO nanorods and nanospheres on Ketjen Black carbon powder..... 71

Figure 5.5 Discharge–charge profiles of Li–O_2 batteries composed of 40% LNO-nr (red) and 40% LNO-ns (blue)..... 72

Figure 5.6 (a) Discharge–charge profiles of Li–O_2 batteries composed of carbon-only cathodes (black line), and carbon cathodes with 20 wt% (red line), 40 wt% (blue line) and 60 wt% (green line) nanorod LNO electrocatalyst. Error bars were generated for three replicas of each experiment. (b) Charging profiles (specific charge capacity vs. charging voltage) of the same battery cells..... 73

Figure 5.7 (a) XRD patterns of carbon-only cathodes (i) as-prepared, (ii) after first discharge, and (iii) after first charge. (b) XRD patterns of LNO-nr/carbon cathodes (i) as-prepared, (ii) after first discharge, and (iii) after first charge. The results for the LNO/carbon cathodes were similar for all the different LNO-nr loadings..... 74

Figure 5.8 (a) Darkfield TEM of the Li_2O_2 particles formed on carbon-only cathode after first discharge. The inset between image a and b shows the EELS spectra of Li k-edge of the particles on both cathodes. (b) Dark-field TEM of Li_2O_2 particles formed on LNO containing cathode after first discharge. Dashed circles are used for visual enhancement of the Li_2O_2 particles on the surface of LNO nanorods..... 75

Figure 5.9 SEM images of Li_2O_2 containing (a) carbon and (b) nr-LNO containing cathodes... 76

Figure 5.10 (a) Slow anodic sweep voltammograms (SASV) of carbon-only cathode with preloaded Li_2O_2 (black curve) and nr-LNO/carbon cathode with preloaded Li_2O_2 (red curve). The scan rate used in these experiments was 0.02 mV/s with a voltage window from OCV (~2.8 V) to 4.5 V. (b) XRD spectra of the carbon-only cathode (i) before and (ii) after the SASV experiment, and nr-LNO/carbon cathode (iii) before and (iv)

after the SASV experiment. The inset in figure (a) shows the loading verification of Li_2O_2 on nr-LNO/carbon cathode charged galvanostatically using 100 mA/g_{carbon} ... 77

Figure 5.11 Charge/discharge cycling performance of battery cells containing (i) carbon-only cathode, and (ii) nr-LNO/carbon cathode. A limiting specific capacity of 500 mAh/g_{carbon} and a current density of 100 mA/g_{carbon} were used in these experiments 78

Figure 5.12 XRD spectra of (i) the carbon-only cathode, and (ii) nr-LNO/carbon cathode after 20 charge/discharge cycles 78

Figure 6.1 (a) XRD spectra, (b) FE-SEM images and (c) ICP analysis of the synthesized R-P oxides. The M in Ni/M ratio represents the dopant amount (Cr, Mn, Co and Cu) (d) Atomic resolution HAADF image of a Co-LNO sample 87

Figure 6.2 Cyclic Voltammograms (CVs) of $La_2Ni_{0.875}M_{0.125}O_4$ (M is specified in the figure), bare XC-72 carbon, & Pt/C deposited on glassy carbon electrode (5 mm diameter) in O_2-saturated (solid lines) and Ar-saturated (dash lines) 0.1 M KOH electrolyte using 50 mV s^{-1} scan rate..... 88

Figure 6.3 Rotating Ring-Disk Voltammograms of $La_2Ni_{0.875}M_{0.125}O_4$ (M is specified in the figure) and Pt/C electrocatalysts deposited on glassy carbon electrode (5 mm diameter) in O_2 saturated 0.1 M KOH electrolyte at various rotating speeds (9 perfect squares between 100 and 2500 rpm) using 10 mVs^{-1} scan rate. The catalyst loading in these experiments was fixed at 250 $\mu g/cm^2$ for the oxides and 65 $\mu g/cm^2$ for commercial Pt/C. The negative current value is related to the disk activity while the positive current values represent the ring electrode activity (held at 1.2 V constant potential throughout the measurement). The Pt/C voltammetry scans show that the diffusion limited current density is about -5.6 mA/cm^2 at 1600 rpm, which agrees with the reported value for $4e^-$ ORR on single and poly-crystalline Pt electrodes. The onset potential for the control experiment with Pt/C also is consistent with literature at 0.91 V. 89

Figure 6.4 (a) Rotating ring-disk voltammograms of $La_2Ni_{0.875}M_{0.125}O_4$ thin-films in O_2-saturated 0.1 M KOH at 10 mV/s scan rate and 1600 rpm rotation speed. (b) Zoomed-in view of the boxed region shown in (a). Inset in (b) shows the plotted onset potentials of the oxides as a function of composition..... 90

Figure 6.5 (a) Koutecky–Levich plots of $La_2Ni_{0.875}M_{0.125}O_4$ calculated at 0.4 V vs RHE (b) number of electrons transferred and hydrogen peroxide formation during ORR calculated at 0.4 V for all oxides..... 91

Figure 6.6 Rotating ring-disk voltammograms of NiO, MnO, Mn_2O_4 and Mn-LNO thin-films in O_2-saturated 0.1 M KOH at 10 mVs^{-1} scan rate and 1600 rpm rotation speed..... 92

Figure 6.7 Cyclic Voltammograms (CVs) (a) NiO (b) MnO and (c) Mn_2O_3 deposited on glassy carbon electrode (5 mm diameter) in O_2-saturated (solid lines) and Ar-saturated (dash lines) 0.1 M KOH electrolyte using 50 mV s^{-1} scan rate. 92

Figure 6.8 High-resolution XPS scan of Ni 3p region (Envelope: orange curve, Raw data: black squares, 3p $^{3}/_{2}$ fit: green curve and 3p ½ fit: red curve) in (a) Cr-LNO, (c) Mn-LNO, (e) Co-LNO, (g) Cu-LNO and (i) LNO. High resolution XPS scan of M-site 2p region (Envelope: blue curve, Raw data: black squares, 2p $^{3}/_{2}$ fit: green curve and 2p ½ fit: red curve) of: Cr-site in (b) Cr-LNO, Mn-site in (d) Mn-LNO, Co-site in (f) Co-LNO, Cu-site in (h) Cu-LNO. 97

Figure 6.9 (a) HPRR voltammograms of R-P oxides (b) HPRR voltammogram of CoLNO at different speeds at 1600 rpm using 10 mV s^{-1} scan. 98

Figure 6.10 k_1/k_2 ratios of R-P oxides as a function of potential. 99

Figure 6.11 (a) Cycling stability test of XC-72 carbon thin films with (light blue curves) and without Mn-LNO (black curves): LSVs before and after 10,000 cycles. High-resolution XPS scan of Ni 3p region before (b) and after (d) 10,000 CV scans with orange curve as the envelope, scatter points are the raw data, and green and red curves for Ni 3p $^{3}/_{2}$ and 3p $^{1}/_{2}$ fit respectively. High-resolution XPS scan of Mn 2p region before (c) and after (e) 10,000 CV scans with orange curve as the envelope, scatter points are the raw data, and green and red curves for Mn 2p $^{3}/_{2}$ and 2p $^{1}/_{2}$ fit respectively. 100

CHAPTER 1. INTRODUCTION

1.1. Summary

This chapter gives a brief introduction to the current worldwide energy challenges associated with the increase in energy demands. The escalating concerns regarding global warming and the urgent need for more reliable energy storage and conversion devices will also be discussed. This chapter also briefs on the current energy storage devices available commercially and potential technologies that are being investigated as alternatives. We discuss the theoretical limitations and practical challenges of these technologies and the role of oxygen electrocatalysis in addressing these challenges. We concisely summarize the extent of this research topic, describe the research scope and briefly introduce the succeeding chapters.

1.2. Global Warming and Energy Utilization

Currently, the evidence of global warming and climate change has surpassed the questioning stage. The high concentrations of greenhouse gases (mainly consisting of CO_2 and CH_4) generated from industrial energy conversion technologies have led to rise in the global surface temperatures. CO_2 levels in the atmosphere have been on the rise since the beginning of the industrial revolution due to human activities, such as mining and combustion of fossil fuels (such as petroleum, coal and natural gas). Figure 1.1 (a) shows the atmospheric carbon dioxide concentration in parts per million for the last half million years. The data presented in this figure come from a variety of historical ice core studies and recent air monitoring. It is very clear from the graph that the concentration of CO_2 has currently spiked to almost double the historical variation values. The current reading of CO_2 is about 405 ppm (parts per million), which is 100 ppm more than the highest ever detected value over the last million years.[1] Figure 1.2 (b) shows the annual mean global surface temperature change relative to 1951-1980 average temperatures,

which indicates that the effect of global warming on climate is occurring at an escalating rate.[2] Another negative effect of CO_2 is the fact that the oceans absorb CO_2 from the atmosphere leading to its reaction with seawater to form carbonic acid. This process increases the acidity of the oceans disturbing the balance of minerals in the water, which makes it difficult for certain marine animals to build their protective skeletons or shells.

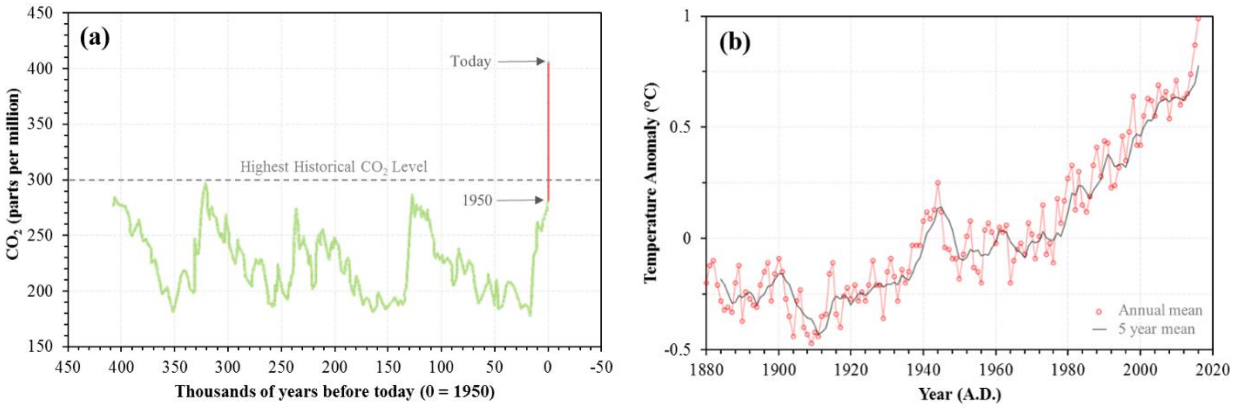

Figure 1.1 (a) The CO_2 levels during the last three glacial cycles, as reconstructed from ice cores.[1,3] (b) The change in global surface temperature relative to 1951-1980 average temperatures.[2]

Utilization of fossil fuels as energy sources is the largest contributor to CO_2 emissions. Oil represents 34% of the world's total primary energy source and it accounts for 40% of the total CO_2 emission into the atmosphere.[4] In 2015, petroleum products provided about 92% of the total energy used from the U.S. transportation sector (Figure 1.2.), with only 1% coming from other sources such as energy storage and conversion devices.[5]

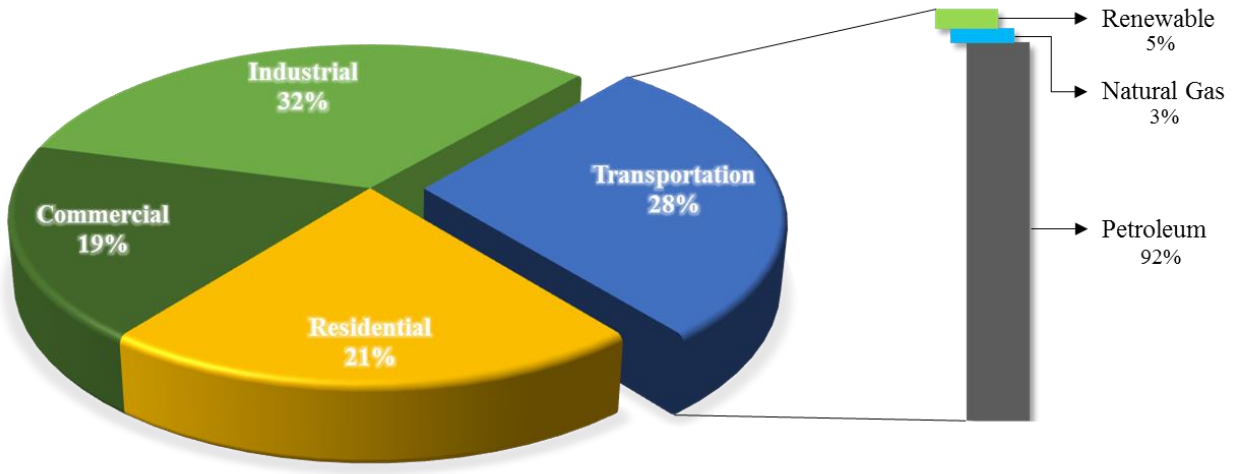

Figure 1.2 The pie chart represents the U.S. annual energy consumption by sector, while the bar chart represents the energy source of the transportation sector. The total U.S. average annual energy consumption is about 98 quadrillion Btu.[5]

In addition to the impact on climate, petroleum resources are also becoming scarce over the years. Based on a 2016 annual statistical review of the world energy report published by British Petroleum,[6] the total approved oil reserves would last for another 51 years if the reserve per production ratio remains the same. Therefore, there is an immediate need to shift our dependence from fossil fuels.[7]

Recently, renewable energy sources (such as wind and solar) have undergone significant technological developments, as well as reduction in cost per power unit generation. One main issue associated with renewable energy supplies is that their power generation is intermittent. For instance, solar power generation plants are dependent on the time of the day, year and weather, and can't provide electricity on demand at any time. The same follows for other sources like wind and tidal waves. Therefore, development of technologies capable of storing or converting the energy generated from these sources is necessary.[8]

Energy can be stored in many forms: mechanical (pumped-storage, compressed air and flywheel), thermal (latent heat storage), electrical (capacitors), chemical (hydrogen and methane)

and electrochemical (rechargeable batteries and supercapacitors). All of which have different energy storage capabilities, power release potentials and storage durability.

1.3. Energy Storage: Batteries

Batteries are energy storage electrochemical systems that convert stored chemical energy to electrical energy through reduction-oxidation (redox) reactions. A battery cell consists of two electrodes that are internally connected by an ionic conductive material, known as the electrolyte, and externally connected to an electrical consumption device known as a load. Batteries fall into two main categories based on the electrochemical reactions that govern their performance: primary batteries and secondary batteries. Primary batteries are capable of generating energy through the decomposition of the positive electrode (anode) by electrochemical oxidation reaction and the negative electrode (cathode) by electrochemical reduction reaction to form new chemical species that are irreversible (unfavorable to decompose back electrochemically to their original state), resulting in non-reversibility of these systems. These types of batteries are more suitable for applications that require low energy over a long period of time or in cases where the charging process is not an option (e.g. watches and implantable power devices). On the other hand, secondary batteries have the ability to recharge by the aid of an opposite external current that drives the reaction in reverse.[9] Several rechargeable battery systems have been developed and commercialized over the past few decades, but none of these systems provide a specific energy (mileage range in electric vehicle application) and/or specific power (acceleration) that is close to what gasoline can offer.[10]

The oldest type of rechargeable battery is the lead-acid battery (PbA). It was invented in 1859 by French physicist Gaston Planté. This battery is regarded to be the technology that set the birth of electric vehicles during the late 19th century. The lead-acid battery uses lead dioxide as the

positive electrode (cathode) and metallic lead as the negative (anode) active material. Both electrods are submerged in sulfuric acid electrolyte solution. As the cell discharges, both electrodes are converted to lead sulfate. The process reverses on charge. Although, PbA batteries have high power output and are not expensive, they suffer from low specific energy (theoretical 252 Wh/kg and practical 40 Wh/kg) and cyclability.[9]

Another type of battery technology is the nickel-cadmium battery (NiCd) which offers good performance (specific power) and cyclability. It utilizes nickel (III) oxyhydroxide as the positive electrode and metallic cadmium as the negative electrode, both separated by an alkaline electrolyte (potassium hydroxide) soaked separator. NiCd battery has some major drawbacks related to the poor charge retention and environmental concerns with the use of cadmium.[9] The rechargeable nickel-metal hydride (NiMH) battery is a relatively new technology with characteristics similar to those of the nickel-cadmium battery. The principal difference is that the NiMH uses hydrogen, absorbed in a metal alloy, for the active negative material in place of the cadmium used in the NiCd. Over the 1990's, the specific energy and energy density of NiMH batteries have been increased by over 35% as a result of improvements in both the positive and negative electrodes. This battery has a key disadvantage posed by its high self-discharge rate and shelf-life time.[9]

Lithium ion battery (LIB) present the youngest (commercialized 1991) and yet fastest growing type of battery. LIBs comprise cells that employ lithium intercalation compounds as the positive and negative electrodes. As the battery is cycled, lithium ions (Li^+) exchange between the cathode and anode electrodes. The positive electrode material is typically a metal oxide with a layered structure, such as lithium cobalt oxide ($LiCoO_2$), or a material with a tunneled structure, such as lithium manganese oxide ($LiMn_2O_4$) supported on a current collector aluminum foil. The

negative electrode material is typically graphitic carbon - also a layered material supported on copper current collector. The LIB market has grown in a decade from an R&D interest to sales of over 400 million units in 1999. Currently, this battery technology is showing the utmost potential with the Tesla Roadster exhibiting more than 200 miles range per charge. A major disadvantage related to this battery technology is that there is very limited room for improvement given that the current specific energy has almost reached the ceiling performance. Also, there are major safety concerns with this technology, specifically, self-combustion due to heat, short-circuit and/or overcharge.[9]

The concept of the lithium air battery (Li-air, also called Li-O_2) was first introduced in 1976 by Littauer *et. al.*,[11] but it was not realized practically due to the rapid reaction of lithium with water in aqueous electrolyte media that hindered the efficient formation of lithium oxide/peroxide – the discharge product that stores the electrical energy. In 1996, Abraham and Jiang showed that a Li-air battery can be synthesized by using a non-aqueous electrolyte.[12] Based on the theoretical specific capacity of lithium, 3.862 mAh/kg, one can calculate the theoretical energy density generated per kg of lithium to be 11,140 Wh/kg, almost 10 times that of the state-of-the art LIBs. This high specific energy (illustrated in Figure 1.3) has led to strong interest in developing Li-air batteries for powering EVs, enabling driving ranges comparable to gasoline powered automobiles. Due to the instability induced by the complex chemistry associated with the charge/discharge processes, this battery is still under experimental investigation. Over the last decade, the scientific community has pinpointed a lot of challenges posed by the poor cyclability, operating rate, stability and overpotential losses. In order to properly discuss the challenges associated with these systems, an introduction to the electrochemistry of these systems is provided below.

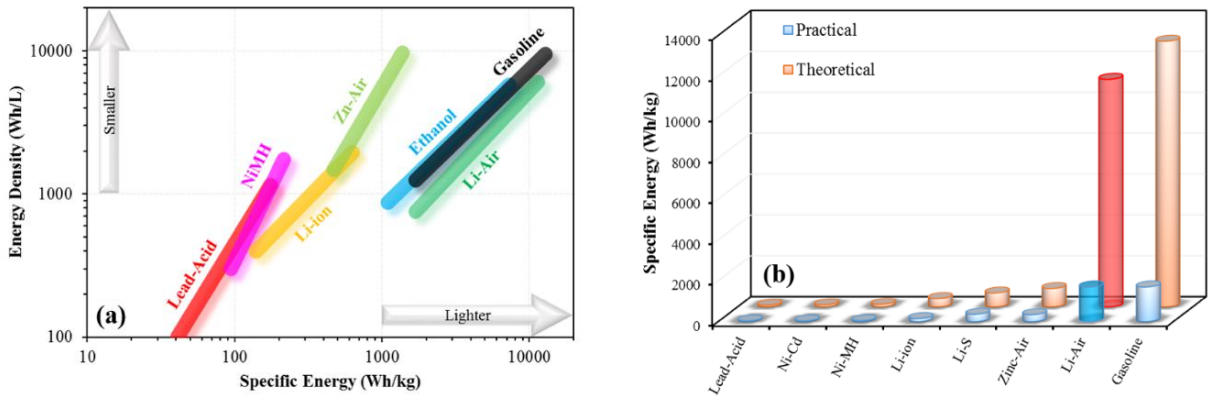

Figure 1.3 (a) Specific energies and energy densities of rechargeable battery systems and internal combustion engines. The highest data points represent the theoretical value of active materials based strictly on thermodynamics, while the lowest data points represent the current practical value of the battery.[9] (b) The theoretical and practical specific energies (Wh/kg) for various types of rechargeable batteries compared to gasoline.[4]

1.4. Electrochemistry of Li-air Batteries

The overall reaction of any electrochemical cell is determined by the combination of both half-cell reactions that occur on each electrode. The theoretical or standard potential (voltage) of the cell is equal to the difference between the electrochemical potential of the reduced species (cathode materials, $E^0_{Cathode}$) and the oxidized species (anode materials, E^0_{Anode}). The following equation shows how the standard potential can be calculated:

$$E^0_{Cell} = E^0_{Cathode} - E^0_{Anode} \qquad \text{(eqn 1)}$$

The unit associated with equation 1 is Volts (V). Each element and molecule that can reduce or oxidize electrochemically to a lower or higher oxidation state(s) has a standard potential (reduction or oxidation) value. This value is equal to the potential difference between the desired element or molecule and the hydrogen potential, in which the hydrogen potential is considered to be 0 Volts. Table A1 (see appendix) shows the reduction potential for some of the elements in aqueous solution at room temperature. Some molecules do not have a standard redox potential, because they vary based on the electrolyte media being used. For instance, the oxygen molecule

has a standard reduction potential of 1.229 V (vs. RHS) in aqueous media, 1.21 V (vs. $Fc^{+/0}$) in acetonitrile and 0.60 V (vs. $Fc^{+/0}$) in dimethylformamide.[13]

The overall electrochemical reaction will have a specific number of electrons transferred during the reaction, which is determined by the half-cell reactions. The number of electrons transferred (n) and the standard potential (E^0_{Cell}) can be used to determine the standard Gibbs free energy (ΔG^0_{Cell}) of the reaction using the following equation:

$$\Delta G^0_{Cell} = -nFE^0_{Cell} \quad \text{(eqn 2)}$$

where n is the number of electrons (mole of e^-) and F is Faraday's constant that represent a fixed electric charge per mole of electron and it is equivalent to 96485.34 C/mol e^-. This value is calculated by multiplying the electric charge of one electron ($1.6021766 \times 10^{-19}$ C) by Avogadro's number (6.022×10^{23} mol^{-1}). ΔG^0_{Cell} is expressed in kJ/mol where $1\ kJ = 0.278\ Wh$ and $1\ Ah = 3600\ C$.

The amount of electrical charge available in any material that can be reduced electrochemically is usually normalized by the weight of that material and known as the theoretical specific capacity (commonly expressed in $Ah/kg_{active\ material}$). Knowing the molecular weight ($M.wt$) of the material, one can calculate the theoretical specific capacity by using the equation below:

$$\text{Theoretical Specific Capacity} = \frac{nF}{M.wt} \quad \text{(eqn 3)}$$

The electrochemical reactions that govern the chemistry in Li-air batteries are shown in Table 1.1. Based on the theoretical specific capacity of lithium, 3.862 mAh/kg, one can calculate the theoretical energy density generated per kg of Li as shown below. This theoretical specific capacity is comparable to that of gasoline that is used in thermochemical processes. Figure 1.3

clearly shows that Li-air batteries have the highest potential among all the currently explored energy storage systems exhibiting the highest theoretical energy density.[4]

Table 1.1 Theoretical voltages and energy densities of lithium oxide/peroxide formation

Electrochemical reaction	Gibbs free energy of formation	Voltage potential	Energy density (excluding the product weight)	Energy density (including the product weight)
$2Li + O_2 \xleftrightarrow{2e^-} Li_2O_2$	-571.2 kJ/mol	2.96 V	11,426 Wh/kg	3,457 Wh/kg
$2Li + \frac{1}{2}O_2 \xleftrightarrow{2e^-} Li_2O$	-562.1 kJ/mol	2.91 V	11,248 Wh/kg	5,226 Wh/kg

There are four different configurations of Li-air batteries (see Figure 1.4), depending on their electrolyte medium (aqueous, non-aqueous, mixed and solid). For the aqueous and mixed aqueous/aprotic electrolyte configurations, the cathode chemistry is similar (reaction product is $LiOH \cdot H_2O$), and there is currently no evidence that the electrochemical reaction is reversible, except by mechanically removing the reaction products and replacing them with fresh reactants. In the case of solid state and aprotic (also known as non-aqueous) electrolyte configurations, it has been demonstrated that the reactions to form the storage product (Li_2O_2) are reversible, and the batteries are capable of undergoing multiple cycles.[4,12]

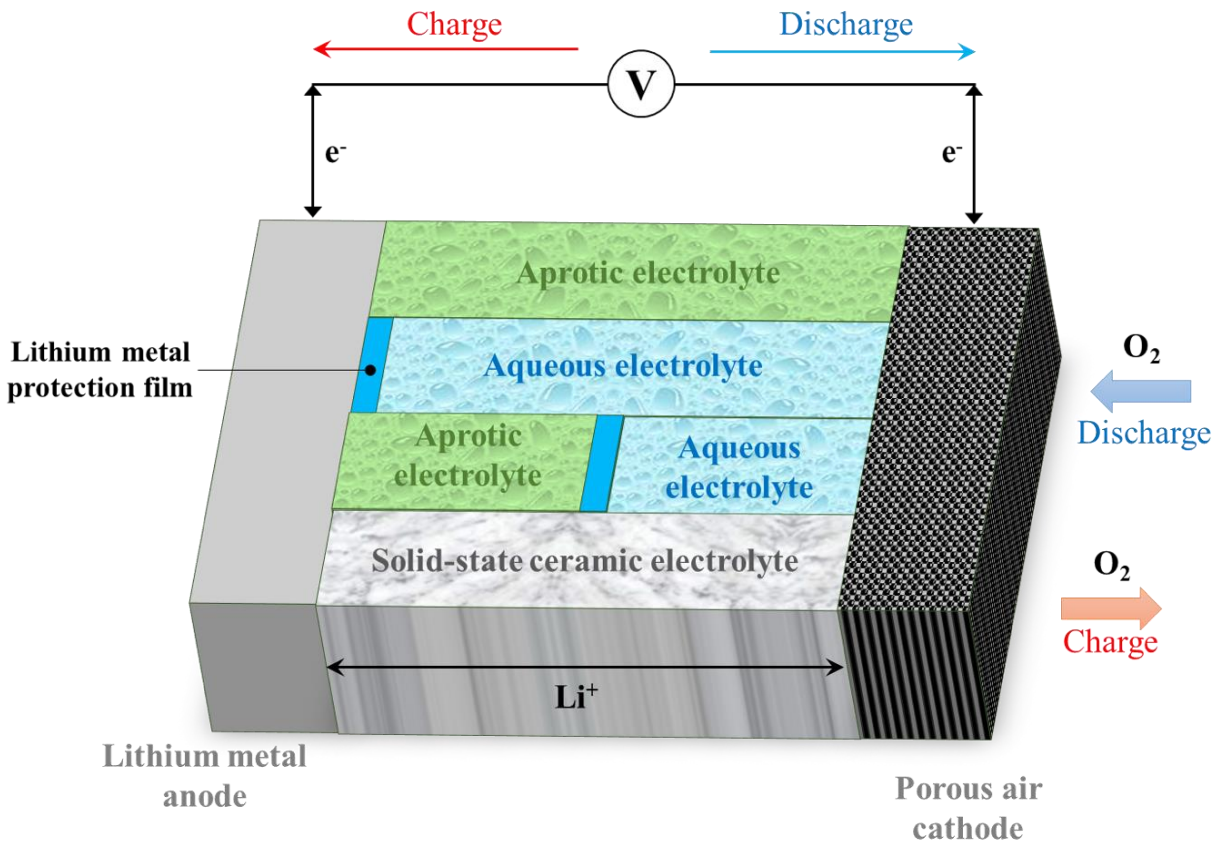

Figure 1.4 Schematic representation of the four different architectures of Li-air battery based on the electrolyte type employed.[4]

1.5. Scope of the Thesis

Despite the apparent remarkable superiority of Li-air battery technology compared to other rechargeable batteries, there are some intrinsic limitations hindering their market penetration, including: high charge overpotentials (poor OER activity), which largely affect the energy efficiency and cycling performance. Incorporation of noble metal electrocatalysts in Li-air cathodes have been shown to lower the overpotentials caused by the sluggish oxygen evolution reaction during charge, but these catalysts are limited by their high cost. Alternatively, non-precious, mixed ionic-electronic conducting oxides have also shown promising ORR and OER activity, but are largely limited by the poor understanding of the factors that governs their activity for proper optimization of their catalytic performance. In this thesis, the overall objective is to

determine the potential of non-precious metal based A_2BO_4 layered metal oxide structures (A = rare-earth metal and/or alkali-earth metal and B = transition metal) as efficient oxygen reduction/evolution electrocatalysts for use in low-temperature electrochemical systems, such as Li-O_2 batteries. The *overall hypothesis* is that tuning the A- and B-site composition of these oxides will lead to changes in the crystal and surface structure of these materials that consequently will affect their performance. The overall approach involves combining well-controlled synthesis techniques along with detailed characterization and electrochemical studies to develop structure-function relationships that can test the overall hypothesis and guide the optimization of these non-precious metal oxides for low-temperature oxygen electrocatalysis.

In Chapter 2, a rationale for the proposed work is provided through a comprehensive literature review of the state of oxygen electrocatalysis at low temperatures. We discuss the role of different electrocatalysts and proposed mechanisms for oxygen reduction (ORR) and evolution (OER). Fundamental studies using half-cell electrochemical rotating disc experiments on various electrocatalysts for ORR and OER are reviewed. We highlight the advantages and the disadvantages with the current state-of-the-art in oxygen electrocatalysis and set the stage for the study in this thesis.

In Chapter 3, a detailed description of the experimental methods and techniques employed in this thesis is presented. We also provide essential background regarding the theories and principles that govern the utilization of these techniques. Moreover, we report on the details of electrocatalysts synthesis, cathode fabrication, Li-O_2 battery design and assembly and thin-film deposition for rotating ring-disk electrode studies of the oxygen reduction reaction (ORR).

In Chapter 4, the specific objective is to study the effect of the nature of the A-site of first series R-P oxides (Ln_2NiO_4 (Ln = La, Pr, Nd and their combinations)) on electrochemical activity

for OER and ORR in Li-O_2 batteries. We hypothesize that varying the A-site of first series R-P oxides (Lanthanum, praseodymium and Neodymium), as well as doping it with various alkaline cations (Calcium, Barium, and Strontium) affects the catalyst structure due to inducing changes in the ionic radius of the A-site atoms, consequently affecting the activity. We discuss the structure-activity trend for these oxides for ORR and OER. We show that La_2NiO_4 exhibits the best performance among the investigated family of layered lanthanide oxides. An increase in the electrocatalytic activity of La_2NiO_4 is observed when the A-site is doped with alkaline metal, such as barium.

In Chapter 5, the specific aim is to determine the effect of surface structure of La_2NiO_4 (LNO) toward ORR and OER activity in Li-O_2 batteries. We hypothesize that the composition of the surface structure plays a critical role on the nature of the active sites and thus the catalytic activity of these oxides. To test this hypothesis, we utilize a well-controlled microemulsion method to synthesize La_2NiO_4 (LNO) nanostructures with high surface area and controlled surface morphology. The presented electrochemical studies show that the incorporation of LNO nanorods highly terminated by (001) Ni oxide surface facets in Li-O_2 cathodes result in lowering of the charging potential, and enhancement of the reversible specific discharge/charge capacities as compared to carbon-only cathodes.

In Chapter 6, the specific objective is to investigate the effect of B-site composition on the ORR activity of first series R-P oxide in alkaline media. The hypothesis is that the nature of the B-site on the surface of these oxides significantly affects the energetics of ORR due to the difference in the nature of interactions of these atoms with the ORR intermediates, consequently affecting activity and selectivity. We have mainly focused on B-site terminated nanostructures of $La_2Ni_{0.875}B_{0.125}O_4$ (B = Cu, Co, Fe, Mn and Cr) for this study due to their stability. We show that

the ORR selectivity and activity of $La_2Ni_{0.875}Mn_{0.125}O_4$ is superior among the investigated catalyst series. Furthermore, we report on the long-term stability of Mn-doped LNO under ORR conditions in alkaline media.

The major conclusions derived from the work presented in this thesis are summarized in Chapter 7. The impact of this work is discussed in context of the potential of non-precious metal layered A_2BO_4 oxides as electrocatalysts for oxygen electrocatalysis in energy conversion and storage systems. Future work directions in this area are also discussed.

CHAPTER 2. BACKGROUND AND LITERATURE REVIEW

2.1. Summary

In this chapter, a comprehensive literature review is presented on the state of oxygen electrocatalysis at low temperatures in alkaline media. We shed light on the role of electrocatalysts and proposed mechanisms for oxygen reduction and evolution reactions. We discuss fundamental studies using half-cell electrochemical rotating disk experiments on various electrocatalysts for ORR. We focus primarily on the role of the active transition metal sites, and the proposed activity descriptors developed to predict active electrocatalysts for these processes.

2.2. Introduction

Electrochemical oxygen reduction (ORR) and evolution (OER) reactions play an important role in many energy storage and conversion devices, such as fuel cells, water electrolyzers and metal-air batteries. As discussed in chapter 1, the need for sustainable energy sources is critical in dealing with the increasing energy demand and the carbon footprint in the atmosphere.[14]

ORR and OER suffer from high overpotential losses (high activation barriers) due to the complexity of the proton-coupled electron transfer.[15] The sluggish ORR kinetics (which occur on the cathode) in fuel cell applications contribute in large part to the overall efficiency drop.[16] This is demonstrated in Figure 2.1, which shows a crude depiction of the polarization curves of hydrogen and oxygen chemistries that typically occur in fuel-cell/electrolyzer reactions (both alkaline and acidic).[17] Thus, improving the oxygen electrocatalysis in these systems is of significant importance and largely investigated.

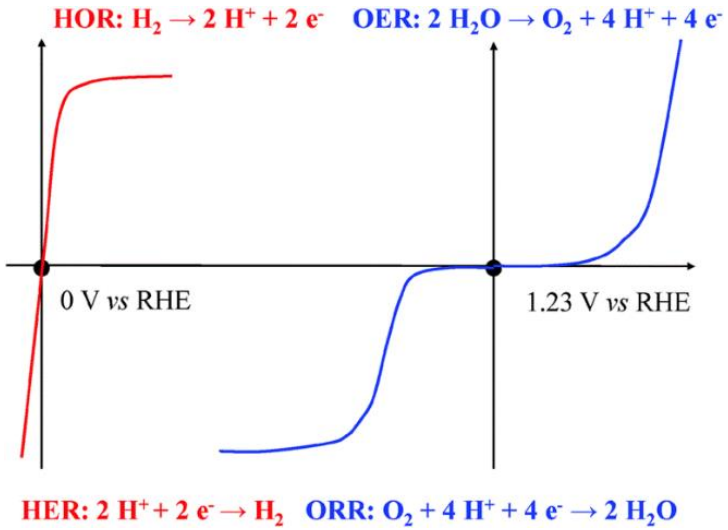

Figure 2.1 The polarization curves for two pairs of the key energy-related electrochemical reactions and their overall reaction equations. Red and blue curves refer to the hydrogen-involving and oxygen-involving reactions, respectively. The lines are not drawn to scale.[17]

2.3. Oxygen Electrocatalysis in Metal-Air Batteries

ORR in aqueous solution proceeds primarily via two reaction pathways: the direct 4-electron pathway to form H_2O, and the 2-electron pathway to form hydrogen peroxide (H_2O_2). In non-aqueous aprotic solvents and/or in alkaline solutions (metal-air batteries), the 1-electron reduction pathway from O_2 to superoxide (O_2^-) can also occur. Table 2.1 lists several typical ORR processes with their corresponding thermodynamic electrode potentials at standard conditions.[18]

Table 2.1 Thermodynamic electrode potentials of electrochemical O_2 reductions[18,19]

Electrolyte	ORR half-cell reactions	Thermodynamic electrode potential at standard conditions, V
Acidic aqueous solution	$O_2 + 4H^+ + 4e^- \rightarrow H_2O$	1.229
	$O_2 + 2H^+ + 2e^- \rightarrow H_2O_2$	0.70
	$H_2O_2 + 2H^+ + 2e^- \rightarrow 2H_2O$	1.76
Alkaline aqueous solution	$O_2 + 2H_2O + 4e^- \rightarrow 4OH^-$	0.401
	$O_2 + H_2O + 2e^- \rightarrow HO_2^- + 4OH^-$	-0.065
	$HO_2^- + H_2O + 2e^- \rightarrow 3OH^-$	0.867
Non-aqueous aprotic solvents	$O_2 + e^- \rightarrow O_2^-$	a
	$O_2^- + e^- \rightarrow O_2^{2-}$	b

a, b: The thermodynamic potentials for the 1-electron reduction reaction to form superoxide, and its further reduction to O_2^{2-}. Their values are strongly dependent on the solvent used.

Operation of ORR in alkaline media provides several advantages including the stability of the electrocatalysts and the electrochemical cell components. For example, aqueous metal-air batteries commonly use alkaline solutions as electrolyte because anodes and cathode electrocatalysts are relatively stable in basic media. On the other hand, acidic electrolytes present a challenge for practical applications because of the aggressive undesired reactivity with the anodes, leading to severe corrosion of the electrode.[20]

The oxygen electrochemistry on the cathode of non-aqueous Li-air batteries is quite complex, highly dependent on the nature of the electrode material, catalyst and electrolyte.[21,22] Using *in situ* surface-enhanced Raman spectroscopy (SERS), Peng *et. al*.[23] showed that ORR and OER on gold-based electrodes in Li-containing non-aqueous electrolyte follow the pathways shown below:

ORR:

$$O_2^- + Li^+ \rightarrow LiO_2 \qquad \text{(rxn 1)}$$

$$2\ LiO_2 \rightarrow Li_2O_2 + O_2 \qquad \text{(rxn 2)}$$

OER:

$$Li_2O_2 \rightarrow 2\ Li^+ + O_2 + e^- \qquad \text{(rxn 3)}$$

The electrochemical reduction of lithium superoxide to Li_2O_2 has also been reported. The overpotential losses associated with ORR and OER are vastly different due to the difference in the reaction pathways for these processes.

Recent studies have shown that lithium superoxide (LiO_2) can be stabilized on the catalyst surface as the main and only discharge product in Li-air batteries.[24,25-28] The authors used Ir supported on reduced graphene oxide (rGO) as the cathode electrocatalyst. The LiO_2 presence in the discharged cathodes was characterized using ex-situ Raman spectroscopy with a characteristic

Raman shift peak centered at 1123 cm^{-1}.[24] This was confirmed further using various chemical/electrochemical coupled spectroscopic techniques.[29] The benefit of stabilizing LiO_2 as the main discharge product comes from the lower overpotential losses during its dissociation as compared to Li_2O_2. Also, LiO_2 is found to be electronically conductive in nature at room temperature, based on ab-initio molecular dynamic simulations.[24]

Precious metals have been explored as potential cathode electrocatalysts for Li-air batteries (gold[23,30-33], palladium[30,34-38], platinum[30,34,39-43], silver[34,43-45], ruthenium[46-48], iridium[49] and noble metal alloys[50-59]). Recently, Lei *et. al.* [36,60] showed a very high ORR and OER activity for Pd nanoparticles synthesized by atomic layer deposition (ALD) (in conjunction with Al_2O_3 passivation) on carbon cathodes. Unfortunately, these cells exhibited low rechargeability.[61,62] Another study by Lu *et. al.*[34] using rotating disk electrode studies in Li containing electrolyte showed the following ORR activity trends for different metal electrocatalysts: Pd > Pt > Ru ≈ Au > GC (glassy carbon). In addition to metals, metal oxides have also been examined as cathode electrocatalysts in Li-air batteries, including manganese oxides with different phases,[63-68] structures[69-76] and metal decorations,[77-82] cobalt oxides (Co_3O_4),[83-95] CoO,[96] Fe_3O_4,[97] Fe_2O_3,[98] V_2O_5,[99,100] RuO_2,[91,101-103] CeO_2,[104] perovskites,[42,105-112] Co-Mn-O,[113] Co-Fe-O,[114] Ni-Co-O,[115-118] Ni-Fe-O,[119] Mn-Fe-O,[120] pyrochlore[121] and nickelates[122,123] supported on different carbon matrices (carbon black, carbon nanotubes, graphene, graphene nanosheets, carbon nanofibers, etc…). While some of these systems have shown promise, limited fundamental studies have hindered the optimization of their performance.

In a very recent publication, Zhu *et. al.*[124] demonstrated a new Li-O_2 battery concept. The authors were able to fabricate an air tight cell, containing a mixture of catalyst (nanoporous Co_3O_4)

and active material (Li_2O) as the cathode, in aprotic electrolyte cell configuration. The novelty of this study is that the oxygen from Li_2O is used to drive the electrochemical reactions below:

$$Li_2O_2 + 2Li^+ + 2e^- \leftrightarrow 2Li_2O \qquad (E^0 = 2.86\ V) \qquad \text{(rxn 4)}$$

$$LiO_2 + 3Li^+ + 3e^- \leftrightarrow 2Li_2O \qquad (E^0 = 2.88\ V) \qquad \text{(rxn 5)}$$

I*n situ* Raman spectroscopy of the electrochemical cell showed formation of both Li_2O_2 and LiO_2 upon charging. In addition, ^6Li nuclear magnetic resonance (NMR) of the discharged/charged cathodes showed consumption of Li_2O and formation of both Li_2O_2 and LiO_2 upon charging. All these techniques confirmed that the cell proceeded via the reactions shown above. This newly proposed Li-O_2 battery configuration has a theoretical capacity of 1340 Ah/kg, and was able to deliver about 50% of the theoretical capacity for over 130 cycles (90 days) (see Figure 2.2c). This represents a 2.6-fold increase in the capacity compared to the current state-of-the-art Li-ion battery, which has a practical capacity of about 230 Ah/kg. (see Figure 2.2). Figure 2.2 a and b, show the proposed reaction mechanism, which involves shuttling of electrons from the anode to the cathode through the electrolyte. Briefly, electrons from the anode complex with the ethylene carbonate (EC) molecule to form a superoxo-radical, which, in turn diffuses back to the cathode, providing the shunting current.

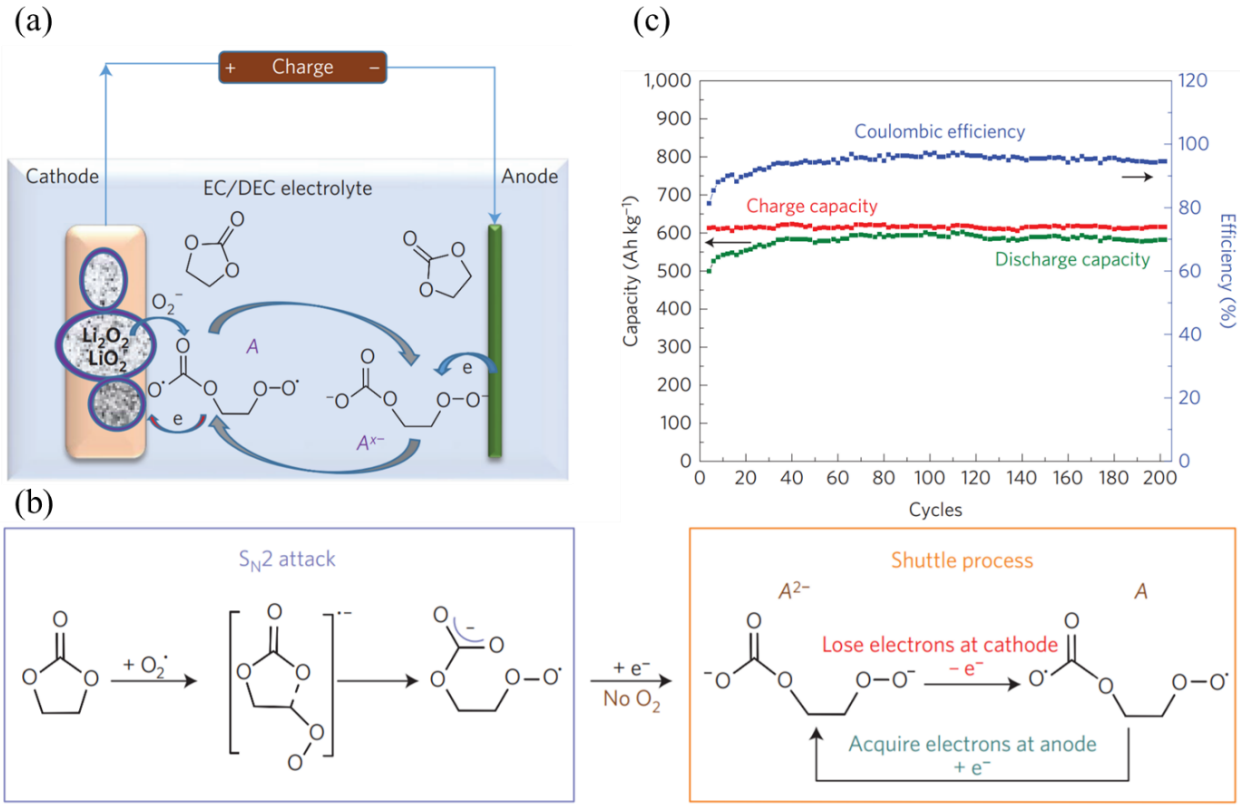

Figure 2.2 (a) and (b), Proposed reactions for the shuttling process at the end of charge. For EC in the electrolyte, the solvated O^{2-} reacts with it, forming an intermediate radical A, the radical then diffuses to the anode and acquires electrons to become A^{2-}, which diffuses back and imparts the electron; the A/A^{2-} redox cycle thus provides the shunting current through the liquid electrolyte. (c) Cycling performance of charge/discharge capacity and Coulombic efficiency against Li metal anode under 120 A kg^{-1}.[124]

2.4. ORR Electrocatalysis in alkaline media for Fuel Cells

2.4.1. Platinum and Platinum Alloy Catalysts

Platinum is the most studied ORR catalyst, and is considered to be the most active.[125] Pt is used to benchmark the ORR activity of other electrocatalysts with the aim of identifying materials that are less expensive but with similar performance to Pt. There are multiple factors that play major role in determining the activity of platinum nanoparticles, such as surface structure, particle size,[126] particle shape[127] and dispersion of the nanoparticles on carbon support.[128] It has been shown experimentally that the ORR activity of low index platinum surfaces follows the trend; {110} > {100} > {111}.[127] This activity trend is mainly attributed to the geometric effect of

different planes, as well as the adsorption of the electrolyte species. Theoretical calculations (density functional theory, DFT) predict a different activity trend than the one reported experimentally,[129] most likely due to the changes in the coverage of oxygen-containing species with the applied potential, as well as the effect of the free energy of reaction intermediates. High index planes (i.e. {221} and {331}) are expected to be much more active than Pt {111},[130] although their stability under cycling potential is a major concern. Pt nanoparticles within the range of 1 – 5 nm have been widely studied.[126,131,132] As particle size decreases, the distribution of Pt {111} and Pt {100} terrace sites decrease as well. 3 nm particles size show an optimum ORR behavior, while smaller sizes suffer from lower specific activity. This might be explained by the increase of low coordination sites (edges and kinks) on smaller particles, where oxygen binding energies are much stronger. Other researchers argue the effect of particle size within this range. Nesselberger *et. al.* found that minimum ORR specific activity change was observed with particle size variation (1 – 5 nm), while the activity increases linearly with increasing particle dispersion.[133]

Platinum alloys have attracted significant attention due to their superior ORR activity and durability in contrast to pure platinum metal. Alloying platinum with transition metals can induce many changes, such as alteration of the Pt-Pt bond distance, increase in surface roughness due to the dissolution of the transition metals, delay in surface oxide formation, variations in the d-band vacancy, etc. Stamenkovic *et. al.* reported the activity trend of sputtered polycrystalline Pt-alloy films to follow the order of Pt < Pt_3Ti < Pt_3V < Pt_3Ni < Pt_3Fe < Pt_3Co.[134] A slight change in this trend has also been reported for thermally treated Pt alloys, in which segregation of Pt atoms to the surface takes place resulting in a Pt-skin surface. Similar to pure Pt metal, the particle size, shape and dispersion of Pt-alloys as well as the degree of alloying have a direct impact on the ORR activity.

Alloying Pt with lanthanide metals has been shown to enhance the ORR activity by a factor of 5 over Pt. The lanthanide contraction can be used to control strain effects and tune the activity and stability of these materials. In the same study, the authors reported a volcano activity relationship in the order of Pt < Pt_5La < Pt_5Ce < Pt_5Tm < Pt_5Ca ≈ Pt_5Dy < Pt_5Sm < Pt_5Gd < Pt_5Tb.[135]

2.4.2. Carbon-Based Catalysts

In recent years, carbon-based catalysts have emerged as promising alternatives to the predominant noble and transition metal electrocatalysts for oxygen and hydrogen electro-chemistries in energy storage and conversion devices. Nitrogen-doped vertically aligned carbon nanotubes (VA-CNTs) were found to exhibit excellent activity towards ORR in alkaline media, were tolerant to CO-poisoning and minimized fuel crossover.[136] It was found that doping carbon with nitrogen induced charge redistribution and facilitated oxygen chemisorption and the electron transfer for ORR.[137,138] The same behavior was also reported for nitrogen-doped graphene electrocatalysts. Co-doped CNTs with various heteroatoms were found to further enhance the electrocatalytic activity for boron and nitrogen co-doped CNTs. DFT revealed that the enhancement in the activity of co-doped carbon materials was due to the ability to tune the energy bandgap and charge density.[139] Furthermore, sulfur and nitrogen co-doped CNTs have shown superior ORR activity in both acidic and alkaline media relative to single atom doped CNTs.[140] A nitrogen-doped graphene-CNT-carbon black composite with a well-defined porous structure was shown to have excellent long-term operational stability and high-power density in acidic polymer electrolyte membrane (PEM) fuel cells.[141] In general, such C–N bonds available in nitrogen-doped carbon materials are considerably polarized owing to the larger electronegativity of nitrogen than

carbon; this causes the carbon atoms adjacent to the nitrogen dopants to be positively charged and become the active sites for O_2 adsorption.[142]

2.4.3. Transition Metal Oxides

Recently, transition metal oxides have attracted significant attention as bifunctional electrocatalysts, recently. They are considered to be inexpensive compared to precious metals.[143] Controlling their particle size and shape is possible due to the wide range of synthesis methods and precursors that can be used. There are many types of transition metal oxides, such as single metals, mixed transition metals and mixed transition and non-transition metals. Furthermore, transition metal oxides can exist in mixed-valance states, creating oxygen defects in the structure. These defects have been shown to enhance the oxygen chemistry in these materials.[144] In the following sections we highlight literature reports on the most active oxides for oxygen electrocatalysis.

Cobalt-Based Oxides: Cobalt oxides have been shown to have excellent bifunctional activity towards ORR and OER when they are combined with carbon materials. Xiao *et. al.* investigated the electrocatalytic activity of spinel Co_3O_4 ($Co^{2+}Co_2^{3+}O_4$) anchored on graphene sheets.[145] The authors have demonstrated their ability to control the shape of the oxides. Furthermore, they were able to synthesize nanorods, nanocubes and nano-octahedrons with different exposed nanocrystalline surfaces {110}, {100} and {111}, respectively. The ORR catalytic trend followed {111} > {100} > {110}. They attributed the enhancement in oxygen reduction to the existence of Co^{2+} ions located on the tetrahedral sites, while Co^{3+} ions located on the octahedral sites were linked to OER activity. Liang *et. al.* also examined the synergetic potential of Co_3O_4 nanocrystals grown on mildly-reduced graphene oxide,[146] and found an unexpected enhanced bifunctional activity to both oxygen reactions.

Nickel-Based Oxides: Pure nickel oxides have been shown to have considerably good OER activity, although they suffer from poor ORR activity, rendering their use as bifunctional electrocatalysts.[143] On the other hand, nickel has certain properties that attract much interest in the electrocatalysis community. Nickel is electronically conductive, and its oxides are more resistant to corrosion in alkaline media than other transition metal oxides.[143]

Manganese-Based Oxides: Mn-oxides have been at the forefront of oxygen electrocatalysis among transition metal oxides. The factors that contribute to the wide spread investigation into the activity of these oxides, is their ability to exist in over 30 different crystal structures and a number of oxidation states.[143,147] Furthermore, Mn is the 12th most abundant element on earth.[148] Mn-containing oxides have shown superior activity that is comparable to platinum.[149,150] Stoerzinger *et. al.* has surveyed the literature reported activity of manganese oxides and concluded that Mn^{3+} containing oxides seem to have highest activities when compared to those containing exclusively Mn^{2+} or Mn^{4+}, regardless of the crystal structure.[147] Moreover, it has been demonstrated that Mn^{4+} can catalyze the chemical disproportionation of the HO_2^- (reaction intermediate or byproduct) to molecular oxygen, which, in turn gets recycled for further reduction.[151] Consequently, the coexistence of Mn^{3+} and Mn^{4+} in the same metal oxide has been linked to enhanced activity and selectivity towards a total 4-electron ORR.

2.4.4. Perovskites

Perovskites are among the most widely studied mixed metal oxides with general chemical formula of $ABO_{3\pm\delta}$, where A represents a lanthanide cation, alkali earth metal cation, or a mixture of the two, and B is commonly a transition metal cation (or mix of more than one).[152] Figure 2.3a shows the crystal structure of a perfectly cubic perovskite without oxygen defects. The transition metals at the B-site are octahedrally coordinated to oxygen, while the A-site is 12-fold coordinated

to oxygen.[153] The main advantage of using this type of material is the ability to tune the oxidation state (generally between 2+ and 4+) of the transition metal by varying the A-site composition and/or the oxygen defect. This property has attracted a lot of interest in utilizing these materials in various chemical/electrochemical catalysis, like CO oxidation, NO oxidation, partial CH_4 oxidation to useful chemicals and oxygen electrocatalysis.[154-158]

Recently, interesting observations have been reported regarding the activity of perovskites toward ORR.[159-170] ORR catalytic trends of the substituted transition metal site $LaBO_3$ in alkaline media have been reported by many groups.[171-173] In general, Mn substituted/doped B-site showed the highest activity among the perovskites containing first series transition metals. One plausible explanation for this observation is the existence of Mn in mixed trivalent and quadrivalent states. ORR catalytic trends were also identified by other groups for A-site substituted $AMnO_3$ (A = $Pr_{1-x}Ca_x$,[174] $La_{1-x}Ca_x$,[175] and $La_{1-x}Sr_x$[176]; where $0.1 < x < 1$). All studies showed that the highest ORR catalytic activity was achieved when the valance state of Mn of +3.4 ($x \rightarrow 0.4$).[147] Suntivitch *et. al.*[171] proposed a catalytic descriptor for determining the electrocatalytic activity of perovskites (see Figure 2.3b), based on the occupation of the σ*-antibonding orbitals (e_g). Although, the proposed activity descriptor has led to insights, questions regarding the validity of this descriptor remain due to the fact that the perovskites used to establish this descriptor are prone to electrochemical reduction/oxidation within the ORR potential range.[173]

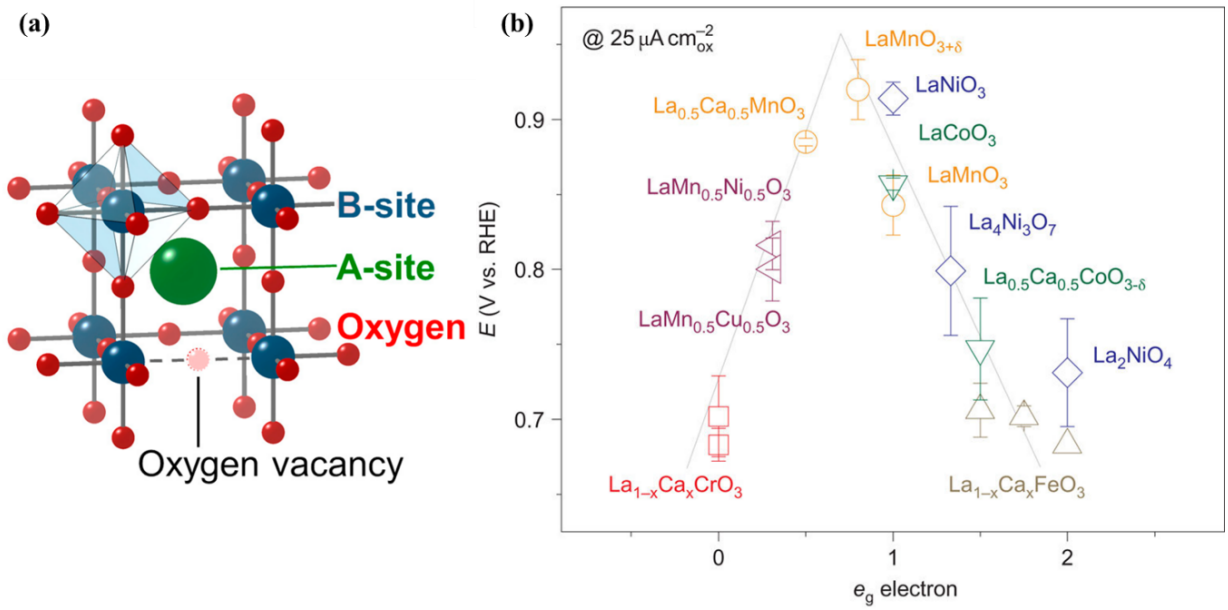

Figure 2.3 (a) Illustration of the unit cell of the perovskite structure.[153] (b) Experimental voltage at $25\mu A\ cm_{ox}^{-2}$ as function of estimated e_g occupancy of the $LaBO_3$ series and other relevant perovskites.[171]

2.4.5. First-series Ruddlesden-Popper oxides

First-series Ruddlesden-Popper (R-P) oxides with a formula $A_{n+1}B_nO_{3n+1}$ (where n = 1), share similar crystal structure to perovskites (ABO_3), with the additional existence of alternating rock-salt-type (AO) layers in the *c* crystallographic direction (see Figure 2.4).[177] Number of A_2BO_4 crystal structures are known, with $La_2NiO_{4+δ}$ being a prototypical example.[178] They are commonly used in high temperature electrochemical devices (such as solid oxide fuel cell, SOFC) due to their mixed ionic and electronic conductivities, as well as their excellent electrocatalytic performance toward ORR and OER.[179,180] A key factor of their high activity is the ability to accommodate oxygen interstitial sites in between adjacent rock-salt layers,[181-183] that leads to oxygen hyper-stoichiometry (δ) due to the variation in the oxidation state of the transition metal.[184,185] The substitution of lanthanum with other rare-earth metals with Nd and Pr ($Nd_2NiO_{4+δ}$ and $Pr_2NiO_{4+δ}$) leads to faster oxygen transport properties than their lanthanum contender.[186,187] In addition, the A-site can be doped with alkali-earth metals, such as $La_{2-x}Sr_xNiO_{4+δ}$,[188] $La_{2-x}Ba_xNiO_{4+δ}$,[189] and

$La_{2-x}Ca_xNiO_{4+\delta}$ which leads to changes in the oxygen transport and exchange properties of these materials.[190]

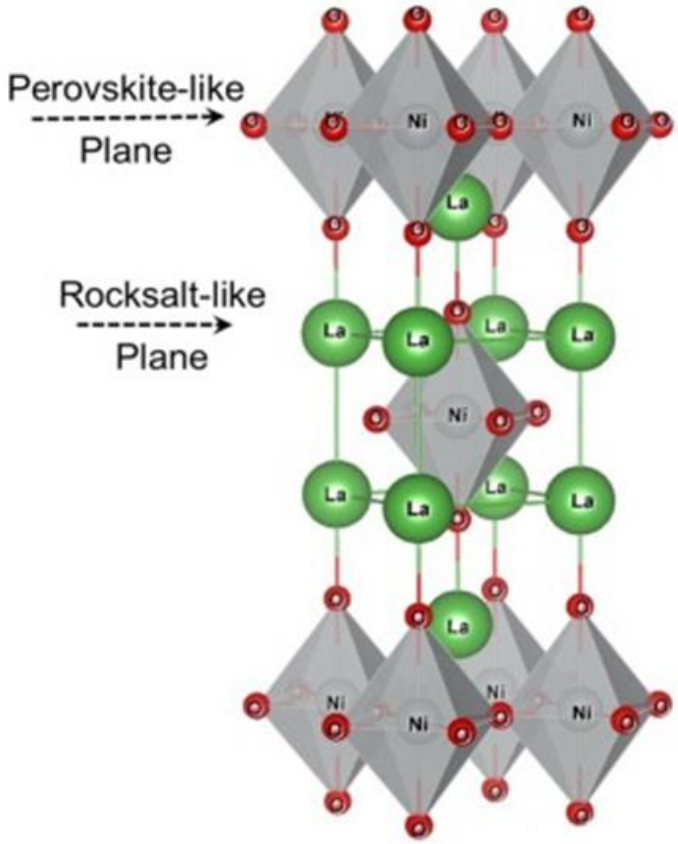

Figure 2.4 Stoichiometric crystal structure of A_2BO_4-type oxides, where A is lanthanum (green atoms) and B is nickel (gray atoms).[191]

The B-site metal of A_2BO_4 oxides can also be doped with transition metal cations, such as, Mn, Fe, Co, Cu and Zn.[183,192-194] Computational studies of various A- and B-site substituted/doped R-P structures were reported earlier by our group.[195] In this study, surface oxygen exchange rates for the investigated oxides show a volcano-like activity behavior with respect to the oxygen binding energy. The surface oxygen exchange kinetics has been shown to be an important characteristic feature of the oxygen electrochemistry at high to intermediate temperatures.[196-198] It was also concluded in the same DFT study, that the A-site terminated R-P oxides tend to have lower activity than that of B-site terminated R-P oxides. The catalytic activity of La_2NiO_4 in

relation to the surface termination of the oxide surface, was also proven experimentally by measuring the surface oxygen exchange activation energies in SOFC symmetric cells via impedance spectroscopy. Well-controlled rod-shape La_2NiO_4 nanoparticles La_2NiO_4 surface terminated by {001} B-site facets were synthesized which showed exceptional activity of ORR at intermediate temperatures.[179]

Thus far, the use of the first series R-P oxides has mainly focused on high temperature applications due to their fast oxygen transport properties. Very limited work[122,123] has been conducted to investigate their catalytic/electrocatalytic behavior at ambient temperatures. In the following chapters, we investigate the effect of varying A- and B-sites dopants of R-P oxides in low temperature oxygen electrocatalysis with the aim of developing fundamental insight that can guide their optimization for low temperature electrochemical systems.

CHAPTER 3. EXPERIMENTAL TECHNIQUES

3.1. Summary

In this chapter, a detailed description of the experimental methods and techniques employed in this thesis is presented. We also provide essential background regarding the theories and principles that govern the utilization of these techniques. Moreover, we report on the details the preparation of all electrocatalysts, cathode fabrication, Li-O_2 battery design and assembly and thin-film deposition for rotating ring-disk electrode studies of the oxygen evolution reaction (ORR).

3.2. Synthesis and Reactor Design

3.2.1. Reverse-Microemulsion Synthesis

The microemulsion method has been considered as an ideal liquid-phase method to synthesize inorganic materials with controlled nano-size characteristics.[199] Due to its distinctive properties (i.e. ultralow interfacial tension, large interfacial area and thermodynamic stability) the utilization of this synthesis technique is fairly large in the chemical and biological fields. Nanoparticles are exploited for many technological applications such as catalysts, high-performance ceramic materials, microelectronic devices, high-density magnetic recording and drug delivery. One of the advantages of this technique is the ability to control the nanoparticle characteristics, such as the particle size, geometry, morphology, homogeneity and surface area. In a typical reverse-microemulsion synthesis,[200] two separate reverse-microemulsion systems were first prepared, with each containing a quaternary reverse-microemulsion system composed of an oil phase hydrocarbon (aliphatic or aromatic), ionic surfactants, co-surfactants (generally 4–8 carbon chain aliphatic alcohol) and an aqueous phase with the desired metal ions or the precipitating agent. When the combination of the four components is appropriate, the solution

becomes clear spontaneously. In this study, we have used a quaternary system composed of cetyltrimethylammonium bromide (CTAB)/water/hexane/n-butanol and KOH as the precipitating agent. The two systems were mixed together, left to react through the exchange of ions followed by nucleation and precipitation. The collected solid-gel precipitates were then washed extensively with DI water and ethanol to remove the surfactant from the generated complex-metal hydroxide nanoparticles. The washed samples were then left to dry in static air for 12 hours at 80 °C, followed by calcination under inert atmosphere (see Figure 3.1). The reaction steps below outline the process of synthesizing $La_2NiO_{4+\delta}$ as an example of the nanostructured catalysts used in this thesis.

$$2\,La(NO_3)_{3\ (aq)} + Ni(NO_3)_{2\ (aq)} + 8\,KOH_{(aq)} \xrightarrow{Stirring\ at\ RT} [2\,La(OH)_3 \downarrow + Ni(OH)_2 \downarrow] + 8\,KNO_{3\ (aq)}$$

$$[2\,La(OH)_3 + Ni(OH)_2] \xrightarrow{Heating\ 5℃/min} [2La_2O_3 + NiO] + 3\,H_2O$$

$$[2La_2O_3 + NiO] \xrightarrow{825℃\ argon\ 5℃/min} La_2NiO_{4+\delta}$$

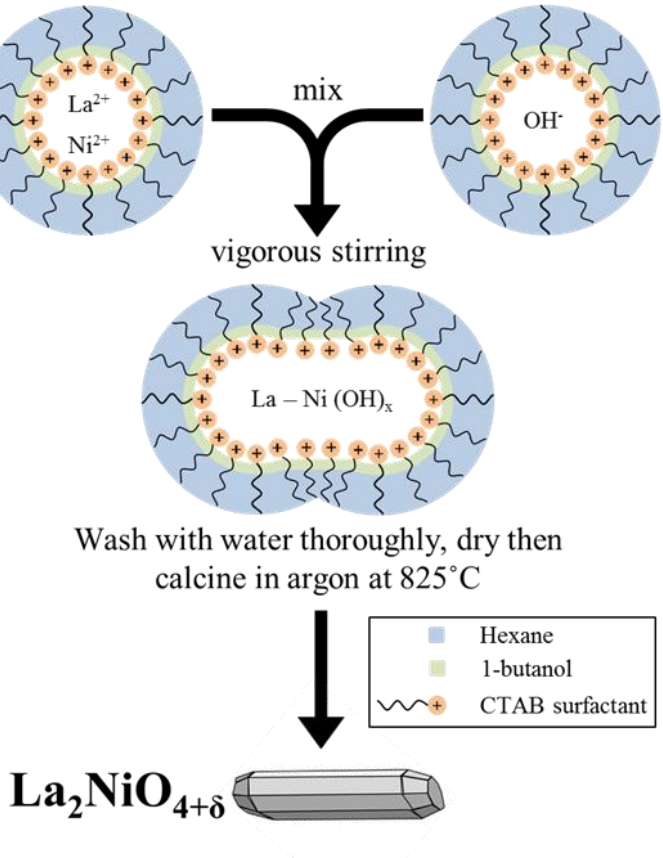

Figure 3.1 Schematic illustration of the synthesis of La_2NiO_4 nanorods.

3.2.2. Cathode Fabrication for Li-O_2 Battery

The cathode slurries used to fabricate the cathode electrode of the Li-O_2 batteries were prepared by mixing the active material (catalyst/carbon or carbon only) with a binder dissolved in a low vapor pressure solvent. Li-air battery cathodes require: (i) highly porous electronically conductive materials (carbon is the most common used material), as well as an active catalyst to efficiently and selectively catalyze the desired electrochemical reaction, (ii) the utilization of inert binder to hold the different components of the cathode together, (iii) the ability to hold liquid phase in their pores, (iv) sturdiness of the cathode support (commonly used supports are carbon paper and nickel mesh). The complete formation of this cathode is known as the Gas-Diffusion-Layer (GDL). The GDL allows the interaction of gas molecules, electrochemical active ions in the liquid phase and the transferred electron, in which they all meet at the triple-phase boundary of the electrode to initiate the electrochemical reaction.

Many cathode fabrication techniques have been utilized in the literature, including; tape-casting,[201] spraying,[202] impregnation and hot-pressing. All cathodes used in this study, have been fabricated by spraying the cathode slurry (carbon/catalyst/binder) on a carbon paper support (Toray TGP-H-030, FuelCell Store) taped to a glass plate and placed on a hot plate (~ 120 °C). All cathodes were dried under vacuum at 80 °C overnight, to insure full evaporation of the solvent used to make the slurry. Average weights of the final cathodes were recorded and labeled on every cathode, then stored for later use in an Argon-filled glove box.

3.2.3. Battery Design and Assembly

In this study, the Li-O_2 battery design was adopted from the literature[203] with the schematic shown in Figure 3.2. To ensure that our assembly is properly sealed, the cells were pressurized

with 30 psi argon and left over 2 days to monitor the drop in pressure overtime. No pressure drop was observed in any of the studies reported in this thesis.

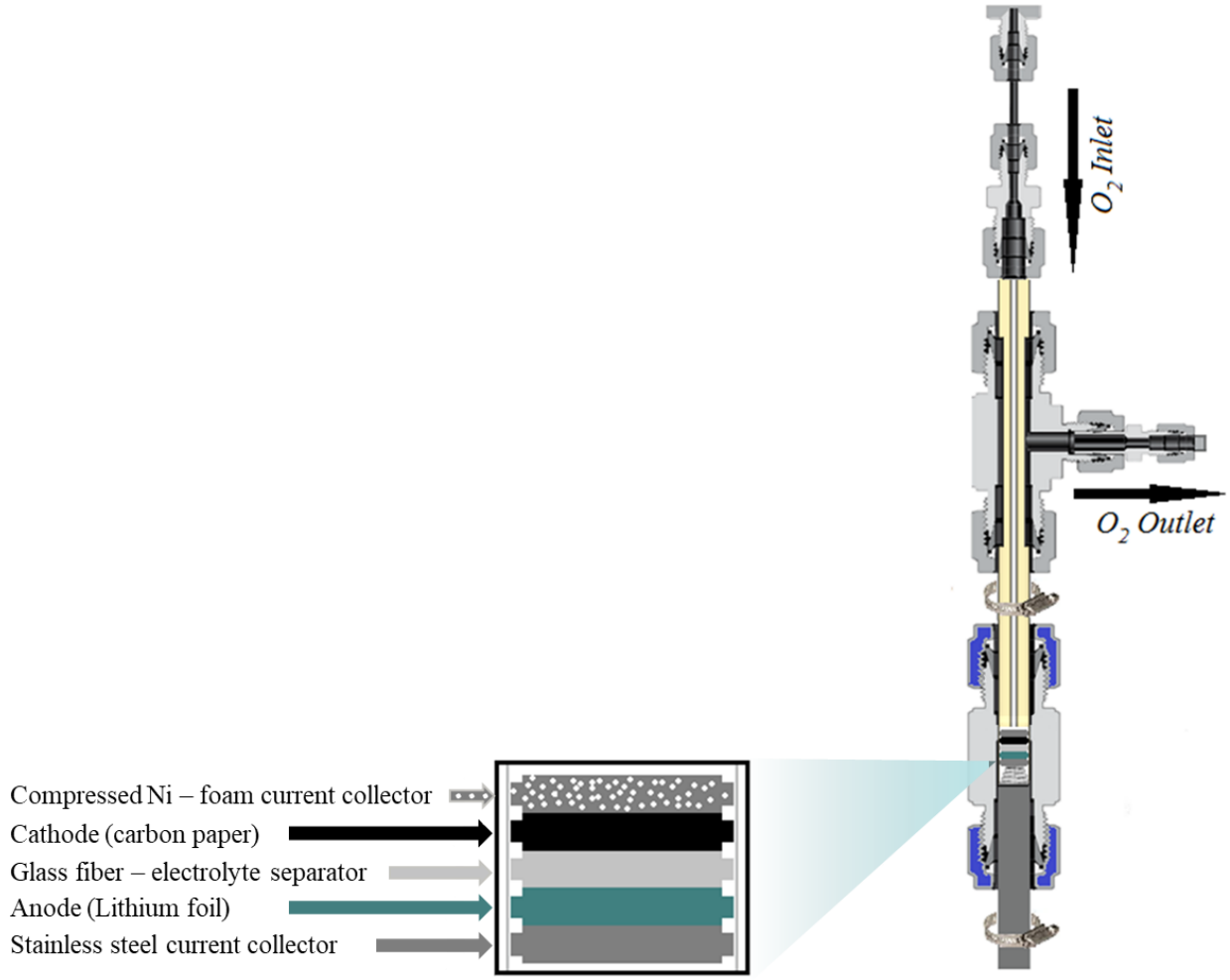

Figure 3.2 Schematic of the battery design and the contents of the button cell.

The electrolyte solution was prepared by dissolving lithium trifluoromethanesulfonate ($LiCF_3SO_3$, 99.995%, Sigma-Aldrich, dried at 130 °C under vacuum for 12 hours before use) in anhydrous tetraethylene glycol dimethyl ether (TEGDME, Sigma-Aldrich, dried using 3Å molecular sieves) using a 1:4 molar ratio, respectively. Lithium foil (0.75 mm thick, 99.9%, Sigma-Aldrich) was cut into ⅜" disk, polished, and supported on a stainless steel shim current collector. This was followed by placing a glass microfiber (Whatman®) separator on top and the addition of 100 µL of the electrolyte solution. The catalyst-containing side of the carbon paper was

then placed on top of the separator followed by a nickel mesh current collector in a shape of a porous flat disk, (Goodfellow USA). The cells were then sealed and their open circuit voltage was measured. All the above steps were conducted in an argon filled glove box with both oxygen and moisture levels less than 0.1 ppm.

3.2.4. Thin-Film preparation for Rotating Disk Voltammetry Studies

Catalyst slurries were prepared by ultrasonicating 15 $mg_{catalyst}$, 3 mg_{carbon} (XC-72R, FuelCell store), 64.5 μl_{nafion} (5 wt% nafion solution, ionpower) in 2.99 ml (3:1 DI water to 2-propanol (IPA) volume ratio) in an iced bath (to avoid nafion degradation) for 30 minutes.[204] Prior to thin-film deposition, the glassy carbon (GC) disk electrode was polished to a mirror-finish using 0.05 μm alumina suspension (Allied High Tech Products) on microfiber cloth (Buehler), followed by sonication in DI water and IPA. The GC disk substrate was left to dry at room temperature under nitrogen flow. 10 μL of the aliquot slurry was drop-casted on the 5 mm diameter GC disk electrode while rotating the disk at 700 rpm to provide better distribution of the catalyst film and to minimize the coffee-ring effect.[205] The final loadings of the catalyst, carbon and nafion were 250 $\mu g/cm^2$, 50 $\mu g/cm^2$ and 50 $\mu g/cm^2$, respectively. Figure 3.3 shows the drop-casted thin-film on a 5 mm glassy carbon disk electrode.

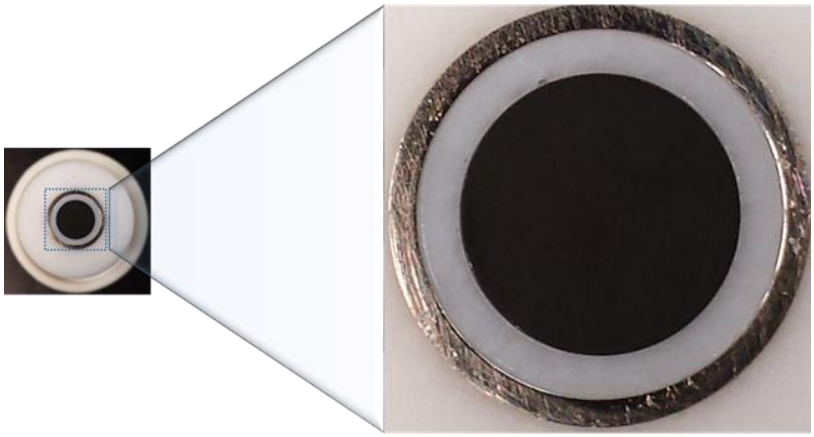

Figure 3.3 Catalyst/carbon thin-film deposited on glassy carbon disk electrode.

3.2.5. Rotating Disk Electrochemical Cell Design

The electrochemical cell utilized in this study is depicted in Figure 3.4. The cell was constructed from glass based on an in-house design with a maximum inside volume of 50 ml. The working electrode was composed of a concentric platinum ring/glassy carbon disk electrode tip, connected the rotor shaft. The shaft was mounted on a computer-controlled rotator, with a maximum rotation limit of 3000 rpm. The counter electrode used in this study was a high surface area platinum gauze, while the reference electrode was a mercury/mercury oxide redox couple in 20% KOH electrolyte. For the electrochemical stability tests, a teflon-based electrochemical cell was used similar to the design in Figure 3.4.

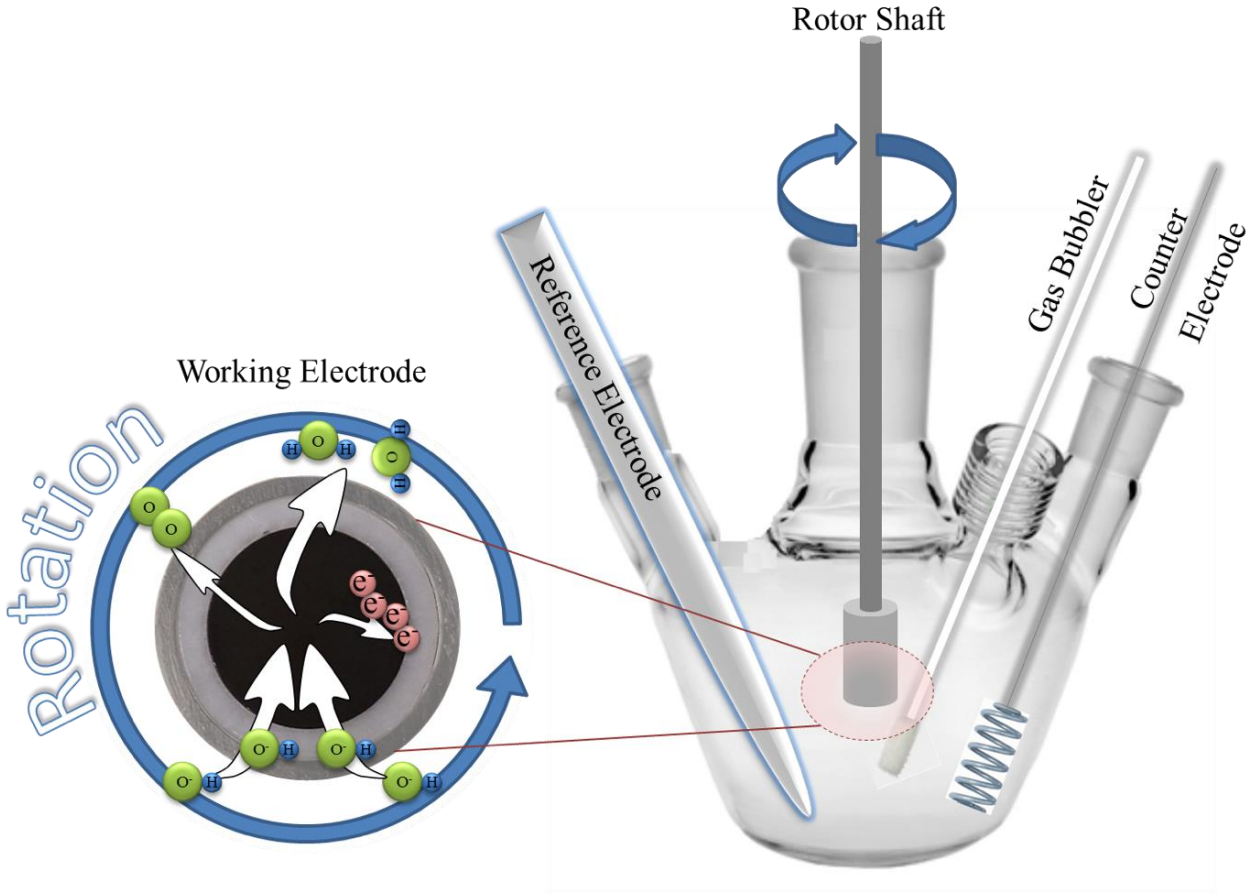

Figure 3.4 Rotating ring-disk electrochemical cell design

3.3. Structural and Physical Characterization

Multiple characterization techniques were employed in this study, to characterize the as-prepared catalysts, cathodes for Li-O_2 battery and thin-films for RDE experiments. These techniques are introduced in detail in the following sections.

3.3.1. X-Ray Diffraction (XRD)

X-ray diffraction is a non-destructive characterization technique utilized to identify the crystallographic structure of materials and is considered a key technique for the investigation of the bulk structure of materials. In heterogeneous catalysis the active sites are usually located on the solid surface, but the bulk structure is important since in many cases it dictates the termination of the surface. In a typical XRD experiment, X-rays are generated and emitted from an X-ray source to the targeted crystalline sample (see Figure 3.5). A number of X-ray reflections are scattered from the sample, each one associated to the lattice plane identified by the Miller indices *h, k, l*. The diffraction pattern occurs at an angular position (2θ), that depends on the related interplaner spacing (d) and on the X-ray wavelength (λ), as defined by the well-known Bragg's law (eqn 1). The crystallite size can be calculated from the broadening of the diffraction peaks using Scherrer's analysis (eqn 2).

$$n\lambda = 2d \sin\theta \qquad \text{(eqn 1)}$$

$$L = \frac{0.9\,\lambda}{\beta \cos\theta} \qquad \text{(eqn 2)}$$

where L is the crystallite size, λ is the wavelength of the incident X-rays (1.5418 Å for Cu-Kα) and β is the peak full-width at half maximum in radians.[206]

In this thesis, the XRD measurements were performed with a Cu-Kα source using a benchtop Brucker AXS PHASER II with 30 kW X-ray generator. The collected X-ray patterns

were analyzed using DIFFRAC software, which permits the appropriate peak assignment to previously reported structures in the database.

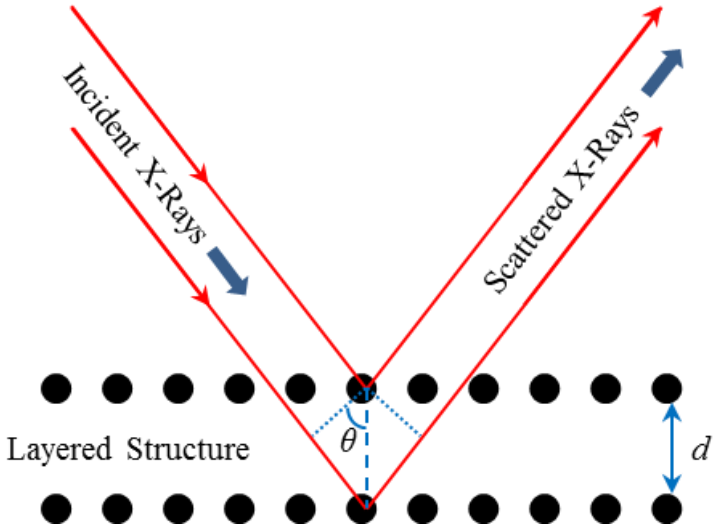

Figure 3.5 Schematic representation of the process that occurs in an X-ray diffraction experiment.

3.3.2. Field Emission Scanning Electron Microscopy (FESEM) and Energy Dispersive Spectroscopy (EDS)

Field emission scanning electron microscopy is the main characterization tool used to identify the morphology of the synthesized nanostructured materials in this study. The image is created by scanning (raster scan pattern) the sample with a high electron beam generated by a very sharp tip, field emission electron gun. Down the column and along the electron path, there are series of condenser lenses that focus the electron beam on the targeted sample. Two types of electrons are detected for imaging: secondary electrons (SE) and backscattered electrons (BSE). The secondary electrons are low energy electrons ejected from the k-orbitals (core level) of the sample atoms. While the backscattered electrons are high energy electrons that are elastically backscattered by the sample atoms. Both ejected electrons can be detected, and their signals can be interpreted to inform about sample's surface topography and elemental composition. The ejection of the secondary electron from the k-orbital to vacuum generates an empty electron state

or hole. This hole is filled with another electron from a higher energy level. The difference in energies between the two excited states is equivalent to the energy of the ejected photon detected. This detected energy represents a fingerprint of each element in the periodic table with Z > 3. This process is known as energy dispersive x-ray spectroscopy (EDS).

In this study, SEM and EDS were carried out using JSM-7600, JEOL at an accelerated voltage of 15kV. This microscope has a special resolution of a few nanometers and it is also equipped with an energy dispersive x-ray spectrometer (EDS)

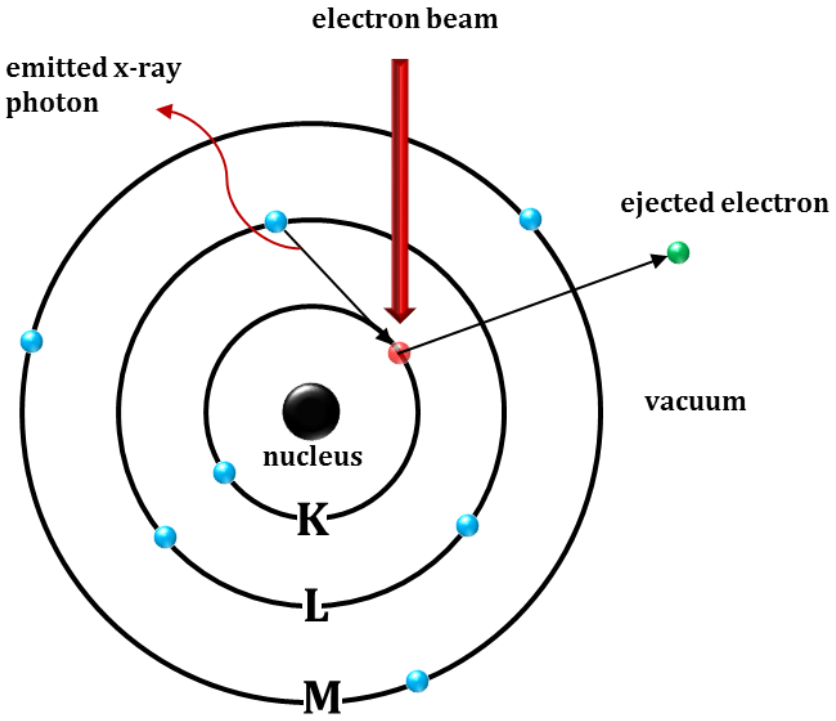

Figure 3.6 Schematic representation of the process that occurs in the energy dispersive x-ray spectroscopy experiment

3.3.3. X-ray Photoelectron Spectroscopy (XPS)

X-ray photoelectron spectroscopy is a surface sensitive technique that measures the elemental composition at the parts per thousand range and can determine the empirical formula, chemical state and electronic state of the elements that exist within the sample. A schematic representation of the XPS process is illustrated in Figure 3.7. Briefly, an X-ray photon (hν)

penetrates the sample surface and excites the electrons from the core levels of the atoms to the vacuum. The measured kinetic energy of the photoelectrons escaped from the sample surface (1 – 10 nm), is equivalent to the energy of the X-ray photon (hν) source minus the summation of the binding energy of the excited electrons in the core level and the work function (Φ). The work function corresponds to the difference in energies between the Fermi level and the vacuum level. The binding energy of the excited core electrons in the sample are well represented by the following equation:

$$E_{Binding} = h\upsilon - E_{Kinetic} - \phi \qquad \text{(eqn 3)}$$

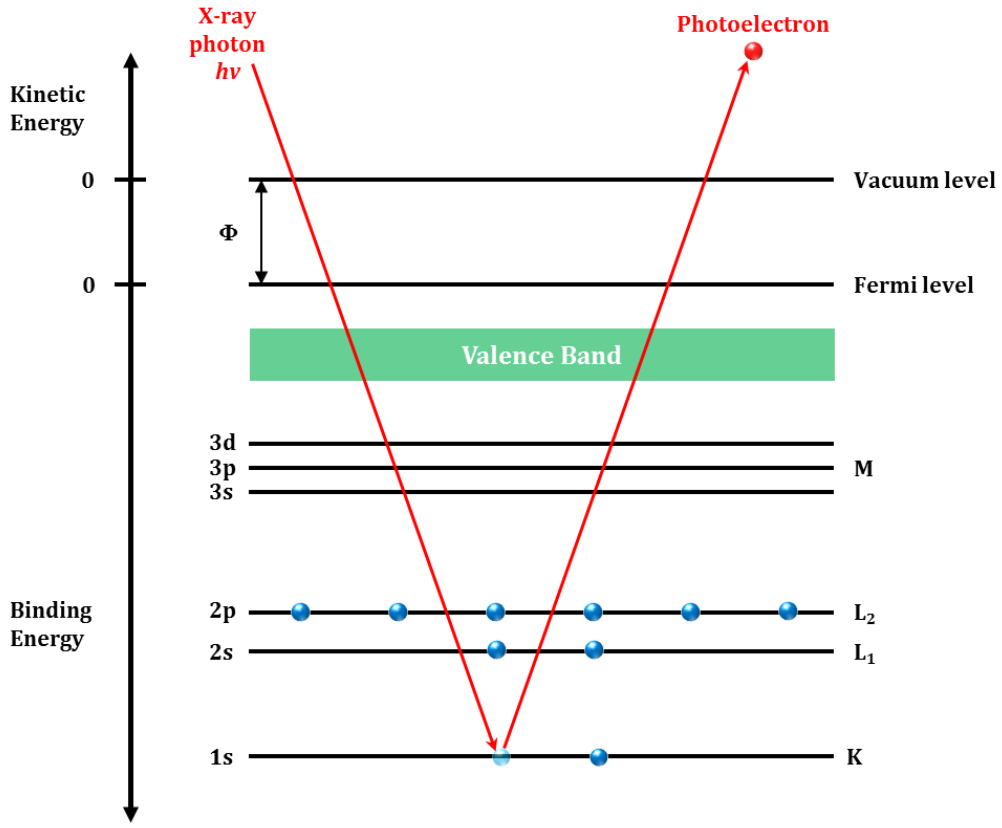

Figure 3.7 Schematic representation of the process that occurs in XPS experiment

In this thesis, a Kratos axis ultra XPS with monochromatic Al K-α source is used to determine the oxidation state of the transition metal in the synthesized metal oxides before and

after electrochemical studies. This XPS is part of the Michigan Center for Materials Characterization (MC^2) located at the University of Michigan (Ann Arbor, MI USA).

3.3.4. Scanning Transmission Electron Microscopy (STEM) and Transmission Electron Microscopy (TEM)

In TEM, the electron beam is generated by the electron gun (a hairpin-shaped tungsten filament) and accelerated by applying a certain negative high voltage to the cathode cap surrounding the filament. This allows the accumulation of electrons inside of the cathode cap and forming of an electron cloud. An anode located underneath the electron gun creates a positive attraction for the negatively charged electrons, causing them to accelerate through the small hole in the anode. This aperture serves as the first lens encountered by the electron. The accelerated electron beam is transmitted through the ultra-thin specimen containing the desired sample, and is focused and magnified using the objective and projector lenses, respectively. Selected area electron diffraction (SAED), is a TEM-accompanying crystallographic technique. In TEM, the thin specimen is subjected to a parallel beam of high-energy electrons. The wavelength of the high-energy electrons is a few hundredths of an angstrom, while the spacing between atoms in the examined crystalline sample is about a hundred times larger. Some electrons are scattered at different diffraction angles depending on the crystal structure of the sample, resulting in a characteristic diffraction spot patterns.[207-209]

Scanning transmission electron microscopy (STEM) combines the concept of both SEM and TEM, in which a focused electron beam (unlike TEM, where the electron beam is broad) scans the sample in a raster pattern. Accordingly, the electron beam interaction with the atoms in the sample correlated with the beam position to generate a series of images at each point in the sample probed by the beam. In STEM, images are formed either by the transmitted or the scattered

electrons. In the bright field (BF), transmitted electrons appear bright while scattered electrons appear dark. In dark field (DF), this contrast scheme is reversed. Depending on the interaction strength of the electron beam with the atoms in the sample, electrons are scattered strongly or weakly by the sample. Electrons scattered through low angles (LA) are known to be elastic (particle-like description) and coherent (wave-like description). The high angle (HA) electrons are inelastic because their energy is lost in collisions with atoms in the columns. Also, they are incoherent since a loss of energy equals an increase in wavelength. An annular dark field image formed by very high angle incoherent scattered electrons (scattered from the nucleus of the atoms) is very sensitive with respect to the atomic number of the atoms in the sample. This technique is known as high-angle annular dark-field imaging (HAADF). High atomic number atoms appear brighter due to the strong electron scattering. While atoms with low atomic number appear darker.[210]

In this study, TEM images were obtained using a JEOL 2011 200 k eV transmission electron microscope equipped with EDS detector. While STEM images were collected by JEOL 2010F analytical electron microscope with 200 kV accelerated voltage, equipped with a 0.17 nm HAADF detector and Gatan Imaging Filter (GIF) for electron energy loss spectroscopy (see detail about EELS below). Both pieces of equipment are part of the Michigan Center for Materials Characterization (MC^2) located at the University of Michigan (Ann Arbor, MI USA).

3.3.5. Electron Energy Loss Spectroscopy (EELS)

EELS is an elemental analysis technique, commonly, accompanying with TEM and STEM. In this measurement, the interaction between the incident electron and the atoms in the sample, results in core-electrons ejecting from the inner energy levels to the outer energy levels (unoccupied states above Fermi level). The energy required to eject core electrons to an

unoccupied state, has to be sufficiently high, to overcome the attraction of the nucleus and the core electrons. This attraction energy is known as the ionization energy which is uniquely defined for each specific atom and specific electron shell.[211] EELS provides better quantitative analysis than EDS. Also, EELS can detect lithium atoms, unlike EDS, where the characteristic radiation energy of the emitted X-ray photon is very low to detect, preventing the identification of lithium atoms by EDS spectroscopy.

3.3.6. Thermogravimetric Analysis (TGA)

Thermogravimetic analysis (TGA) is used to determine the weight change in a material as a function of changes in temperature and time. The detected gain or loss in mass, was induced due to changes in the sample physical characteristics (phase transition, adsorption, desorption and evaporation), as well as related chemical phenomena (chemisorption, thermal decomposition and oxidation). In this thesis, TGA was employed to determine the loading ratio of catalyst to carbon of the hybrid mixture used to fabricate cathodes for Li-O_2 batteries using a Q600 TGA from TA Instruments.

3.3.7. Brunauer-Emmett-Teller (BET) measurement

The specific surface area of a material can be measured by the well-known BET isotherm measurement. The BET theory extends the Langmuir's kinetic theory from monolayer adsorption to multilayer adsorption. The BET theory assumes that the uppermost molecules in adsorbed stacks are in dynamic equilibrium with the vapor. This means that when the surface is covered with only one layer of adsorbate, an equilibrium exists between that layer and the vapor; when two layers are adsorbed, the upper layer is in equilibrium with the vapor, and so forth. The analysis was carried out at liquid nitrogen temperature (77 K), over many relative pressures. In this thesis, prior to the BET analysis, all samples were dried and degassed under vacuum at 350 °C to provide more

accurate results. All BET N_2 physisorption measurements were conducted using the Micromeritics ASAP 2020 analyzer.[212]

3.4. Electrochemical Techniques

The open circuit voltage (OCV) of Li-O_2 batteries assembled inside an argon-filled glove box (as described in section 3.1.3) was measured using a multimeter with a high internal resistance. The battery cells were transferred anaerobically to the testing station and purged with ultra-high oxygen gas. Many electrochemical techniques were employed in this work with details provided in the next sections.

3.4.1. Galvanostatic Discharge/Charge

Galvanostatic discharge/charge performance is one of the most utilized electrochemical techniques in battery testing, that can be used to identify the maximum specific capacity ($mAh/g_{active\ material}$) measured at a constant discharge current density ($mA/g_{active\ material}$). Also, it provides an insight regarding the overpotential losses (defined as the voltage difference between the thermodynamic potential and operational voltage) both during discharge and charge. During discharge, the battery was subjected to a constant negative current, and the voltage response is recorded as a function of time. The discharge continues till the specified cutoff voltage is reached. The same response behavior was generated during recharge by applying a constant positive current.[19] Figure 3.8 shows a typical galvanostatic discharge/charge response of Li-O_2 over multiple cycles. The value of the applied current to the battery terminals has a direct effect on the observed voltage based on the polarization concept. These electrochemical measurements reported in this work were performed using a battery analyzer by MTI corp. Richmond, CA USA with a maximum absolute current value of 1 mA and voltage of ± 10 V.

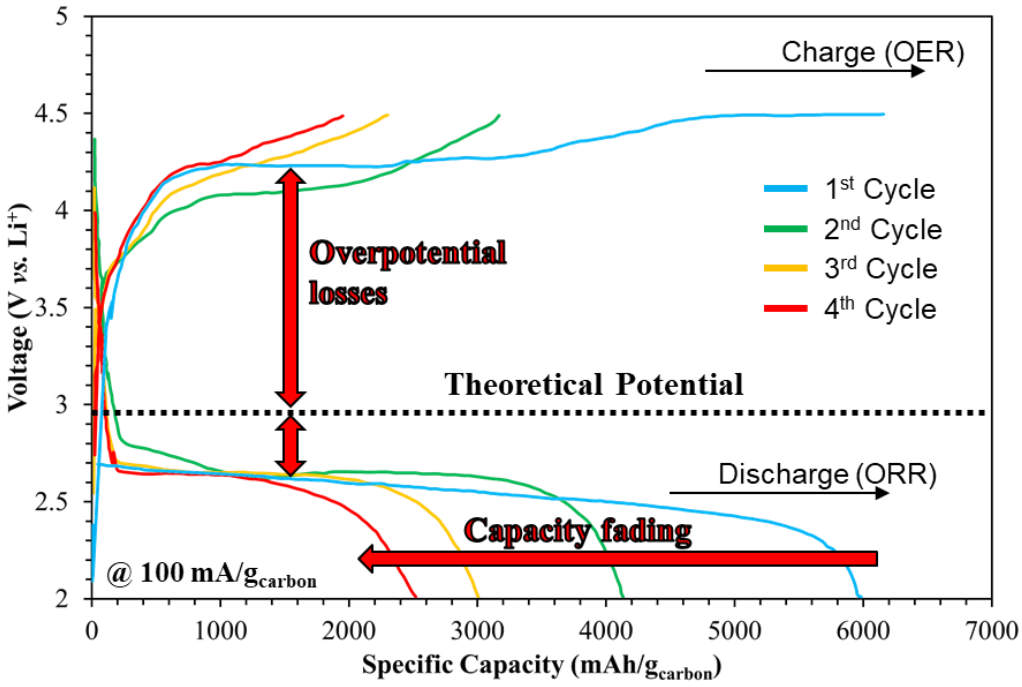

Figure 3.8 Four consecutive discharge/charge cycles of non-aqueous Li-O_2 cell with Ketjen black carbon cathode with 1M $LiPF_6$ dissolved in carbonated based electrolyte, using 100 mA/g_{carbon} current density.

3.4.2. Cyclic Voltammetry (CV)

Cyclic voltammetry is one of the most commonly used potentiostatic techniques. It involves scanning the potential of an electrochemical cell, starting from the system's OCV toward a more negative final voltage (cathodic scan) to identify the electrochemical activity of the reduced species (in the case of Li-O_2 battery, this represents the formation of lithium oxides). This is followed by a reverse scan (anodic scan) to a more positive final voltage to determine the electrochemical activity of the oxidized species (in this study, Li_2O_2). The observed peak current (i_p) generated throughout both scans is dependent on the scan rate (v), concentration of electrochemical active species (C), diffusion of the active species (D), number of electrons transferred (n), electrode surface area (A) and reaction temperature (T). This behavior is well described by the Randles–Sevcik equation (eqn 4).[19]

$$i_p = 0.4463\ nFAC\left(\frac{nF\upsilon D}{RT}\right)^{1/2} \qquad \text{(eqn 4)}$$

3.4.3. Slow Anodic Sweep Voltammetry (SASV)

Slow anodic sweep voltammetry shares the same concept with cyclic voltammetry with the exception of it involving a one directional potential slow scan (anodic scan) applied. The reason for scanning the potential slowly, is to provide enough time for the oxidation of the electrochemically active species. In this work, SASV measurements were employed to identify the onset (initial activity) and peak (maximum activity) oxidation potentials of preloaded Li_2O_2 on Li-O_2 battery cathodes. The investigated cathodes were composed of carbon-only and carbon/catalyst hybrid mixture. This experiment is explained more in detail in Chapter 5. SASV experiments were performed using Gamry Reference 3000 potentiostat (Gamry Intruments, USA).

3.4.4. Electrochemical Cycling

Electrochemical cycling is a powerful technique to investigate the stability and cyclability of commercially available batteries or promising new-concept battery technologies. This technique is similar to the galvanostatic discharge/charge, with the exception of involving a limited discharge capacity. It provides valuable information regarding the capacity retention (the ratio between the discharge and charge capacities), voltage efficiency (the round-trip voltage difference between the discharge and charge behavior) and the active material's electrochemical and structural stabilities.

3.4.5. Electrochemical Potential Impedance Spectroscopy (EPIS)

EPIS is a powerful technique used in electrochemistry. Its main application is to identify the resistances associated with every electrochemical reaction step in a complex mechanism. It can also be expanded to distinguish many important kinetic parameters, such as, activation energy,[180] reaction rate constant[213] and reaction order, by constructing an electrical circuit representation of the targeted reaction. In general, EPIS involves the introduction of an alternating potential with specific amplitude at fixed cell voltage while varying the frequency of the excitation signal, and

measuring the difference in the phase change of the detected and applied sinusoidal signals.[19] In this work, EPIS was used to identify the ohmic resistances of the system. This value was used to correct the voltage against these ohmic losses. The corrected voltage is solely related to the kinetic behavior of the electrochemical reaction occurring at the surface of the heterogeneous catalyst being investigated. EPIS measurements were performed using Gamry Reference 3000 potentiostat (Gamry Intruments, USA).

3.4.6. Rotating Disk and Ring-Disk Electrode Voltammetry (RDE and RRDE)

RDE and RRDE are hydrodynamic forced-convection electrochemical experiments. The working electrode rotates during experiments inducing a laminar flux of the electrochemical active species to the electrode surface to sustain a constant concentration of the analyte near the electrode surface, where the electrochemical reaction takes place. Linear sweep voltammograms were recorded at various rotation speeds (angular velocities). The total current (i_d) generated during the experiment is related directly to serial resistances of two major processes; one associated with the current generated due to the mass-diffusion limitations through the hydrodynamic boundary layer (i_{dl}), and the second related to the current generated due to the inherent catalytic activity of the investigated electrocatalysts (i_k). This is simply depicted in equation 5 (Koutecký–Levich equation).

$$\frac{1}{\mathrm{i_d}} = \frac{1}{\mathrm{i_k}} + \frac{1}{\mathrm{i_{dl}}} \qquad \text{(eqn 5)}$$

The diffusion-limited current density (i_{dl}) is obtained using Levich equation (eqn 6):

$$\mathrm{i_{dl}} = 0.62\mathrm{nFC_{O_2}D_{O_2}^{2/3}}\upsilon^{-1/6}\omega^{1/2} = \mathrm{B}\omega^{1/2} \qquad \text{(eqn 6)}$$

where n is the number of electrons involved in the oxygen reduction reaction (in this study, ORR is the targeted reaction), F is the Faraday constant (96485 C/mol), C_{O_2} is the oxygen concentration of a fully saturated 0.1 M KOH electrolyte (1.21×10^{-6} mol cm^{-3}), D_{O_2} is the oxygen diffusion

coefficient in 0.1 M KOH (1.9×10^{-5} cm^2 s^{-1}), υ is the kinematic viscosity of the electrolyte solution (0.01 cm^2 s^{-1}) and ω is the rotation rate (rad s^{-1}).[19]

In RRDE, a concentric active ring electrode is embedded just outside the disk electrode. The ring electrode is commonly utilized by applying a constant potential sufficient to cause oxidation of the reduced species that are swept away from the disk electrode. The collection efficiency is solely dependent on the ring-disk geometry and the Teflon spacing isolating the two electrodes (see the following section for collection efficiency determination). A simplified representation of the RRDE experiment is illustrated in Figure 3.9.

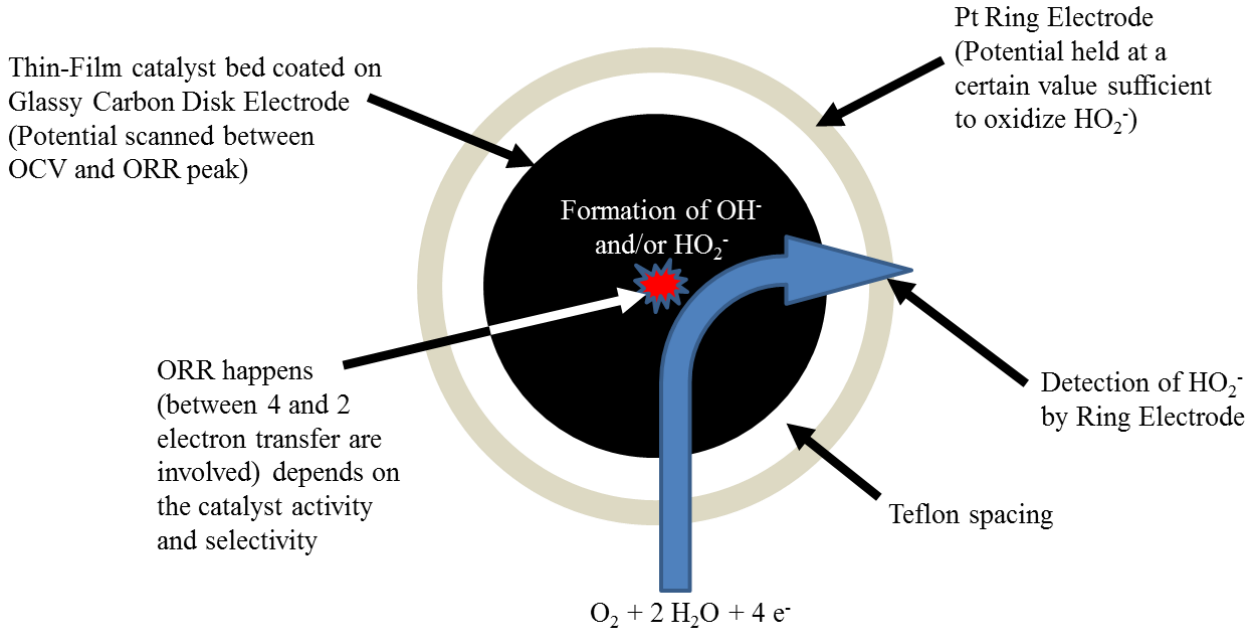

Figure 3.9 Illustration of the oxygen reduction reaction occurring during RRDE experiment

The percentage of hydroperoxide generated during the reaction and the number of electrons involved in ORR were calculated by the following equations:

$$\%HO_2^- = \frac{2\frac{I_R}{N}}{I_D + \frac{I_R}{N}} \times 100\% \qquad \text{(eqn 7)}$$

$$n = \frac{4\ I_D}{I_D + \frac{I_R}{N}} \qquad \text{(eqn 8)}$$

where I_R and I_D represent the current generated on the ring and the disk electrodes, respectively, and N is the collection efficiency of the ring electrode.

In this thesis, RDE and RRDE were performed by utilizing a bipotentiostat electrochemical system from Pine Instruments, North Carolina USA integrated with an electrode shaft rotator, and controlled by Aftermath software. Nine perfect square rotation speeds were chosen between 100 and 2500 rpm, while scanning the disk potential linearly from 1.2 to 0.05 V (ORR region), and the ring potential was held constant at 1.25 V for hydroperoxide detection generated by the disk electrode.

3.4.7. Ring Electrode Collection Efficiency Determination

The collection efficiency of the ring electrode is an important value incorporated in the calculation of the number of electrons involved in the electrochemical reaction. This value is solely dependent on the ring-disk electrode geometry.[19] In order to utilize the ring electrode in the RRDE studies, the value of the collection efficiency has to be determined. The determination of the collection efficiency is done experimentally by utilizing a reversible one-electron redox couple. $Fe(CN)_6^{3-/4-}$ is the most commonly used redox couple. In this experiment, 4 mmol of $K_3[Fe(CN)_6]$ was dissolved in 30 ml Ar-saturated 0.1 M KCl electrolyte. Hg/HgO was used as the reference electrode and Pt-gauze was used as the counter electrode. Chronoamperometry graphs (see Figure 3.10) were collected at various rotations by holding the disk potential at 1.5 V and the ring potential at 0.1 V. The potential values were chosen at very well defined diffusion limited regions of the redox reaction. The collection efficiency of the Pt-ring (N) was calculated by taking the ratio of the current generated on the ring electrode (i_R) to the current generated on the disk electrode (i_D). This procedure was performed frequently to insure accurate measurements of RRDE experiments (see Table 3.1).

$$N = -\frac{i_R}{i_D} \qquad \text{(eqn 9)}$$

Table 3.1 Collection efficiency values at varying rotational speeds

Trial	Collection Efficiency (N)				Mean
	400 rpm	900 rpm	1600 rpm	2500 rpm	
1	0.248454	0.249208	0.247472	0.243264	0.2471
2	0.241532	0.241628	0.239932	0.235813	0.239726
3	0.246437	0.245686	0.241795	0.240477	0.243599

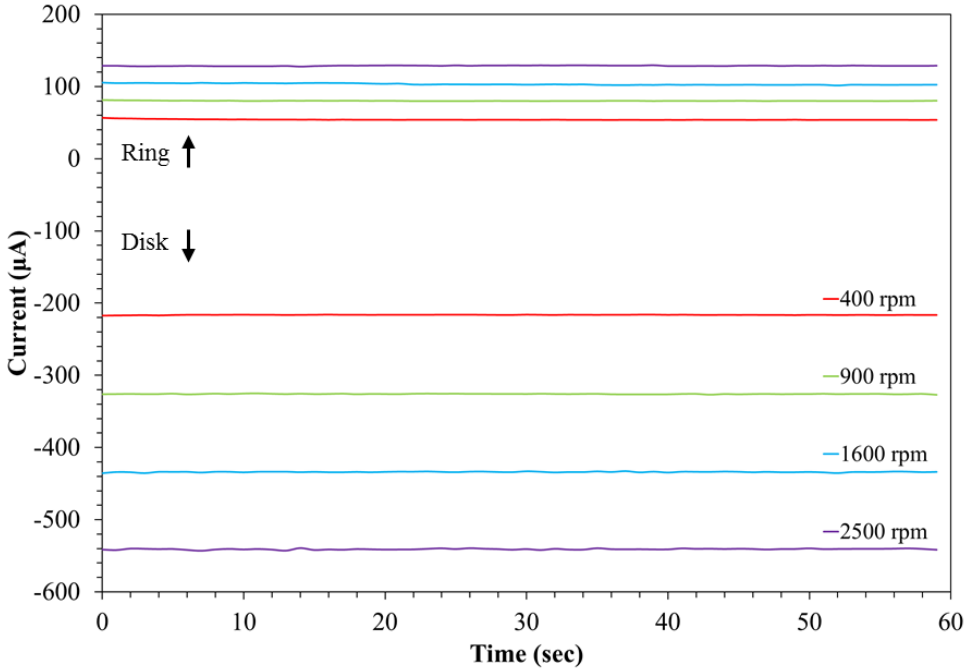

Figure 3.10 Chronoamperometry experiment of Pt-ring and glassy carbon disk electrodes in 0.1 M KCl electrolyte containing 4 mmole of $K_3\{Fe(CN)_6\}$. The ring and disk electrodes were held at a constant potential of 1.5 V and 0.1 V, respectively.

3.4.8. Hg/HgO Reference Electrode Calibration

In this thesis, Hg/HgO (in 20 wt.% KOH) was used as the reference electrode. This electrode was calibrated against the reversible hydrogen electrode (RHE) between experiments. First, the electrolyte (30 ml of 0.1 M KOH) was fully saturated with ultrahigh purity hydrogen gas (99.999 %, Airgas) for about 30 minutes. The working electrode employed during the calibration

was Hg/HgO, while the reference and counter terminals were both connected to a Pt-gauze electrode. Prior to the experiment, the open circuit potential was recorded for 6 minutes (see Figure 3.11 a). Cyclic voltammograms were collected at 0.1 mV s^{-1} scan rate in a 40 mV potential window around the OCV value. The potential values of both positive and negative scans of the CV were averaged out at 0 μA current value as shown in Figure 3.11 b.[146]

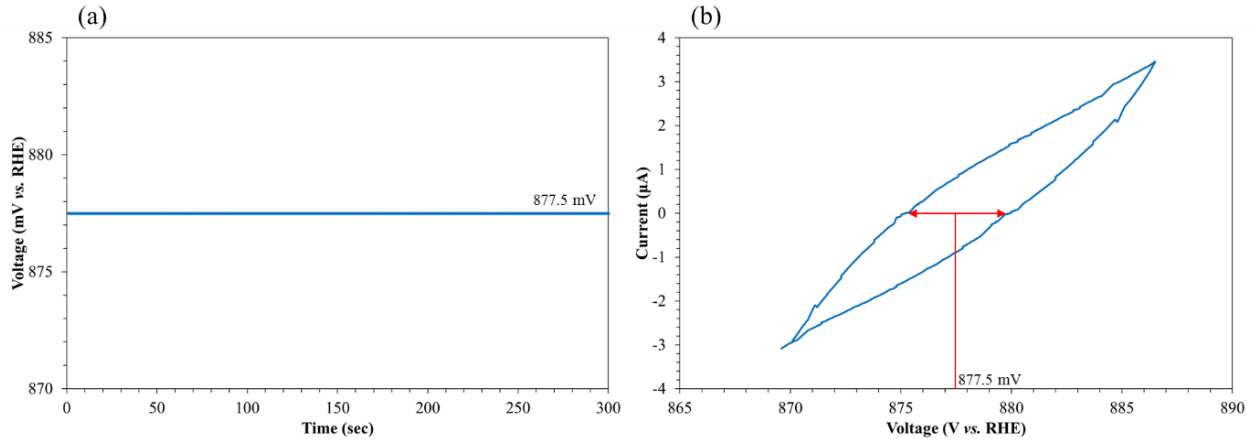

Figure 3.11 (a) OCV plot of H_2-saturated 0.1 M KOH, (b) cyclic voltammogram of H_2-saturated 0.1 M KOH electrolyte using Pt-gauze as both working and reference electrode and Hg/HgO as counter electrode.

3.4.9. Hydrogen Peroxide Electrochemical Reduction Reaction (HPRR)

Electrochemical reduction of H_2O_2 was performed using the same RDE setup by injecting 25mM of H_2O_2 to the existing argon-saturated electrolyte (0.1 M KOH), and scanning the potential from 1.2 to 0.05 V at 10 mV s^{-1} at various rotation rates. This experiment was employed to obtain insightful information about the catalytic activity of the various catalysts towards HPRR. Hydroperoxide is a well-known reaction intermediate that involves in the ORR. Further explanation of this experiment is provided in Chapter 6.

CHAPTER 4. INVISTIGATION OF THE ELECTROCATALYTIC ACTIVITY OF A-SITE DOPED NICKELATES IN LI-O_2 BATTERY

4.1. Summary

In this chapter, the electrochemical investigation of the catalytic activity of lanthanide nickelate oxides Ln_2NiO_4 (Ln = La, Pr, Nd and their combinations) toward ORR/OER in Li-air batteries is presented. The electrocatalytic activity trend developed suggest that La_2NiO_4 exhibits the best performance among all the investigated lanthanide oxides. We find that the electrochemical performance of La_2NiO_4 could be further improved by doping the La-site with an alkaline earth metal, such as barium. We show that $Ba_{0.25}La_{1.75}NiO_4$ exhibits the best discharge capacity and lowest OER potential when compared to undoped La_2NiO_4, $Sr_{0.25}La_{1.75}NiO_4$ and $Ca_{0.25}La_{1.75}NiO_4$. The stability of these oxide electrocatalysts is demonstrated under electrochemical conditions. These findings show promise for utilizing first-order Ruddlesden-Popper series oxides as efficient non-precious metal-based cathode electrocatalysts for high-energy storage systems.

4.2. Introduction

Electrochemical energy storage has become very important in recent years due to the increase in interest in electrical vehicles and an avenue for storing the energy generated from renewable resources, such as the sun and wind. Li-air (Li-O_2) batteries are among the most promising energy storage technologies as they theoretically can provide high specific capacity (3.86 Ah/g) and energy density (~11,140 Wh/kg) at a low cost.[4,12,214-217] While promising, Li-O_2 batteries have faced a number of challenges with achieving their theoretical specific capacity/energy density and maintaining their long-term stability over cycling. Among the different structural arrangements of the Li-O_2 batteries, nonaqueous/aprotic systems are among the

most attractive since they eliminate the need for active reagents, have relatively simple structures and are the most active.[218,219]

The most commonly used cathode materials for Li-O_2 batteries are mesoporous carbons due to their low cost, light weight, good storing capability for Li_2O_2, and excellent electron conductivity.[214,220,221] One drawback with carbon cathodes is their low activity toward catalyzing the electrochemical reactions.[43,222] The high overpotential losses during OER (recharge) has inspired the scientific community to find better alternatives that are capable of lowering the potential gap and are earth-abundant materials rather than the expensive noble metals.[223,224] An approach to reduce the overpotential losses in these batteries is to incorporate an active OER electrocatalyst into the carbon-based cathodes. Literature reports have shown that the addition of an active OER electrocatalyst to the carbon electrode can significantly reduce the charging potential.[4,43,121,225] Unfortunately, most of the promising OER electrocatalysts for Li–O_2 batteries contain precious metals, presenting a significant challenge for commercialization.[41,47,53,101,102,226] Recent reports have shown that non-precious metal oxide systems, such as perovskite,[105,106,227-229] hollandite[230] and nickelate oxides,[123,231] can also lower the cell potential during charging. While these studies have shown promise, limited understanding of the factors that lead to the lowering of the overpotential losses in these metal oxide systems exist.

In this chapter, we study the effect of the A-site composition of nickelate oxides on the electrochemical performance toward ORR and OER when incorporated in the cathode of Li-air batteries. It has been shown that changes in the A-site composition lead to changes in the structure of nickelate oxides that significantly affect their catalytic activity at high temperatures.[232] We report that as you move across the lanthanides in the periodic table from La to Pr to Nd, the

catalytic activity toward the electrochemical reactions in Li-O_2 batteries decreases, with the best performance exhibited by lanthanum nickelate.

4.3. Experimental

4.3.1. Catalysts Synthesis

All chemicals were purchased and used as commercially received without further purification. The Ln_2NiO_4 (Ln = La, Pr, Nd and their combinations) electrocatalysts were prepared using a reverse-microemulsion method.[233,234] In a typical synthesis, two separate reverse-microemulsions were first prepared, with each containing a quaternary reverse-microemulsion system composed of cetyltrimethylammonium bromide (CTAB)/water/hexane/n-butanol. One microemulsion was formed by mixing 4 mmole of Ln-nitrate hexahydrate and 2 mmole of nickel nitrate hexahydrate (99.999%, Sigma–Aldrich) in 0.8 ml of deionized water, and the other one was formed by mixing 1.155 g of KOH (85%, Sigma–Aldrich) in 5.6 ml of deionized water. In each microemulsion system, the amount of CTAB, hexane and n-butanol was fixed at 11 g, 56 ml and 11 ml, respectively. After the solutions were well mixed, the microemulsion system containing the metal salts was added to the system containing the base under stirring (1100 rpm). The mixture was maintained under the same conditions for 4 hours to form the gel suspension containing the precipitated metal hydroxide. The solid gel was collected by centrifugation (8000 rpm, 3 min). This was followed by washing three times using deionized water and three more times using ethanol. The solid gel was then dried under air at 80 °C overnight. The obtained solid was calcined at 1050 °C (2 °C/min heating rate from room temperature) for 2 hours under static air atmosphere. Alkali-earth metal (Ca, Sr and Ba) doped lanthanum nickelate oxides with a dopant ratio of 12.5 % were synthesized using the same method as mentioned above.

4.3.2. Cathode Preparation

Initially, the prepared electrocatalysts were sonicated in ethanol (0.1 g catalyst in 3 ml ethanol) for one hour. The solution with the dispersed electrocatalyst was then impregnated (with the desired loading) onto the mesoporous carbon powder (Ketjen Black EC600JD, Akzo Nobel). This was followed by drying at 75 °C and 110 °C for 20 minutes and 2 hours, respectively. The mass loading of catalyst on carbon support was verified by TGA. In a typical procedure for the preparation of the Li-O_2 cathode, 0.1 g of polyvinylidene fluoride (PVDF, Sigma-Aldrich) binder was first dissolved in 8 ml of N-methyl-2-pyrrolidone (NMP, 99.5%, Sigma-Aldrich) and stirred overnight. This was followed by the addition of the appropriate amount of the catalyst-carbon mixture (40 wt% catalyst loading) and stirring for an additional 24 hours. The slurry was then sprayed using an airbrush on one side of the carbon paper (Toray TGP-H-030, FuelCell Store) to yield a final carbon loading of 0.77 ± 0.01 mg/cm^2 for all the cells reported in this chapter. This was followed by drying at 115 °C for 3 hours. Carbon paper was used as the cathode support in all our studies. Our findings show, consistent with literature reports,[235] that the carbon paper exhibits a very low discharge capacity (approximately 70 mAh/g) when used as the cathode. Therefore, it is safe to assume that the impact of the carbon paper on the discharge capacity of the cells is negligible. Finally, the prepared cathodes were dried overnight under vacuum at 80 °C along with the SwagelokTM cell assembly.

4.3.3. Battery Assembly

The electrolyte solution was prepared by dissolving lithium trifluoromethanesulfonate ($LiCF_3SO_3$, 99.995%, Sigma-Aldrich, dried at 130 °C under vacuum for 12 hours before use) in anhydrous tetraethylene glycol dimethyl ether (TEGDME, Sigma-Aldrich, dried using 3Å molecular sieves) using a 1:4 molar ratio, respectively. Lithium foil (0.75 mm thick, 99.9%,

Sigma-Aldrich) was cut into ⅜" disk, polished, and supported on a stainless steel shim current collector. This was followed by placing a glass microfiber (Whatman®) separator on top and the addition of 100 μL of the electrolyte solution. The catalyst-containing side of the carbon paper was then placed on top of the separator followed by a nickel mesh current collector (in a shape of a porous flat disk, Goodfellow USA). The cells were then sealed and their open circuit voltage was measured. All the above steps were conducted in an argon filled glove box with both oxygen and moisture levels less than 0.1 ppm.

4.3.4. Characterization

The determination of the electrocatalyst loading in catalyst-carbon mixture in each cathode was performed by thermal gravimetric analysis (TGA, Q600, TA Instruments), the sample was loaded in an alumina holder and heated under continuous air flow to 800 °C using 10 °C/min ramping rate. The X-ray diffraction (XRD) characterization of each sample was performed with a powder X-ray diffractometer (Smartlab, Rigaku Inc., Japan) using Cu Kα radiation (λ = 0.15418 nm). The XRD pattern of fresh LNO was recorded over 2θ values of 20 º to 80 º at a rate of 2 º/min. The morphology of each catalyst was analyzed using a field-emission scanning electron microscopy (SEM, JSM-7600, JEOL Inc., Japan) at the accelerating voltage of 15 kV, while the composition of the A-site ratio was verified by Energy-dispersive X-ray spectroscopy (EDXS).

4.3.5. Electrochemical Testing

Galvanostatic Full Charge-Discharge Experiments: The assembled cells were connected to a flow of ultra-high purity oxygen (99.999%) for 30 minutes before testing. All the testing experiments were conducted using a battery analyzer (MTI corp. Richmond, CA) under a current density of 50 mA/g_{carbon}. The reported specific capacities were normalized based on the carbon weight of each cathode, consistent with literature reports.[43,53,121]

Cyclic Voltammetry (CV) Experiments: The same cell design as the one discussed above was used for these experiments. The assembled cells were left under open circuit potential (OCV) conditions for 30 minutes under a flow of oxygen to equilibrate, before the experiments were started. The voltammograms were recorded by sweeping the potential from the OCV negatively to 2 V (vs. Li^+) using 0.1 mVs^{-1} scan rate (referred to as cathodic scans), followed by reversing the scan to the positive direction to a cutoff voltage of 4.5 V (referred to as anodic scans). Background scans used the same experimental conditions but when exposed to an argon atmosphere instead of oxygen were also conducted to verify the lack of activity and identify the potentials at which the electrolyte starts to decompose as well.

4.4. Results and Discussion

4.4.1. Catalyst Synthesis

Nickelate oxides, as discussed above, are layered oxide structures containing alternating rocksalt-like and perovskite-like layers. While these oxides have been used in solid oxide electrochemical cells[236,237] and Li-air[123,231] cathodes, little is known about the factors that govern their catalytic/electrocatalytic activity. In this study, we have utilized a reverse-microemulsion synthesis route, briefly, the synthesis involves the co-precipitation of the desired metal hydroxide by mixing two microemulsion systems, one that contains the metal salt and the other contains the hydroxide ions. The reaction was carried out at room temperature under vigorous stirring, the nucleation of the hybrid metal hydroxide starts almost immediately while a complete yield of the final product takes about four hours. The precipitated gel was washed with deionized water to remove the surfactant that encapsulates the metal hydroxide. While the pure La_2NiO_4 was able to form pure phase at calcination temperatures lower than 835 °C, in the case of the oxides containing Nd and Pr, the pure crystal phases of Ruddlesden-Popper oxides were only obtained at higher

calcination temperatures (more than 1000 °C). The high calcination temperature of these oxides prevents control over morphology. Therefore, in order to maintain the same geometric structure among all the lanthanide oxides, all synthesized catalysts were calcined under the same conditions (1000 °C).

Figure 4.1 shows that pure crystal phases for all the nickelate oxides with different A-site compositions were obtained. Standard reported X-ray spectra were plotted for comparison. Scanning electron microscopy (SEM) was used to characterize their geometric structures. Figure 4.2 (a-e) shows that the particle geometry and size is fairly similar among the Ln_2NiO_4 oxides synthesized suggesting that the differences in the electrochemical activity will be mainly induced due to the differences in their A-site compositions. Energy dispersive spectroscopy (EDS) was used to verify the A- and B-site compositions in the oxides.

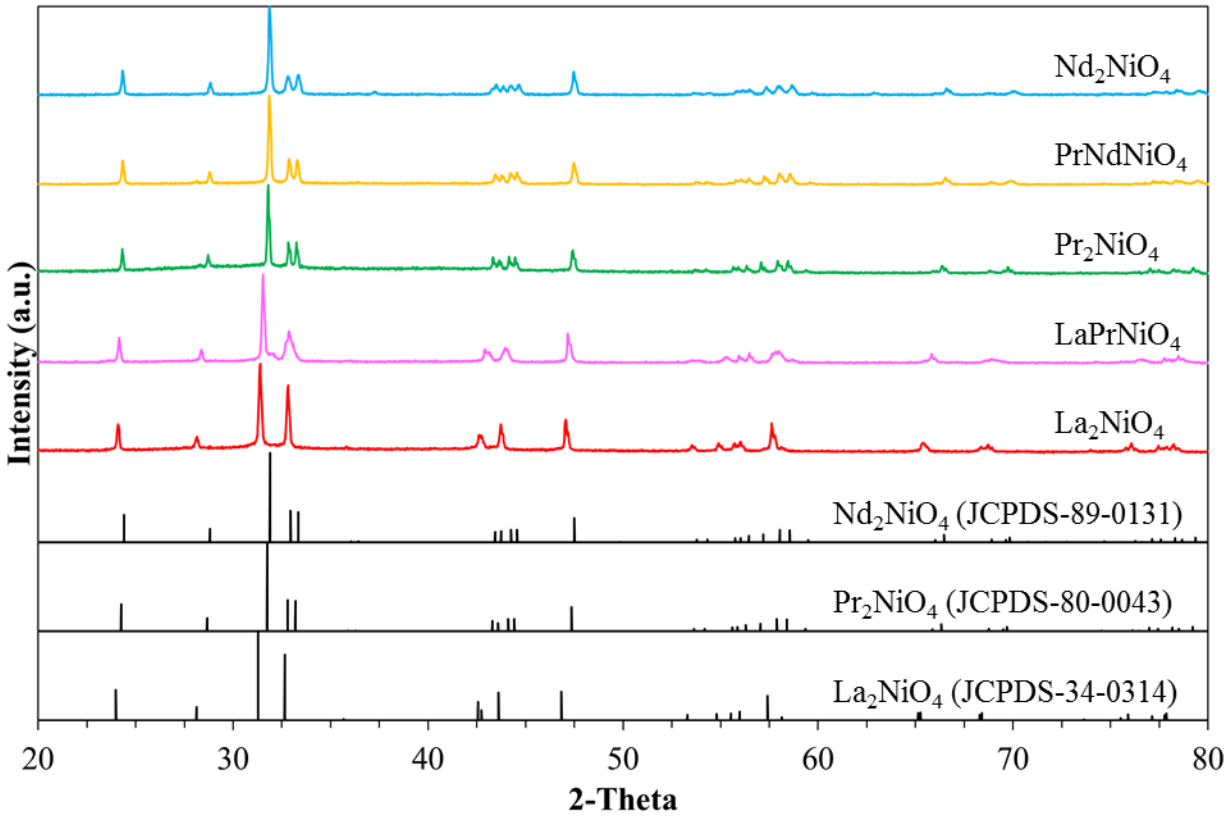

Figure 4.1 X-ray diffraction patterns of the synthesized lanthanide nickelate catalysts and their respective standard JCPDS data

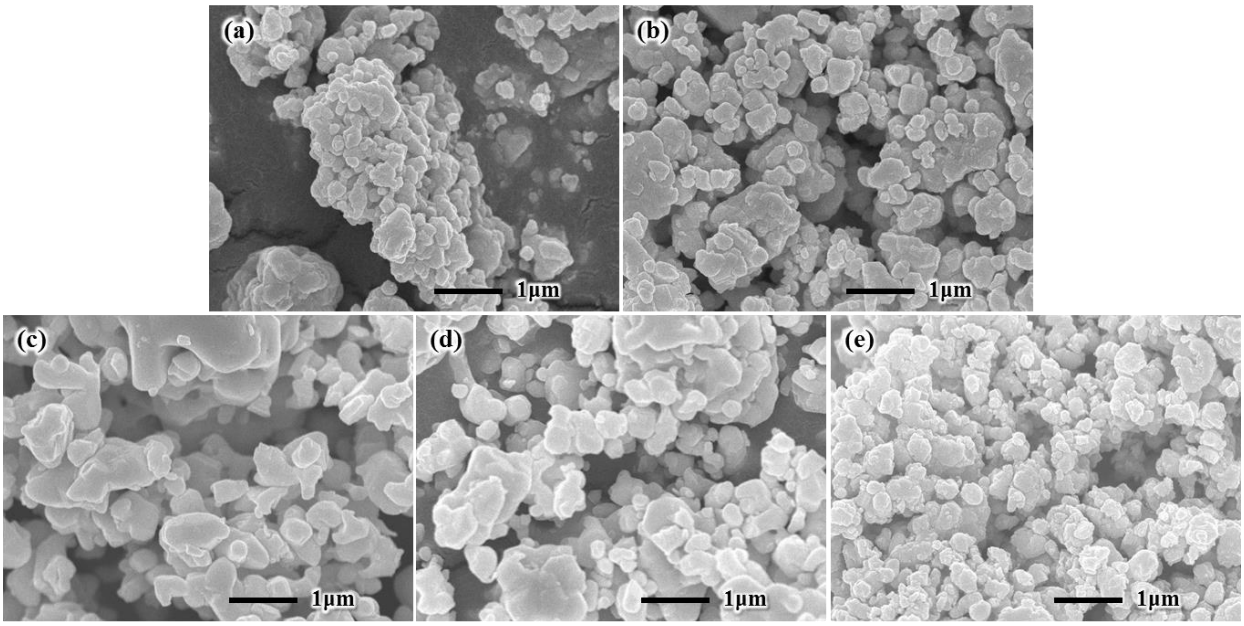

Figure 4.2 SEM images of the synthesized Ln_2NiO_4 oxides: a) La_2NiO_4, b) $LaPrNiO_4$, c) Pr2NiO4, d) $PrNdNiO_4$ and e) Nd_2NiO_4

4.4.2. Electrochemical Characterization

Galvanostatic Full Charge-Discharge Experiments of Ln_2NiO_4 Cathodes: The initial behavior of the catalytic performance of the investigated electrocatalysts can be achieved by fully discharging then charging at constant current densities (50 mA/g_{carbon} in this study). In the discharge phase, the formation of $Li_{2-x}O_2$ species ($0 \leq x < 2$) on the positive electrode of Li-O_2 cell. The discharge current value was fixed throughout the experiment, while the magnitude of the voltage was monitored as a function of specific discharge capacity (capacity = current density × time "mAh/g_{carbon}"). In the recharge phase, the oxidation of these electrochemically formed reaction species was taking place by inverting the reaction direction (externally drive the electron flow from the cathode electrode towards the anode electrode). Figure 4.3 shows the (dis)charge profile at constant current density of 50 mA/g_{carbon}. It is obvious from the figure that all catalyst-containing cathodes have higher discharge capacities and lower charging overpotentials than

carbon only cathodes, hence differentiation in the electrocatalytic activity among the investigated catalysts is shielded by the high surface area of the carbon material (~1200 m^2/g).

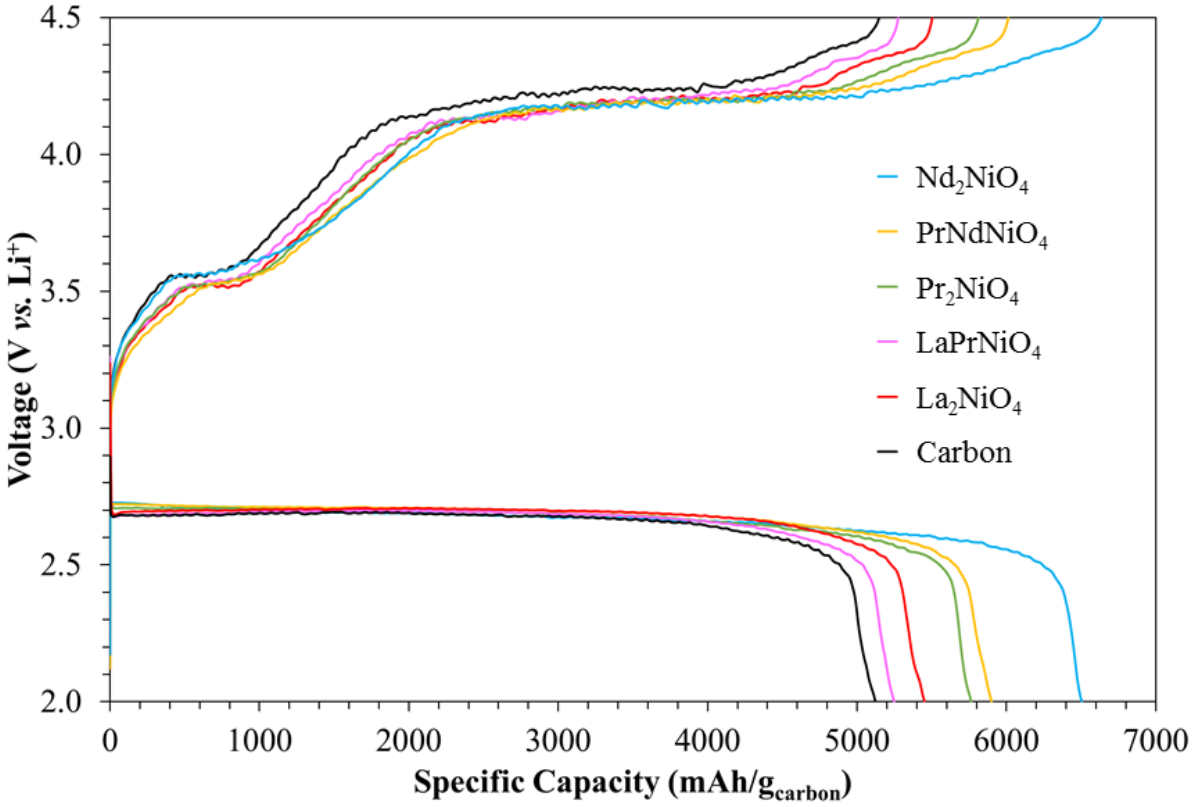

Figure 4.3 Discharge–charge profiles of Li–O_2 batteries composed of carbon-only and 40% electrocatalysts (LNO, LPNO, PNO, PNNO and PNO) supported on carbon cathodes

Cyclic Voltammetry Studies: To further distinguish the effect of A-site composition on the electrocatalytic activity of Ln_2NiO_4 oxides during oxygen reduction and evolution reactions (ORR: $2Li^+ + O_2 + 2e^- \Rightarrow Li_2O_2$, OER: $Li_2O_2 \Rightarrow 2Li^+ + O_2 + 2e^-$) in the Li-$O_2$ cathode, cyclic voltammetry studies were employed. These studies were conducted using a Swagelock design housing of "button" geometry cells consisting of a cathode composed of lanthanum nickelate catalyst and Ketjen Black carbon (or pure carbon in the control experiment), an anode composed of lithium foil, and an electrolyte composed of TEGDME/$LiCF_3SO_3$. These potentiostatic experiments can detect electrocatalytic activity better than current controlled electrochemical experiments, in which

the voltage was controlled by positively scanning the potential at a constant rate (scan rate = 0.1 mV/s) and monitoring the generated current value as a function of time. In comparing different catalysts, the early detected current activity at a particular potential value represents the capability of the investigated cathode material to catalyze the electrochemical reaction efficiently. Figure 4.4 (a) shows the cathodic negative scans of carbon-only and 40 wt% Ln_2NiO_4 supported on carbon.

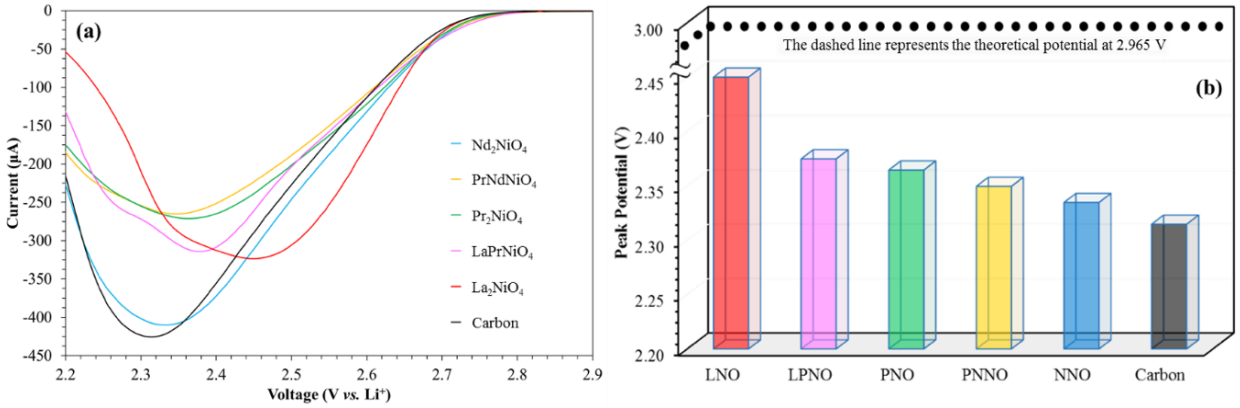

Figure 4.4 (a) CV anodic scans of carbon and Ln_2NiO_4/carbon cathodes using 0.1 mVs^{-1} scan rate. (b) The corresponding peak potentials of the anodic scan as a function of the oxide composition. The dashed line represents the theoretical potential for OER (Li_2O_2 decomposition)

The peak potential for formation of discharge products ($Li_{2-x}O_2$) via the oxygen reduction reaction are depicted in Figure 4.4 (b). The Ln_2NiO_4 oxides exhibit cathodic peaks which are closer to the theoretical potential (shown using a dashed line in Figure 4.4 b) than carbon only cathodes. An increase in the cathodic overpotential (deviation from theoretical potential) was observed as we move from the left to the right of the lanthanide series in the Periodic Table with La_2NiO_4 exhibiting the closest cathodic potential to the theoretical one. These studies suggest an electrocatalytic activity trend toward ORR as follows: La_2NiO_4 > $LaPrNiO_4$ > Pr_2NiO_4 > $PrNdNiO_4$ > Nd_2NiO_4 > carbon.

Cyclic voltammetry anodic scans were used to determine the oxygen evolution potentials required to dissociate the discharge species ($Li_{2-x}O_2$) on different Ln_2NiO_4 oxides. Figure 4.5 shows anodic scans for the nickelate oxides containing different Ln-site compositions. We find

that as in the case of ORR, the La_2NiO_4-containing cathode exhibits the closest OER potential to the OER theoretical potential (shown using a dashed line in Figure 4.5 b). These studies suggest an electrocatalytic activity trend toward OER similar to ORR for the Ln_2NiO_4 oxides: La_2NiO_4 > $LaPrNiO_4$ > Pr_2NiO_4 > $PrNdNiO_4$ > Nd_2NiO_4 > carbon.

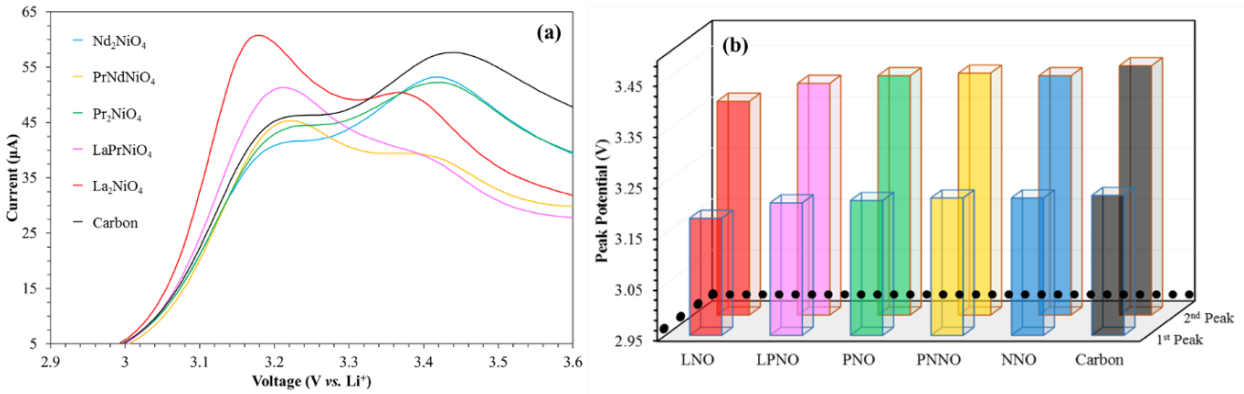

Figure 4.5 (a) CV anodic scans of carbon and Ln_2NiO_4/carbon cathodes using 0.1 mVs^{-1} scan rate. (b) The corresponding peak potentials of the anodic scan as a function of the oxide composition. The dashed line represents the theoretical potential for OER (Li_2O_2 decomposition)

Synthesis of $La_{0.75}A_{0.25}NiO_4$ (A=Ba, Ca, Sr): Lanthanum nickelate oxides doped with 12.5 % of Ca, Sr and Ba were successfully synthesized using the reverse-microemulsion method discussed above. The pure phase crystal structure of these nickelate oxides was obtained as corroborated by the x-ray diffraction spectra shown in Figure 4.6. Figure 4.7 show the SEM images of the as-synthesized oxides. The calcination temperature of these oxides was over 1000°C in order to keep it consistent with the Ln_2NiO_4 oxides discussed above. While $Ca_{0.25}La_{1.75}NiO_4$ and $Sr_{0.25}La_{1.75}NiO_4$ were similar to the Ln_2NiO_4, $Ba_{0.25}La_{1.75}NiO_4$ resulted in slightly larger particles.

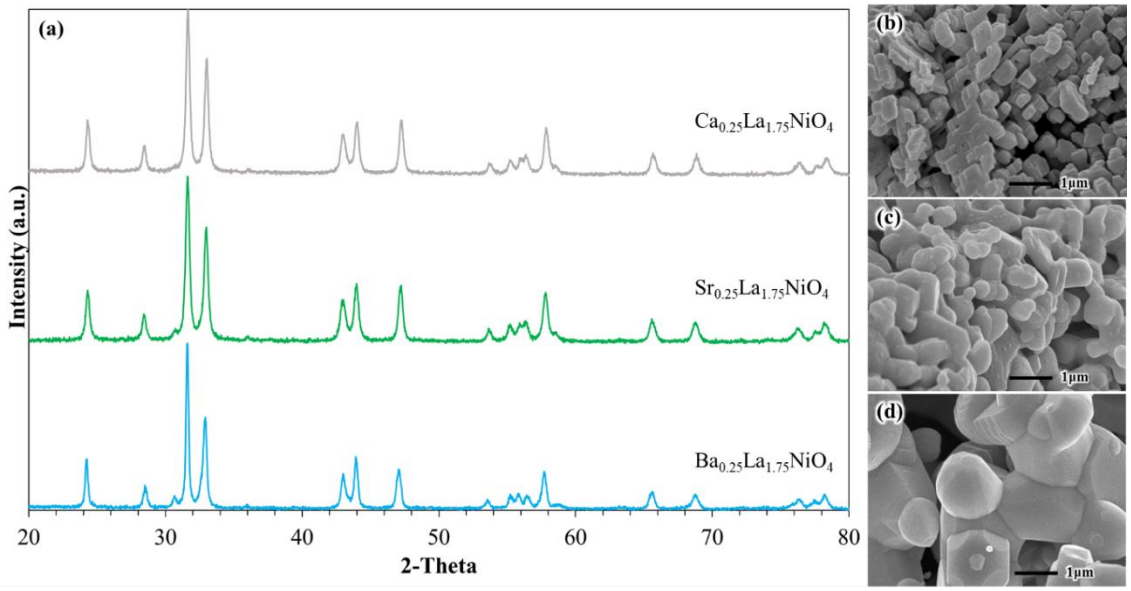

Figure 4.6 (a) X-ray diffraction patterns of the synthesized $Ca_{0.25}La_{1.75}NiO_4$, $Sr_{0.25}La_{1.75}NiO_4$ and $Ba_{0.25}La_{1.75}NiO_4$. SEM images of the synthesized (b) $Ca_{0.25}La_{1.75}NiO_4$, (c) $Sr_{0.25}La_{1.75}NiO_4$ and (d) $Ba_{0.25}La_{1.75}NiO_4$.

Full Charge/Discharge electrochemical performance of $A_{0.25}La_{0.75}NiO_4$ (A=Ba, Sr, Sr): To investigate the performance of $La_{0.75}A_{0.25}NiO_4$ (A=Ba, Sr, Sr) in catalyzing the oxygen reduction and evolution reactions in the Li-O_2 cathode galvanostatic full charge/discharge experiments were conducted. Figure 4.8 shows the cell voltage versus specific capacity behavior during galvanostatic full charge/discharge experiments for cells containing carbon-only cathodes and carbon cathodes with 40 wt% loading of $Ba_{0.25}La_{1.75}NiO_4$, $Ca_{0.25}La_{1.75}NiO_4$ and $Sr_{0.25}La_{1.75}NiO_4$ oxides. In these experiments, the battery cells were allowed to discharge with a cutoff voltage of 2 V and charge with a cutoff voltage of 4.5 V at a rate (current density) of 100 mA/g_{carbon}. For cells containing carbon-only cathodes (Figure 4.8 a, black line), the first full discharge specific capacity was around 4,700 mAh/g_{carbon}, consistent with previous literature reports.[203] On the other hand, for the battery cells with carbon cathodes containing 40 wt% loading of $Ba_{0.25}La_{1.75}NiO_4$, $Ca_{0.25}La_{1.75}NiO_4$ and $Sr_{0.25}La_{1.75}NiO_4$ oxides, the first full discharge capacities were approximately 6278 mAh/g_{carbon}, 5465 mAh/g_{carbon} and 5810 mAh/g_{carbon}, respectively. We find that the incorporation of nickelate oxides led to an increase in the discharge capacity of the battery cell as compared to the one

containing carbon-only cathode. The highest discharge capacity was obtained for the $Ba_{0.25}La_{1.75}NiO_4$-containing cathode cell. Moreover, we find that $Ba_{0.25}La_{1.75}NiO_4$ oxide-containing cells also exhibited the lowest charging potentials as compared to the other cells. These results suggest that in addition to enhancing the storage of Li_2O_2, $Ba_{0.25}La_{1.75}NiO_4$ oxide also lowers the charging overpotential losses during the oxygen evolution reaction. This could be due to the fact that doping the La-site with Ba affects the oxygen chemistry on the surface favoring the dissociation of $Li_{2-x}O_2$, as in the case of high temperature electrochemical systems. One further observation from these experiments is that the initial discharge voltage of $Ba_{0.25}La_{1.75}NiO_4$ occur at lower overpotentials compared to the other cathodes, this might be attributed to the favorable formation of lithium-deficient oxide species (i.e. LiO_2) that can dissociate at lower overpotentials.[25] Further studies are necessary to determine the exact mechanism that governs the superior performance of $Ba_{0.25}La_{1.75}NiO_4$ oxide. We would like to note that characterization of the cathodes before and after the galvanostatic full charge/discharge experiments using X-ray diffraction show that no morphological changes occurred to the nickelate oxide electrocatalysts used in these studies (See Figure 4.7 b).

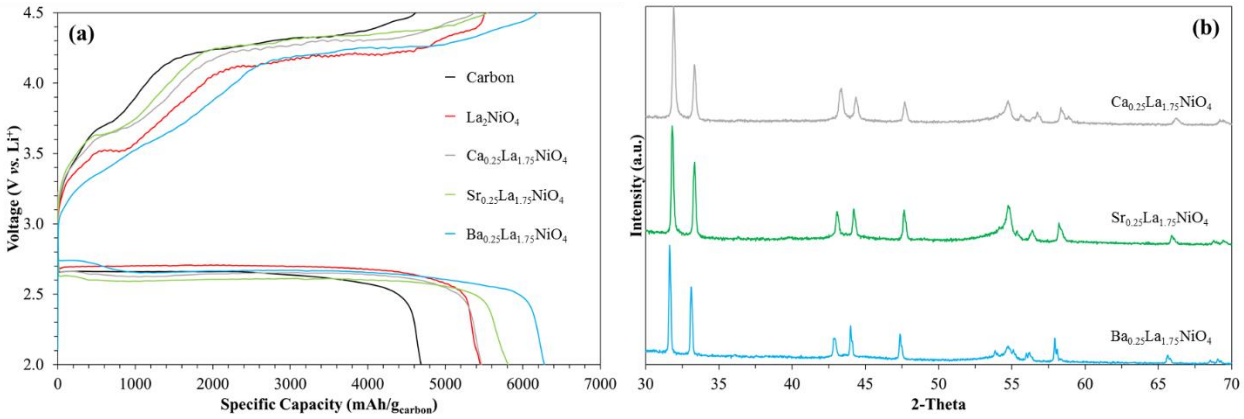

Figure 4.7 Full discharge/charge performance using 40% catalyst loading on Ketjen Black carbon cathodes with a carbon loading on each cathode of 0.985 mg_{carbon}/cathode. The constant current density used was 50 mA/g_{carbon} with discharge and charge cutoff voltages of 2 and 4.5 volts, respectively. (b) X-ray diffraction patterns after full charge/discharge studies of the cathodes containing $Ca_{0.25}La_{1.75}NiO_4$, $Sr_{0.25}La_{1.75}NiO_4$ and $Ba_{0.25}La_{1.75}NiO_4$

4.5. Conclusions

We have demonstrated that the composition of the A-site in first-order Ruddlesden-Popper series of layered oxides (A_2BO_4) has an effect on the electrochemical activity of Li-O_2 cathodes. Among the lanthanides that form stable Ruddlesden-Popper oxide structures, La_2NiO_4 exhibits the best electrochemical performance when incorporated in Li-O_2 cathodes. The electrochemical performance of the La_2NiO_4 electrocatalyst could be further improved by doping the A-site with alkaline earth metals, such as Ba. We show that $Ba_{0.25}La_{1.75}NiO_4$ exhibits the best discharge capacity and lowest OER potential when compared to undoped La_2NiO_4, $Sr_{0.25}La_{1.75}NiO_4$ and $Ca_{0.25}La_{1.75}NiO_4$. The reason for this could be due to the fact that doping the La site with Ba leads to an O surface chemistry that facilitates the oxygen evolution reaction with the lowest oxygen barrier. The low overpotential loss of $Ba_{0.25}La_{1.75}NiO_4$ during recharge might be influenced by the early high discharge voltage, which in turn could be explained by the formation of electrochemical reaction intermediate species (i.e. LiO_2) during discharge that is stabilized at the catalyst surface. The dissociation of these lithium-deficient materials are favorably decomposing (during recharge phase) at lower voltages than Li_2O_2 or Li_2O. These findings set the race in the discovery of more active electrocatalysts that can stabilize the formation of transient reaction products at room temperate and ambient conditions.

CHAPTER 5. NANOSTRUCTURED LA_2NIO_4 AS EFFICIENT AND STABLE CATHODE ELECTROCATALYST FOR LI-O_2 BATTERY

5.1. Summary

In this chapter, we demonstrate the ability to utilize a well-controlled microemulsion method to synthesize La_2NiO_4 (LNO) nanostructures with rod-shaped morphology as active and stable cathode electrocatalysts for non-aqueous Li-O_2 batteries. The presented electrochemical studies show that the incorporation of nanorod LNO catalyst in Li-O_2 cathodes resulted in lowering of the charging potential, and enhancement of the reversible specific discharge/charge capacities as compared to carbon-only cathodes.

5.2. Introduction

As mentioned in the previous chapter, La_2NiO_4 (LNO) exhibited the lowest overpotential losses during oxygen reduction and evolution reactions among all tested Ln_2NiO_4 electrocatalysts. In this chapter we have expanded on the previous chemical composition studies by exploring the electrocatalytic behavior of LNO with different morphologies on both ORR and OER in Li-O_2 battery. We show that LNO displayed higher catalytic activity during ORR when they are formed in the nanorod shape by an increase in the discharge specific capacity and the smaller size formation of the reaction product (Li_2O_2). While slow anodic scan voltammetry studies demonstrated the key activity of LNO nanorods in lowering the activation barriers during OER when commercial Li_2O_2 was preloaded on the cathodes.

It has been shown in the literature that the morphology and microstructure of catalytically active ORR materials are of a great importance.[238-242] Jia *et. al.*[242] have demonstrated that α-MnO_2 nanofibers exhibited the best catalytic activity on the decomposition of gaseous ozone among the other tested structures (nanotubes and nanorods). The author has attributed the increase in catalytic

activity to the amount of oxygen vacancies, where α-MnO_2 nanofibers showed to have the most abundant oxygen vacancies due to the exposed (211) facet. Lu *et. al.*[243] investigated the electrocatalytic activity of hollow spherical $La_{0.8}Sr_{0.2}MnO_3$ (HS-LSM) perovskite oxide on ORR in alkaline medium. They have observed that HS-LSM was able to reduce oxygen at lower overpotentials than synthesized urchin-like LSM and commercial LSM. The catalyst also showed higher current density values compared to other LSMs and remarkable stability and durability when compared to commercial Pt/C electrocatalysts.

5.3. Experimental Details

5.3.1. Catalyst Synthesis

The nanorod LNO was prepared using a reverse-microemulsion method.[244] As explained in Chapter 3, two separate reverse-microemulsions were first prepared, with each containing a quaternary reverse-microemulsion system composed of cetyltrimethylammonium bromide (CTAB)/water/hexane/n-Butanol. One microemulsion was formed by mixing 1.734 g of $La(NO_3)_3$•$6H_2O$ (99.999%, Sigma-Aldrich) and 0.594 g of $Ni(NO_3)_2$•H_2O (98%, Alpha Aesar) in 7.0 g of deionized water, and the other one was formed by mixing 0.825 g of NaOH (ACS grade, Fisher) and 7.0 g of deionized water. In each microemulsion system, the amount of CTAB, hexane, and n-butanol was fixed at 11.25 g, 56 mL and 11.25 ml, respectively. After the solutions were well mixed, the microemulsion system containing the base was added to the system containing the metal salts under stirring (1200 rpm). The mixture was maintained under the same conditions for 4 hours to form the gel suspension containing the precipitated metal hydroxide. The solid gel was collected by centrifugation (6000 rpm, 3 min). This was followed by washing twice using ethanol, and three times using deionized water. The solid gel was then dried under air at 80 °C for 12 hours. The obtained solid was transferred to a quartz tube and calcined at 825 °C (2 °C/min ramp rate

from room temperature) for 2 hours under flowing argon (350 sccm). For the LNO polyhedron nanostructure synthesis, the amount of water added to the metal nitrate was decreased to adjust the ratio between CTAB and H_2O to 14.

5.3.2. Cathode Fabrication

Initially, the prepared LNO electrocatalysts were sonicated in ethanol (0.1 g catalyst in 3 ml ethanol) for one hour. The solution with the dispersed electrocatalyst was then impregnated (with the desired loading) onto the mesoporous carbon powder (Ketjen Black EC600JD, Akzo Nobel). This was followed by aging at 75 °C and 110 °C for 20 minutes and 2 hours, respectively. The weight loading of the catalyst on carbon was verified later by TGA.

In a typical procedure for the preparation of the Li-O_2 cathode, 0.1 g of polyvinylidene fluoride (PVDF, Sigma-Aldrich) binder was first dissolved in 8 ml of N-methyl-2-pyrrolidone (NMP, 99.5%, Sigma-Aldrich) and stirred overnight. This was followed by the addition of the appropriate amount of the catalyst-carbon mixture (based on the LNO loading) and stirring for an additional 24 hours. The slurry was then sprayed using an airbrush on one side of the carbon paper (Toray TGP-H-030, FuelCell Store) to yield a final carbon loading of 0.77 ± 0.01 mg_{carbon}/cm^2 (0.985 mg_{carbon}/cathode) for all the cells reported in this work. This was followed by drying at 115°C for 3 hours.

The cathodes for slow anodic sweep voltammetry experiments were fabricated in a glove box (MBraun Unilab, oxygen and moisture levels < 0.1 ppm). 0.257 g of lithium peroxide (Li_2O_2, 90%, Sigma-Aldrich) was added to 3.2 g of NMP and sonicated for 10 minutes. This was followed by the addition of 1.2 g of the catalyst-carbon mixture (or 1 g of pure carbon powder in the control experiment). After 5 hours of rigorous stirring, the slurry was sprayed onto the carbon paper. The obtained cathodes were then dried at 120 °C for 30 minutes followed by further drying under

vacuum overnight. These cathodes (sealed in an air tight vessel) were characterized using XRD to verify the presence of Li_2O_2 and galvanostatic charge only experiments to evaluate the loading of Li_2O_2 on the cathode matrix.

5.3.3. Battery Assembly

The electrolyte solution was prepared by dissolving lithium trifluoromethanesulfonate ($LiCF_3SO_3$, 99.995%, Sigma-Aldrich, dried at 130 °C under vacuum for 12 hours before use) in anhydrous tetraethylene glycol dimethyl ether (TEGDME, Sigma-Aldrich, dried using 3Å molecular sieves) using a 1:4 molar ratio, respectively. Lithium foil (0.75 mm thick, 99.9%, Sigma-Aldrich) was cut into ⅜" disk, polished, and supported on a stainless steel shim current collector. This was followed by placing a glass microfiber (Whatman®) separator on top and the addition of 100 μL of the electrolyte solution. The catalyst-containing side of the carbon paper was then placed on top of the separator followed by a nickel mesh current collector (in a shape of a porous flat disk, Goodfellow USA). The cells were then sealed and their open circuit voltage was measured. All the above steps were conducted in an argon filled glove box with both oxygen and moisture levels less than 0.1 ppm.

5.3.4. Characterization

The determination of LNO loading in catalyst-carbon mixture in each cathode was performed by thermal gravimetric analysis (TGA, Q600, TA Instruments). The X-ray diffraction (XRD) characterization of each sample was performed with a powder X-ray diffractometer (Smartlab, Rigaku Inc., Japan) using Cu Kα radiation (λ = 0.15418 nm). XRD pattern of fresh LNO was recorded over 2θ values of 20º to 80º at a rate of 2º / min. For XRD data collection of the discharged/charged cathodes, the electrodes were sealed in argon protected vessels inside the

glove box, transferred to the XRD sample holder, and scanned over 2θ values of 30º to 70º at a rate of 1º / min.

The morphology of each sample was analyzed using a field-emission scanning electron microscopy (SEM, JSM-7600, JEOL Inc., Japan) at the accelerating voltage of 15 kV. The bright field transmission electron microscopy (TEM) characterization was performed using a JEOL 3011 electron microscope (JEOL Inc., Japan) at an accelerating voltage of 300 kV. Dark field TEM and electron energy loss spectroscopy (EELS) were carried out using a JEOL 2010 electron microscope (JEOL Inc., Japan) at an accelerating voltage of 200 kV. The EELS data were acquired under scanning transmission electron microscope (STEM) mode with a beam converge angle of 12 mrad and data collection angle of 38 mrad. The energy resolution of EELS was measured from the full width at the half maximum (FWHM) of the zero-loss peak (ZLP).

5.3.5. Electrochemical Testing

Galvanostatic Discharge-Charge: The assembled cells were connected to a flow of ultra-high purity oxygen (99.999%) for 30 minutes before testing. All the testing experiments were conducted using a battery analyzer (MTI corp. Richmond, CA) under a current density of 100 mA/gcarbon (0.077 mA/cm^2). The reported specific capacities were normalized based on the carbon weight of each cathode, consistent with literature reports.[43,53,121] After each test, the battery cells were disassembled inside the glove box for further characterization.

Charge Verification of Preloaded Li_2O_2: Quantification of the lithium peroxide preloaded on carbon cathode was performed by charging the cells under the flow of argon at 70 mA/g_{carbon}. The expected charge specific capacity of the charged cathodes should match the ratio of Li_2O_2 to carbon used to prepare these electrodes. The expected specific capacity was calculated as follows:

Expected Specific Capacity

$$= \mathbf{1500}\,\frac{\mathbf{mAh}}{\mathbf{g_{carbon}}} \times \frac{1\text{ A}}{1000\text{ mA}} \times \frac{3600\text{ s}}{1\text{ h}} \times \frac{1\ {}^{\text{Coulomb}}/_{\text{S}}}{1\text{ A}} \times \frac{6.24150965 \times 10^{18}\text{ e}^-}{1\text{ Coulomb}} \times \frac{1\text{ mol of e}^-}{6.022141 \times 10^{23}\text{e}^-}$$

$$\times \frac{1\text{ mol of } Li_2O_2}{2\text{ mol of e}^-} \times \frac{45.88\text{ g}_{Li_2O_2}}{1\text{ mol of } Li_2O_2} = \mathbf{1.284}\ \frac{\mathbf{g_{Li_2O_2}}}{\mathbf{g_{carbon}}}$$

Slow Anodic Sweep Voltammetry: Slow anodic sweep voltammetry experiments were conducted using Gamry 3000 potentiostat (Gamry Instruments, USA) on battery cells containing pre-loaded Li_2O_2 particles of a given particle size and shape at the cathode. In these experiments, the current generated was measured as the charging potential was slowly swept from 3 to 4.5 V using a scanning rate of 0.02 mV/s. The observed current was normalized to the weight of lithium peroxide deposited on each cathode. Background scans (cathodes without Li_2O_2) were also collected and subtracted from the voltammograms of the reported measurements.

Electrochemical Cycling: In order to test the long-term stability of the battery cells with LNO electrocatalyst, we have conducted multiple charge/discharge cycling experiments. The same setup as the one used for the galvanostatic full charge-discharge experiments was used to run these tests. These experiments were conducted using a current density of 100 mA/g_{carbon} and a specific capacity of 500 mAh/g_{carbon}.

5.4. Results and Discussions

5.4.1. Controlling the Catalyst Morphology

Nickelate oxides, as discussed above, are layered oxide structures containing alternating rocksalt-like and perovskite-like layers as illustrated in Figure 5.1 (a). While these oxides have been used in solid oxide electrochemical cells[236,237] and Li-air cathodes,[123,231] little is known about the factors that govern their catalytic/electrocatalytic activity. Theoretical reports have suggested that oxygen non-stoichiometry and high-energy surface facets, such as (001), can impact the catalytic/electrocatalytic activity of these materials toward reactions involving oxygen.[245]

Unfortunately, current state-of-the-art synthesis approaches employed to synthesize these materials do not allow for control over the morphology and surface structure of nickelate oxides.[246,247] We have successfully utilized a reverse-microemulsion approach to synthesize nanostructured LNO electrocatalyst with preferential morphology and control over the distribution of highly energetic surface facets.[244] As illustrated in Figure 5.1 (b), the synthesis involves (i) the co-precipitation of metal ions inside the gel formed through intermicellar exchange of two separate reverse-microemulsions containing metal cations and hydroxide anion, (ii) separation of the metal hydroxide gel from reaction mixture, and (iii) transformation of the hydroxide to nickelate oxides crystals. Figure 5.2 (a) shows the XRD patterns of the LNO electrocatalysts obtained in our synthesis, which is consistent with those of LNO with K_2NiF_4 structure (JCPDS No. 34-0314, *I4/mmm* space group). The scanning electron micrographs of both LNO-nr and LNO-ns obtained in our synthesis.

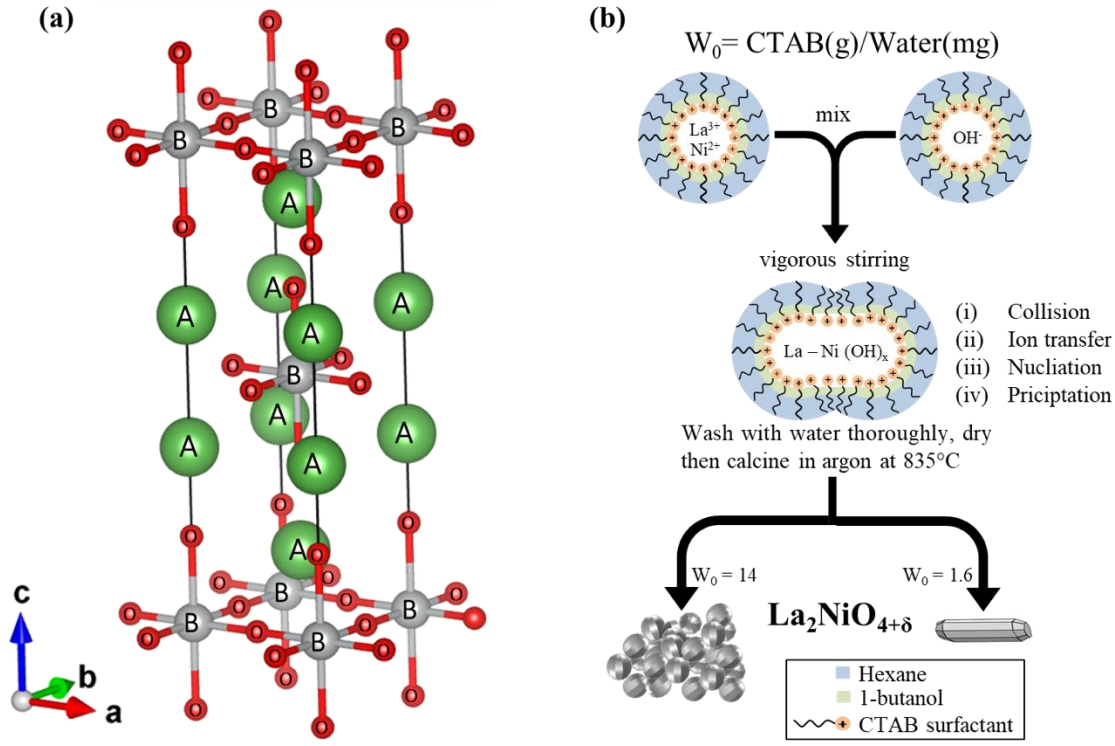

Figure 5.1 (a) Crystal structure of stoichiometric A_2BO_4 showing the perovskite-like and rocksalt-like layers. (b) Schematic illustration of the synthesis of LNO nanorods and nanospheres

The bright-field (BF) and high-resolution (HR) TEM images of an individual LNO nanorod are shown in Figure 5.3 (a) and Figure 5.3 (b), respectively. The continuous lattice fringe in the HRTEM image and the indices of the spots in the corresponding fast Fourier transform (FFT) pattern (inset, Figure 5.3 (b)) indicate the distribution of well-coordinated (001) facet on the sides of the LNO nanorod.

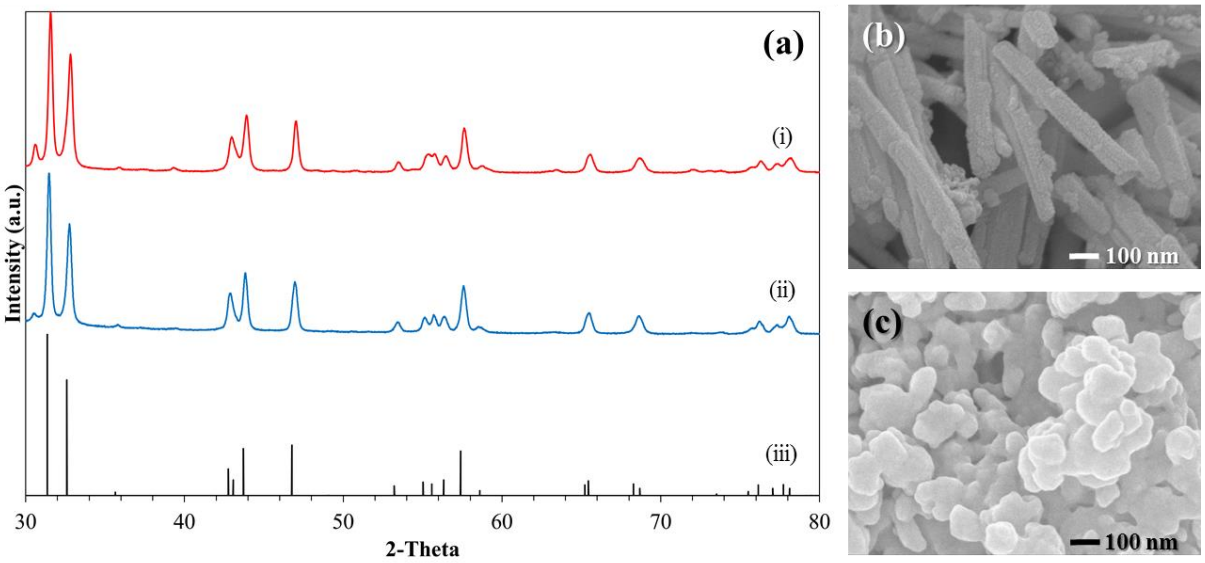

Figure 5.2 (a) XRD patterns of (i) LNO nanorods, (ii) LNO nanospheres and (iii) the standard data for $La_2NiO_{4+\delta}$ (JCPDS No. 34-0314). SEM images of (b) LNO nanorods and (c) LNO nanospheres

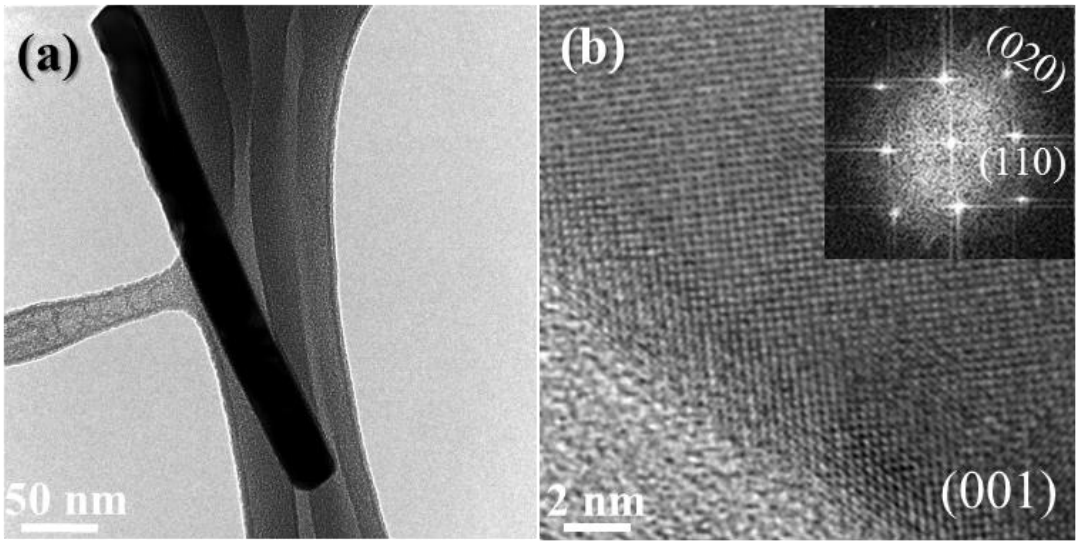

Figure 5.3 (a) Bright-field (BF) TEM image of an individual LNO nanorod. (b) High-resolution (HR) TEM image of the edge of an individual LNO nanorod. The inset in image (b) shows the corresponding fast Fourier transform (FFT) pattern of the image

5.4.2. Galvanostatic Discharge-Charge

To investigate the performance of LNO nanorods and nanospheres in catalyzing the oxygen reduction and evolution reactions (ORR: $2Li^+ + O_2 + 2e^- \Rightarrow Li_2O_2$, OER: $Li_2O_2 \Rightarrow 2Li^+ + O_2 + 2e^-$) in Li-$O_2$ cathode, a modified Swagelok design[203] of the cells was employed. The "button" geometries of the battery cells in this study consisted of a cathode composed of LNO catalyst and Ketjen Black carbon (or pure carbon in the control experiment), an anode composed of lithium foil, and an electrolyte composed of TEGDME/$LiCF_3SO_3$ (See the Experimental Section for details). The loading of LNO catalysts on the carbon electrode was verified using TGA as shown in Figure 5.4.

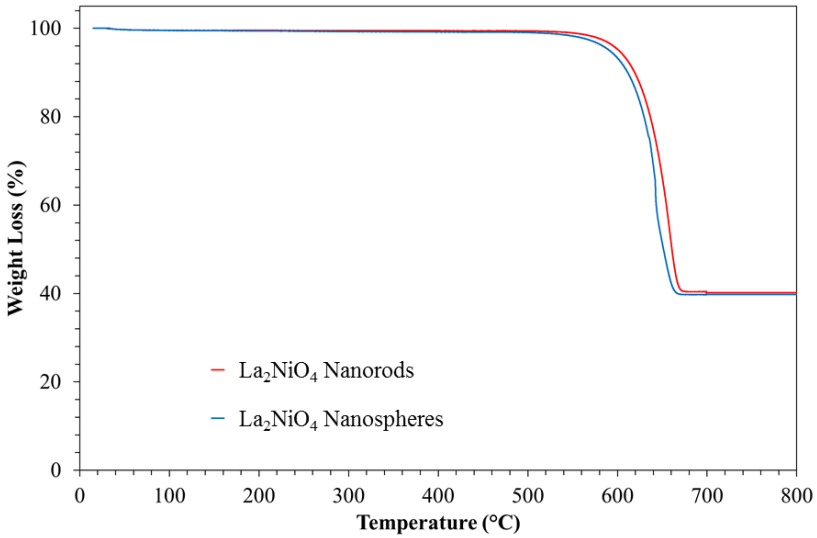

Figure 5.4 TGA curves of impregnated LNO nanorods and nanospheres on Ketjen Black carbon powder

The controlled current discharge-charge profiles of cathodes containing nr-LNO and ns-LNO are shown in Figure 5.5. In these experiments, the battery cells were allowed to discharge with a cutoff voltage of 2.0 V and charge with a cutoff voltage of 4.5 V at a rate (current density) of 100 mA/g_{carbon}. LNO with nanrods morphology show higher discharge capacities and lower charging overpotential compared to LNO nanospheres. Accordingly, we have further investigated various LNO nanorods loadings on carbon cathodes.

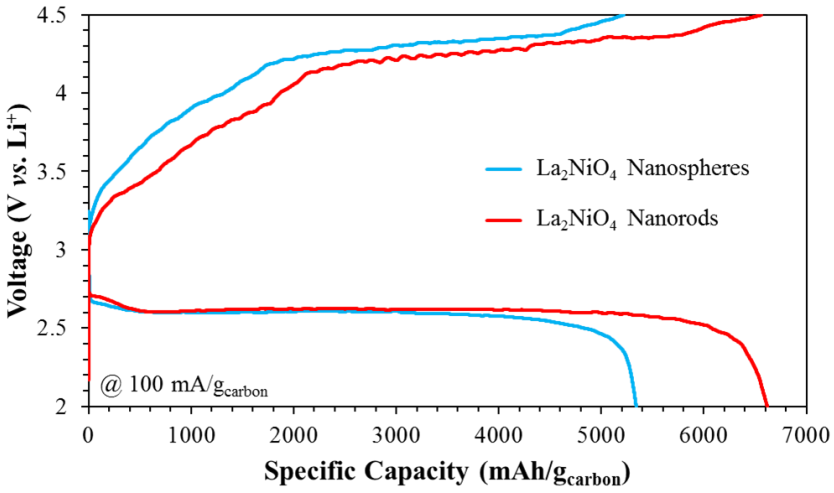

Figure 5.5 Discharge–charge profiles of Li–O_2 batteries composed of 40% LNO-nr (red) and 40% LNO-ns (blue)

Figure 5.6 shows the cell voltage versus specific capacity behavior during galvanostatic full charge/discharge experiments for cells containing carbon-only cathodes, carbon cathodes with 40 wt% ns-LNO and 40 wt% nr-LNO. While Figure 5.6 (a) shows the (dis)charge behavior of nr-LNO with different loadings of 20 wt%, 40 wt% and 60 wt%. For cells containing carbon-only cathodes (Figure 5.6, black line), the first full discharge specific capacity was around 4,700 mAh/g_{carbon}, consistent with previous literature reports.[203] On the other hand, for the battery cells with carbon cathodes containing 20 wt%, 40 wt% and 60 wt% loading of LNO, the first full discharge capacities (Figure 3, red, blue and green lines, respectively) were approximately 5182 ± 97 mAh/g_{carbon}, 6618 ± 128 mAh/g_{carbon} and 7280 ± 135 mAh/g_{carbon}. In all the cases, the incorporation of LNO nanorods led to an increase in the discharge capacity of the battery cell as compared to the carbon-only cathode cells. These results suggest that the presence of the nr-LNO electrocatalyst improved the storage/formation of the discharge product (Li_2O_2). Moreover, the charging potentials of the battery cells with carbon cathodes containing nr-LNO electrocatalyst were lower than the ones obtained for the battery cells containing carbon-only cathodes as shown by the charging profiles plotted in Figure 5.6 b. These results suggest that in addition to enhancing

the storage of Li_2O_2, LNO also lowers the charging overpotential losses during the oxygen evolution reaction. The role of LNO on influencing the charging potential can be a consequence of two factors[121]: (i) the change in the nature of Li_2O_2 formed on the carbon cathodes containing LNO nanorods as compared to the carbon-only cathodes, and (ii) the ability of LNO nanorods to catalyze OER with a lower energy barrier than carbon. In the next few sections we analyze and discuss the impact of each of these factors on the charging performance of the battery cells composed of carbon cathodes containing nr-LNO electrocatalyst. We would like to note that the characterization studies of the cathodes before and after the galvanostatic full charge/discharge experiments using X-ray diffraction suggested that no morphological changes occurred to the carbon-only cathodes (see Figure 5.7 a) and the nr-LNO containing cathodes (See Figure 5.7 b) during these experiments. In addition, the XRD studies confirmed the formation of Li_2O_2 as the main discharge product during the first full discharge on both cathodes, and its complete removal during charging (Figure 5.7 a ii, iii for carbon-only cathode, and Figure 5.7 b ii, iii for LNO/carbon cathode).

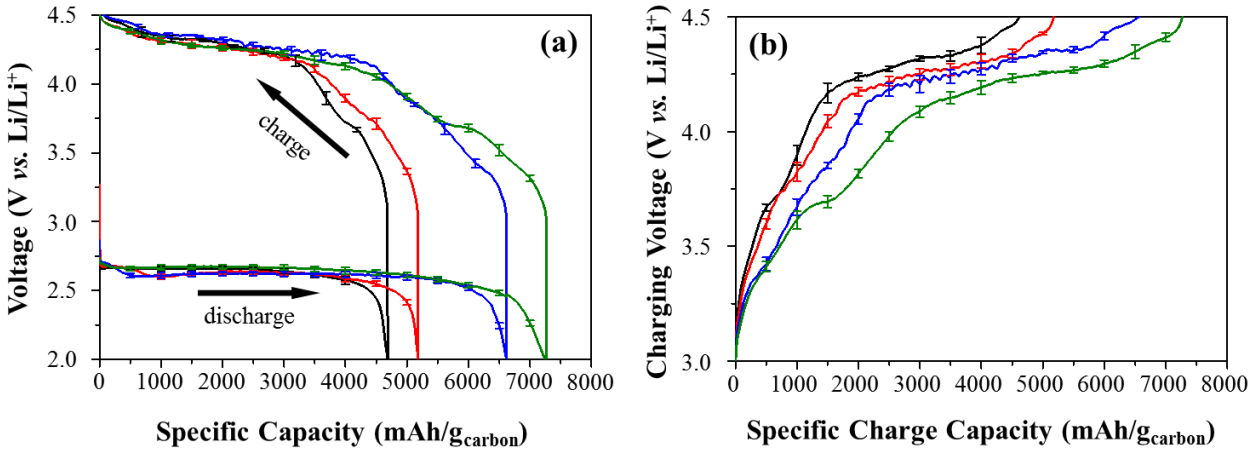

Figure 5.6 (a) Discharge–charge profiles of Li–O_2 batteries composed of carbon-only cathodes (black line), and carbon cathodes with 20 wt% (red line), 40 wt% (blue line) and 60 wt% (green line) nanorod LNO electrocatalyst. Error bars were generated for three replicas of each experiment. (b) Charging profiles (specific charge capacity vs. charging voltage) of the same battery cells

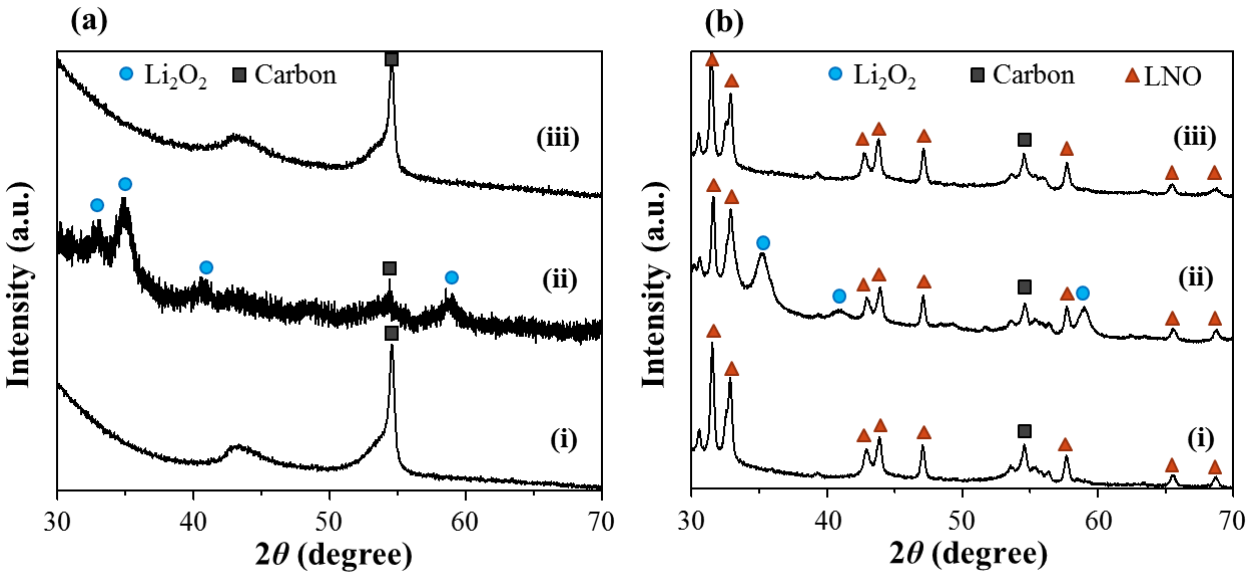

Figure 5.7 (a) XRD patterns of carbon-only cathodes (i) as-prepared, (ii) after first discharge, and (iii) after first charge. (b) XRD patterns of LNO-nr/carbon cathodes (i) as-prepared, (ii) after first discharge, and (iii) after first charge. The results for the LNO/carbon cathodes were similar for all the different LNO-nr loadings

5.4.3. Impact of LNO on Li_2O_2 Formation

In order to evaluate the impact of LNO electrocatalyst on the formation of Li_2O_2 during discharge, the battery cells composed of carbon cathodes with and without LNO were characterized after the first discharge measurement using XRD, TEM and EELS. The X-ray diffraction studies of the cathodes with and without nr-LNO after the first full discharge (Fig. 5.6 a-ii and b-ii) showed the formation of Li_2O_2 as the only discharge product on both cathodes. XRD also showed that the crystallite size of Li_2O_2 formed on LNO-containing cathodes (approximately 21 nm, estimated by Scherrer analysis) was smaller than that of Li_2O_2 formed on the carbon-only cathodes (approximately 25 nm). Dark-field TEM (DF-TEM) studies along with EELS analysis of the carbon-only cathode (without catalyst) after discharge (Figure 5.8, inset) showed the formation of bulky Li_2O_2 particles or aggregates with diameters larger than 1 μm. We also observed that the Li_2O_2 particles were very unstable under the electron beam (see the black holes due to beam damage in the TEM image in Figure 5.8 a). The TEM image in Figure 5.8 b shows the Li_2O_2

particles formed on the surface of LNO nanorods in the LNO containing cathode. The Li_2O_2 particles in this case appear to be smaller and more dispersed on the LNO nanorods as compared to the ones formed on the carbon cathodes. These results suggest that LNO nanorods might affect the formation of Li_2O_2 by facilitating the generation of nanosized Li_2O_2 particles dispersed on the catalyst surface that possibly require lower charging potentials to dissociate.

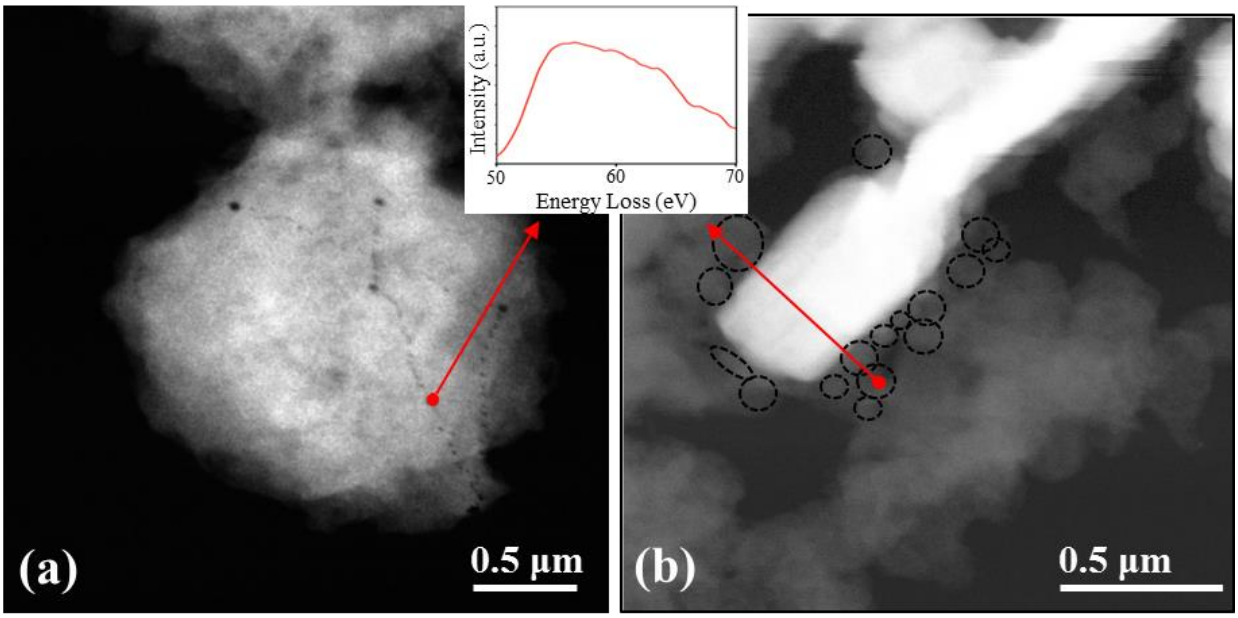

Figure 5.8 (a) Darkfield TEM of the Li_2O_2 particles formed on carbon-only cathode after first discharge. The inset between image a and b shows the EELS spectra of Li k-edge of the particles on both cathodes. (b) Dark-field TEM of Li_2O_2 particles formed on LNO containing cathode after first discharge. Dashed circles are used for visual enhancement of the Li_2O_2 particles on the surface of LNO nanorods

5.4.4. Impact of LNO Nanorods on the Oxygen Evolution Kinetics

Potentiostatic ‘‘charge-only’’ experiments (also known as slow anodic potential sweep voltammetry) were utilized to isolate the electrocatalytic OER activity of carbon cathodes with and without nanorod-shaped LNO electrocatalyst. These experiments were conducted using cathodes pre-loaded with Li_2O_2 particles of controlled size and morphology (see Figure 5.10) in order to eliminate any activity artifacts induced by the morphological/compositional differences of the Li_2O_2 formed during discharge on battery cells containing carbon cathodes with and without

the electrocatalysts.[121,248] The loading of Li_2O_2 on the cathode was verified by galvanostaticly charging the cathode at a constant current of 100 mA/g_{carbon} (see inset Figure 5.9 a), the detected specific capacity matches the amount of Li_2O_2 as calculated by equation 1.

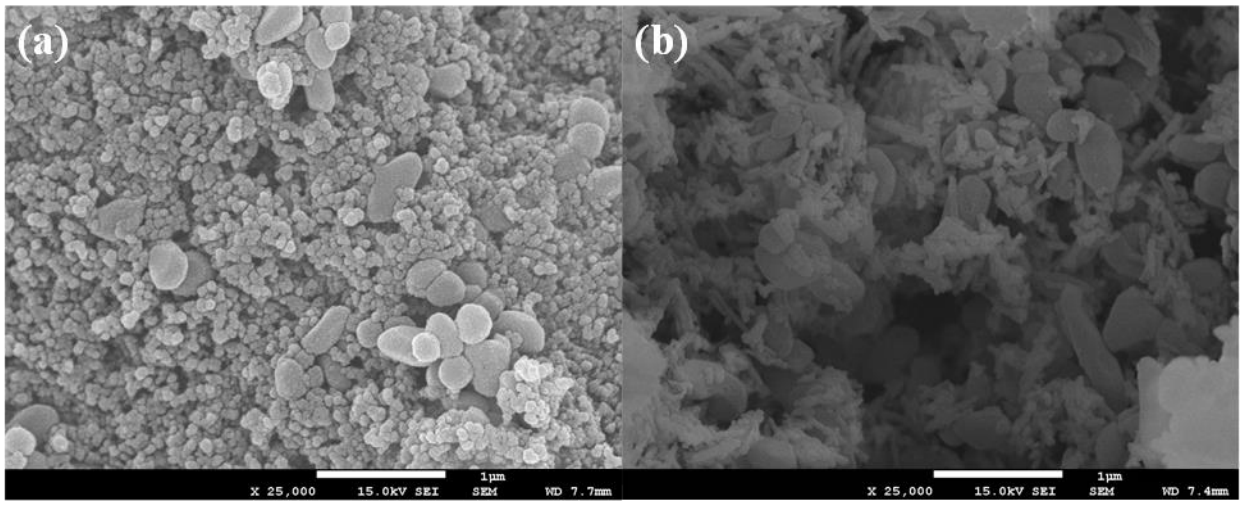

Figure 5.9 SEM images of Li_2O_2 containing (a) carbon and (b) nr-LNO containing cathodes

All the cathodes used in these studies contained no binder to avoid any chemical reaction between the binder (PVDF) and Li_2O_2 particles as shown in previous reports.[249] Figure 5.10a shows the current density versus potential voltammograms from the slow anodic potential sweep experiments. In the case of the cells with carbon-only cathode, the current density (rate) peaks at 4.3 V (*vs.* Li/Li^+), while for the cells containing LNO nanorods current density peaks at 3.9 V (*vs.* Li/Li^+). This suggests that the dissociation of Li_2O_2 via OER on the battery cell with cathode containing LNO occurs at lower potential than on the battery cell with carbon-only cathode, indicating the enhancement of OER activity of the cathode by the presence of LNO (the catalyst activates OER at a potential of 0.4 V lower than carbon). Characterization of the cathodes with and without LNO nanorods confirmed (i) the dissociation of the loaded Li_2O_2 during these experiments on both cathodes (Figure 5.10 b), and (ii) the stability of the LNO crystal structure (Figure 5.10 b-iii, iv).

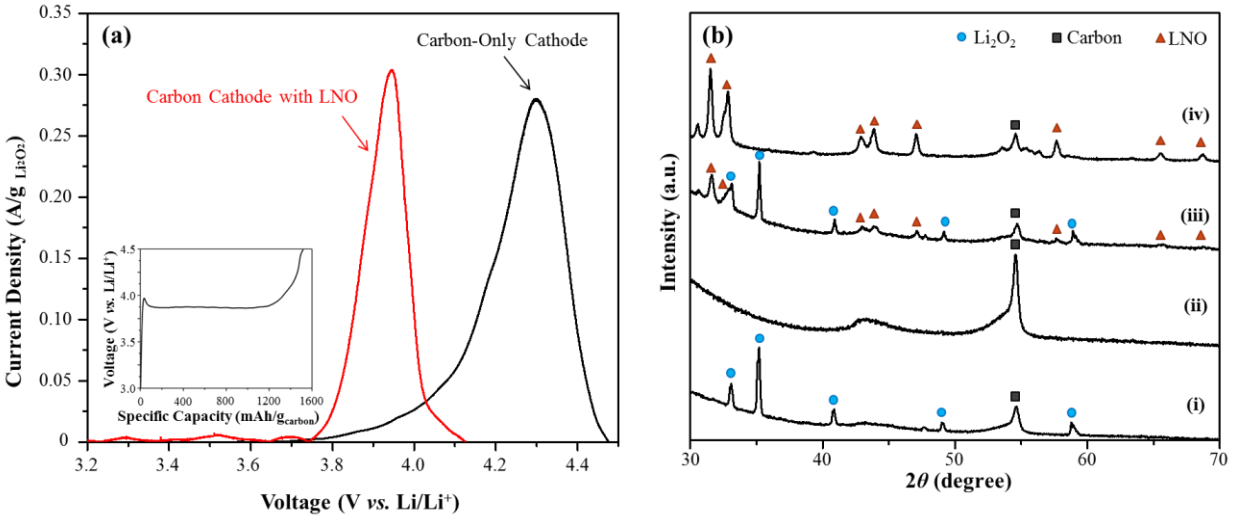

Figure 5.10 (a) Slow anodic sweep voltammograms (SASV) of carbon-only cathode with preloaded Li_2O_2 (black curve) and nr-LNO/carbon cathode with preloaded Li_2O_2 (red curve). The scan rate used in these experiments was 0.02 mV/s with a voltage window from OCV (~2.8 V) to 4.5 V. (b) XRD spectra of the carbon-only cathode (i) before and (ii) after the SASV experiment, and nr-LNO/carbon cathode (iii) before and (iv) after the SASV experiment. The inset in figure (a) shows the loading verification of Li_2O_2 on nr-LNO/carbon cathode charged galvanostatically using 100 mA/g_{carbon}

5.4.5. Electrochemical Cycling

Figure 5.11 shows the cycling performance of the battery cells containing carbon cathodes with and without nanorod LNO electrocatalyst. In this study, a loading of 40 wt% nr-LNO on carbon was employed for consistency with literature reports.[43,53] In these experiments, the cells were allowed to discharge down to a potential of 2.0 V and charge up to a potential of 4.5 V with a maximum specific capacity of 500 mAh/g_{carbon} and a rate (current density) of 100 mA/g_{carbon}. It was observed that both cells started with a charge/discharge round-trip columbic efficiency of approximately 100 %. After 15 charge/discharge cycles, the charge specific capacity of the battery cell with carbon only cathode started decreasing, suggesting the potential formation of undesired discharge by-products that can no longer dissociate at potentials below 4.5 V. This was supported by the XRD pattern plotted in Figure 5.12 i, which shows the presence of Li_2CO_3 (undesired discharge product) peaks in the carbon-only cathode after the electrochemical cycling experiment.

On the other hand, the battery cell with cathode containing LNO nanorods exhibited stable charging/discharging specific capacities for over 20 cycles (corresponding to 180 h of continuous cycling). Characterization of the cathodes after cycling using XRD (Figure 5.12 ii) showed no evidence of the formation of any undesired discharge products during the experiment. Based on these results, we can conclude that the presence of the LNO nanorods improved the stability of the carbon cathode by suppressing the formation of the undesired discharge products during the electrochemical cycling experiments.

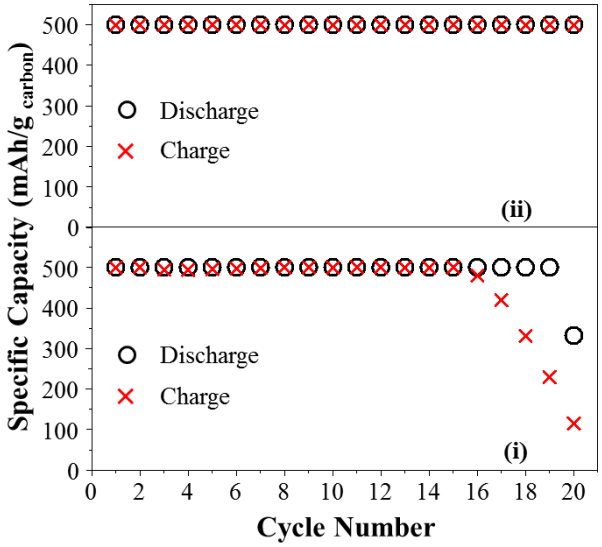

Figure 5.11 Charge/discharge cycling performance of battery cells containing (i) carbon-only cathode, and (ii) nr-LNO/carbon cathode. A limiting specific capacity of 500 mAh/g_{carbon} and a current density of 100 mA/g_{carbon} were used in these experiments

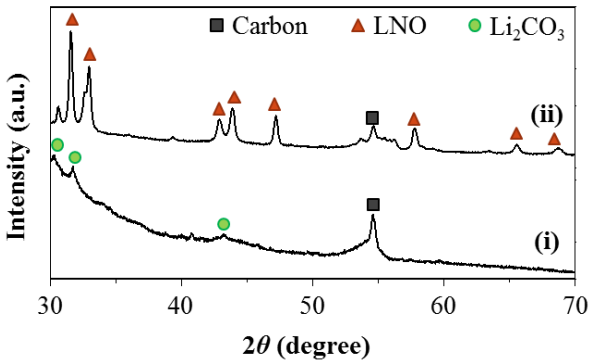

Figure 5.12 XRD spectra of (i) the carbon-only cathode, and (ii) nr-LNO/carbon cathode after 20 charge/discharge cycles

5.5. Conclusions

We have demonstrated the ability to utilize a reverse-microemulsion method to synthesize layered nickelate oxide (LNO) nanostructures with rod-shaped morphology as active and stable cathode electrocatalysts for non-aqueous Li–O_2 cathodes. We have found that LNO nanorods are more active than LNO nanospheres in Li-O_2 batteries. Our electrochemical studies show that the incorporation of LNO nanorods in carbon-based cathodes for Li–O_2 cells resulted in the lowering of the charging potential, and the enhancement of the reversible specific discharge capacities as compared to the battery cells with carbon-only cathodes. These improvements are attributed to the fact that LNO nanorods facilitate the formation of smaller Li_2O_2 particles, and catalyze oxygen evolution reaction during charging with a lower energy barrier than carbon. Electrochemical cycling experiments also show that LNO nanorods enhanced the stability of the battery cells by minimizing the formation of undesired discharge products. We anticipate that the controlled synthesis of highly active LNO electrocatalysts, such as the one described here, will provide a new strategy for synthesizing nanostructured, layered metal oxide systems and open up opportunities for utilizing them as effective non-precious metal-based cathode electrocatalysts for high energy storage systems.

CHAPTER 6. TUNING THE ACTIVITY OF NANOSTRUCTURED, NON-PRECIOUS METAL OXIDES FOR LOW TEMPERATURE ELECTROCHEMICAL OXYGEN REDUCTION

6.1. Summary

A highly efficient and kinetically favorable oxygen reduction reaction (ORR) is pivotal in advancing reliable energy conversion and storage systems, such as fuel cells and metal-air batteries. To date, Pt-based electrocatalysts exhibit the best performance for ORR but are limited by high cost. In this contribution, we explore the potential of non-stoichiometric, layered mixed metal oxides belonging to the Ruddlesden–Popper (R-P) series as promising, non-precious metal based electrocatalysts for ORR. We systematically study the effect of the transition metal site composition using well-defined nanostructures of these oxides terminated by (001) surface facets. Using rotating ring disk voltammetry studies, we show that doping the Ni site with Mn ($La_2Ni_{0.875}Mn_{0.125}O_{4+\delta}$) leads to the best ORR activity among all the oxide compositions considered (Cr, Co, Ni and Cu). Detailed kinetic analyses demonstrate that nanostructured Mn-doped LNO also exhibits the highest selectivity toward the desired, direct $4e^-$ pathway for ORR. Furthermore, stability tests via cyclic voltammetry scans show that Mn-LNO is stable over the course of cycling with minimal change in activity induced by degradation of the carbon support.

6.2. Introduction

Diminishing petroleum resources[55] and increasing carbon dioxide emissions[7] have become contemporary challenges inducing the need to shift our dependence from fossil fuels to more sustainable energy sources.[250] In recent years, much attention has been drawn to the development of reliable energy conversion and storage devices,[251] such as fuel cells, electrolyzers and metal-air batteries. Many of these systems are limited by the inefficient chemical transformations associated

with electrochemical oxygen reduction (ORR) and evolution reactions (OER).[171,252] It has been shown that ORR in alkaline and acidic media can proceed via two pathways: (i) the direct $4e^-$ path (desired pathway) where O_2 is reduced to $4OH^-$ ions in solution in the presence of 4 electrons ($O_2 + 2H_2O + 4e^- \Rightarrow 4OH^-$), or (ii) the $2e^-$ path, which leads to the formation of H_2O_2, an undesired reaction product due to its corrosive nature and inefficient electron transfer ($O_2 + H_2O + 2e^- \Rightarrow OOH^- + OH^-$). H_2O_2 can be further electrochemically decomposed to OH^- via another $2e^-$ step forming OH^- ions in solution ($OOH^- + H_2O + 2e^- \Rightarrow 3OH^-$). Precious metal-based catalysts, such as platinum and palladium, exhibit the best ORR activity and selectivity to the 4-electron path, but are limited by the high cost, scarcity, and poor long-term stability.[253,254]

Comparable activities to platinum-based electrocatalysts have been reported for transition metal oxide electrocatalysts. For example, a superior synergetic chemical coupling effect between Co_3O_4 nanoparticles and nitrogen-doped, mildly-reduced graphene oxide has been reported, which led to limited (< 6%) formation of hydroperoxide (intermediate in the undesired $2e^-$ ORR path).[146] Further improvements in the electrocatalytic activity were achieved by incorporating Mn into the aforementioned cobalt spinal oxide.[255] The enhanced activity was attributed to the substitution of Co^{3+} sites with the more active Mn^{3+} sites, as characterized by X-ray near-edge structure (XANES). The oxidation state of Mn has been shown to affect the ORR activity and selectivity, with Mn^{3+} exhibiting the highest activity and selectivity to the direct 4e- path.[147,256,257,258] Non-stoichiometric mixed ionic-electronic conducting oxides, such as perovskites (ABO_3, where A = lanthanide or alkali earth metal and B = transition metal) have also gained interest for ORR.[161] Mn-based perovskite have been shown to exhibit the highest activity, consistent with the presence of Mn^{3+} in the perovskite structure.[255,256] Design principles have been devised for identifying

optimal perovskite materials for ORR [160,171,257,259-269], but they have not been successfully extended to other non-stoichiometric metal oxide systems.[270]

Ruddlesden–Popper (RP) oxides (A_2BO_4 – first series) are another class of non-stoichiometric, mixed ionic-electronic conducting oxides with high potential for ORR and OER. These materials are characterized by a layered structure of alternating rock-salt and perovskite layers. They have been shown to exhibit excellent activity for high temperature ORR due to their high oxygen transport and exchange properties.[179,180] The potential of these oxides as catalysts for low temperature electrochemical reactions has not been fully explored. Unlike perovskites, these oxides display a hyper-oxygen stoichiometry, accommodating excess oxygen atoms in the rock-salt layers leading to variations in the oxidation state of the B-site transition metal.[191,271] This characteristic has given rise to interesting catalytic/electrocatalytic behaviors of these oxides toward chemical/electrochemical reactions involving oxygen.[272]

In this contribution, the activity and stability of nanostructured lanthanum nickelate oxides with varying B-site composition for ORR in alkaline medium were investigated. The electrocatalytic activity toward ORR at room temperature in alkaline media is determined using rotating ring-disk studies. Post-reaction characterization is carried out on the thin films deposited on the glassy carbon (GC) disk electrode, while catalyst stability is tested using extensive electrochemical cycling via repeated cyclic voltammetry scans. We show that even small variations in the composition of the B-site can substantially increase the electrocatalytic ORR activity of the studied complex metal oxides. The structure-performance studies show that Mn-doped lanthanum nickelate oxide exhibits the best ORR performance.

6.3. Experimental Details

6.3.1. Catalyst Synthesis

All chemicals were used as commercially received without further purification. The nanostructured electrocatalysts were synthesized using a quaternary reverse-microemulsion method as reported elsewhere.[233] Two separate reverse-microemulsions were first prepared, with each containing a quaternary reverse-microemulsion system composed of cetyltrimethylammonium bromide (CTAB)/water/hexane/n-butanol. One microemulsion was formed by mixing 4.0 mmol of $La(NO_3)_3 \cdot 6H_2O$ (99.999 %, Sigma-Aldrich), 1.75 mmol of $Ni(NO_3)_2 \cdot 6H_2O$ (98 %, Alfa Aesar) and 0.25 mmol of the corresponding B-site metal nitrate or chloride (Mn, Co, Ni, Cu and Cr) in 0.8 mL of deionized water, and the other one was formed by mixing 1.155 g of KOH pellets (ACS grade, Sigma-Aldrich) and 5.6 mL of deionized water. In each microemulsion system, the amount of CTAB, hexane, and n-butanol was fixed at 11 g, 56 mL and 11 mL, respectively. After the solutions were well mixed, the microemulsion system containing the base was added to the system containing the metal salts under stirring (1200 rpm). The mixture was maintained under the same conditions for 4 hours to form the gel suspension containing the precipitated complex metal hydroxide. The solid gel was collected by centrifugation (1000 rpm, 1 min). This was followed by washing multiple times using ethanol and deionized water. The solid gel was then dried under static air at 80 °C for 12 hours and calcined at 835 °C for 2 hours under argon in a quartz tubular reactor.

6.3.2. Thin-Film Preparation

Catalyst slurries were prepared by ultrasonicating 15 $mg_{catalyst}$, 3 mg_{carbon} (XC-72R, FuelCell store), 64.5 μl_{nafion} (5 wt% nafion solution, ionpower) in 2.99 ml (3:1 DI water to 2-propanol (IPA) volume ratio) in an iced bath for 30 minutes.[204] Prior to thin-film deposition, the

GC disk electrode was polished to a mirror-finish using 0.05 μm alumina suspension (Allied High Tech Products) on a 2.875" microfiber cloth (Buehler), followed by sonication in DI water and IPA. The GC disk substrate was left to dry at room temperature under nitrogen flow. 10 μL of the aliquot slurry was drop-casted on the 5 mm diameter GC disk electrode while rotating the disk at 700 rpm to provide better distribution of the catalyst film and to minimize the coffee-ring effect.[205] The final loadings of the catalyst, carbon and nafion are 250 $\mu g/cm^2$, 50 $\mu g/cm^2$ and 50 $\mu g/cm^2$, respectively.

6.3.3. Electrochemical Measurements

Electrochemical tests were performed in a 0.1 M KOH (prepared by diluting a standard solution, Sigma-Aldrich) electrolyte solution in a 30-ml glass electrochemical cell. The disk electrode used in this study was glassy carbon (GC, 5 mm diameter) equipped with a platinum ring electrode. A platinum coil was used as the counter electrode, while Hg/HgO in 20 wt.% KOH (Koslow) was used as the reference electrode. Prior to each experiment, the reference electrode was calibrated against the hydrogen reference electrode (see Section 3.4.8), and from this point herein, all voltages reported in this study are referenced with respect to the reversible hydrogen electrode (RHE), unless otherwise specified.

Prior to testing, the electrolyte was saturated with argon (20 sccm) through a bubbler immersed in the electrolyte. Impedance spectroscopy studies were performed using VersaSTAT (Princeton Applied Research) at high frequencies (~ 35 kHz) with a 10 mV excitation signal. The resistance was found to be in the range of 40 to 45 Ω and is used to remove the effect of the ohmic losses (referred to as $E_{iR\text{-}free}$) from the detected voltage. Cyclic voltammograms (CVs) were first collected in Ar-saturated electrolyte multiple times at 50 mV/s until reproducible voltammograms were achieved using a bipotentiostat (Pine Instruments) equipped with an MSR rotator and

controlled using AfterMath™. Background linear sweep voltammetry (LSV) was collected at various rotational speeds (i.e. 100 rpm, 225 rpm, 400 rpm, 625 rpm, 900 rpm, 1225 rpm, 1600 rpm, 2025 rpm and 2500 rpm) at 10 mVs^{-1} cathodic scan rate from 1.2 V to 0.05 V. The platinum ring potential was held at 1.25 V (which represents the oxidation of H_2O_2 at a sufficient diffusion-limiting current).[273] The same experiments were performed under a flow of oxygen (20 minutes of oxygen bubbling was found to be sufficient to reach saturation). Data were corrected by subtracting the O_2-saturated from the Ar-saturated voltammograms to account for the capacitance corrections, while the ohmic losses are accounted for by subtracting (iR) from the observed potential ($E_{applied}$-iR) where i is the detected current value and R is the uncompensated electrolyte resistance discussed above. All electrochemical tests were collected within a 2-hour period to avoid any interference of glass etching in alkaline media[274] at room temperature (~ 21°C).

The activity of the catalysts towards chemical decomposition of H_2O_2 was evaluated for the synthesized oxides, as well as the pure metal oxides (refer to Section 3.4.9). To determine the activity of the catalysts towards electrochemical reduction of H_2O_2, the same RDE experiments were performed by injecting 25mM of H_2O_2 to the existing electrolyte (0.1 M KOH), and scanning the potential from 1.2 to 0.05 V at 10 mV/s at various rotation rates.[275]

Electrochemical stability tests of XC-72 carbon with and without catalyst were performed by cycling the working electrode for 10,000 cycles between the potential window of 0.6 V – 1.0 V at 0.1 Vs^{-1}. Linear sweep voltammograms before and after 10,000 cycles were used as a measure of catalyst stability by observing any changes in the onset potential or the current densities at the diffusion limited region.

6.3.4. Characterization

The morphology of each sample was analyzed using a field-emission scanning electron microscope (FESEM, JSM-7600, JEOL Inc., Japan) at the accelerating voltage of 15 kV, equipped with an energy dispersive spectroscopy (EDS) detector to evaluate the compositional atomic ratio of the metal oxides. Elemental analysis of the synthesized oxides catalysts was performed using an Agilent 7700x inductively coupled plasma-mass spectrometer (ICP-MS). The X-ray diffraction (XRD) characterization of each sample was performed with a powder X-ray diffractometer (Smartlab, Rigaku Inc., Japan) using Cu Kα radiation (λ = 0.15418 nm). XRD pattern of fresh electrocatalysts were recorded over 2θ values of 20°–80° at a rate of 2°/min. X-ray Photoelectron Spectroscopy (Kratos axis ultra XPS, using a monochromatic Al K-α source) was used to determine the oxidation state of the A and B site metals in the oxide before and after electrochemical studies. The physical surface areas for all electrocatalysts were determined by N_2 physisorption studies using the Micromeritics ASAP 2020 analyzer. The interstitial oxygen content (δ) of the synthesized materials was determined using iodometric titration.[276]

6.4. Results and Discussion

6.4.1. Catalyst Synthesis

In the previous chapter (Chapter 5), we have reported on the synthesis of well-controlled nanostructures of first-series, R-P oxides mainly terminated by (001) surface facets of the B-site transition metal oxide layers.[179,180,233,234] The same method was adapted here to synthesize $La_2Ni_{0.88}M_{0.12}O_4$ with varying B-site dopant, M, which refers to Cr, Mn, Co, Ni and Cu ($La_2Ni_{0.88}Cr_{0.12}O_4$ (Cr-LNO), $La_2Ni_{0.88}Mn_{0.12}O_4$ (Mn-LNO, $La_2Ni_{0.88}Co_{0.12}O_4$ (Co-LNO), La_2NiO_4 (LNO), $La_2Ni_{0.88}Cu_{0.12}O_4$ (Cu-LNO)). We note that the loading of the dopant was kept low to assure stability of the R-P structure in all oxides with different compositions.[191,277] The XRD

spectra of the synthesized oxide electrocatalysts (Figure 6.1 a) clearly show that all of the oxides have the same crystal structure ascribed to the K_2NiF_4-type tetragonal structure within the *I4/mmm* space group.[233] Figure 6.1 (b) shows the SEM images of the nanostructures, demonstrating the uniform distribution of the nanorod morphology among all catalysts.

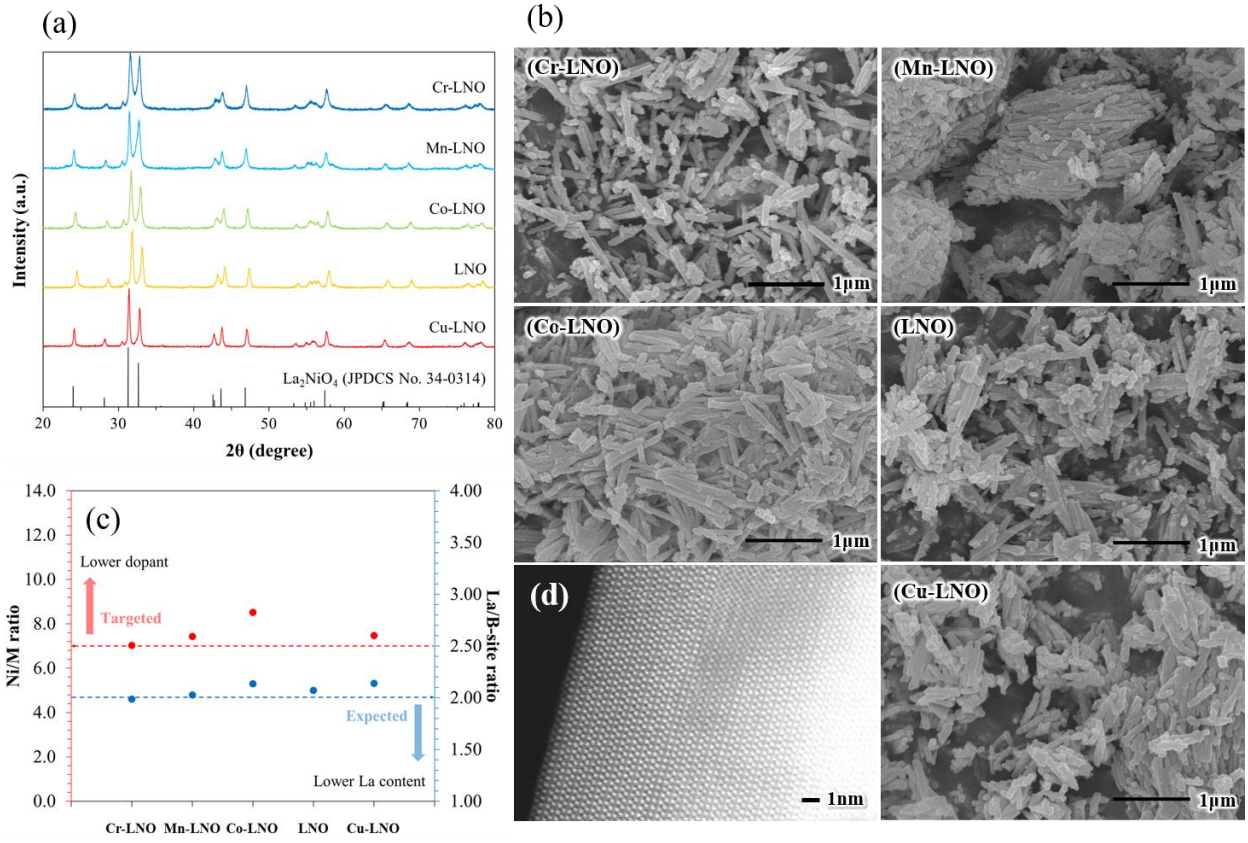

Figure 6.1 (a) XRD spectra, (b) FE-SEM images and (c) ICP analysis of the synthesized R-P oxides. The M in Ni/M ratio represents the dopant amount (Cr, Mn, Co and Cu) (d) Atomic resolution HAADF image of a Co-LNO sample

N_2 physisorption studies show that all synthesized nanostructured oxides have comparable physical surface areas of approximately 12.8 ± 1 m^2 g^{-1}. The chemical composition of all the oxides was confirmed to be within 5% error of the intended composition using ICP-MS (Figure 6.1 c). The B-site transition metal terminated (001) surface has also been confirmed for all synthesized electrocatalysts using atomic resolution HAADF as shown in Figure 1d for Co-LNO. Iodometric titration experiments were used to determine the oxygen non-stoichiometry of the different oxides.

The titration results show that all oxides have a comparable interstitial oxygen content (δ) of approximately 0.14 ± 0.02.

6.4.2. Electrochemical Performance

Cyclic voltammograms (CVs) of the synthesized oxides deposited on glassy carbon electrodes in Ar-saturated electrolyte (Figure 6.2) show no significant electrochemical reduction and/or phase change of these materials. CVs obtained in O_2-saturated electrolyte indicate an increased activity of these oxides compared to carbon. The magnitude of reduction peaks for all oxides was significantly higher compared to the reduction peak of bare carbon at the same potential of 0.6 V (see Figure 6.2). This increase in reduction peak confirms the ORR activity of the oxides and the negligible contribution in activity from XC-72 carbon support.

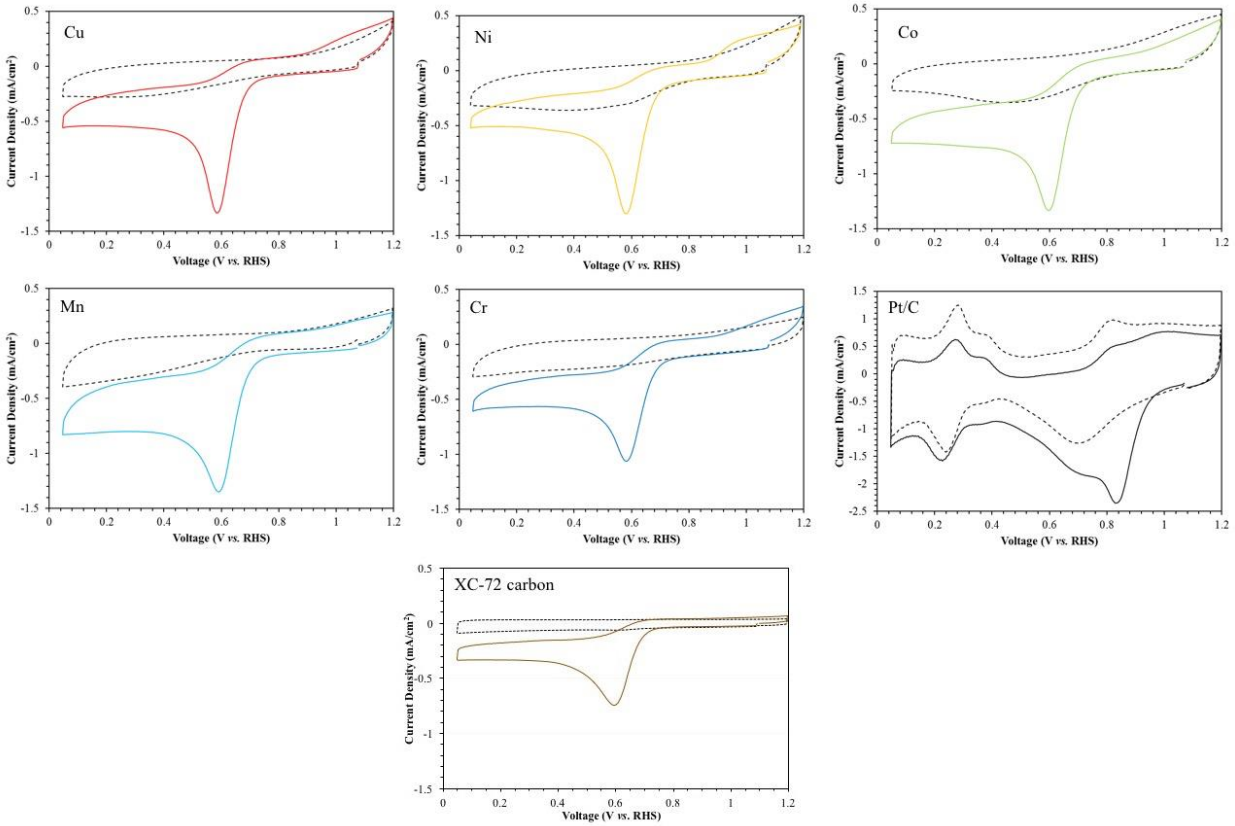

Figure 6.2 Cyclic Voltammograms (CVs) of $La_2Ni_{0.875}M_{0.125}O_4$ (M is specified in the figure), bare XC-72 carbon, & Pt/C deposited on glassy carbon electrode (5 mm diameter) in O_2-saturated (solid lines) and Ar-saturated (dash lines) 0.1 M KOH electrolyte using 50 mV s^{-1} scan rate.

To investigate the inherent catalytic activity of these mixed-metal oxides, rotating ring disk electrode (RRDE) studies (Figure 6.3) in O_2-saturated 0.1 M KOH solution at different rotation speeds were performed. The polarization curves of the different R-P oxides in an O_2-saturated 0.1 M KOH electrolyte are shown in Figure 6.4 (a). It is observed that the current densities in the diffusion-limited region vary as a function of oxide composition. For instance, Mn-LNO has a current density of ~ 5 mA cm^{-2} in the diffusion limited regime, followed by Co-LNO at about 4 mA cm^{-2}, while the rest of the R-P oxides (Cr-LNO, LNO and Cu-LNO) plateau at ~ 3 mA cm^{-2}. A closer look at the onset potential region (Figure 6.4 b) shows that Mn-LNO exhibits the lowest onset overpotential among the different oxide compositions, which suggests that the kinetic barrier for ORR is the lowest on Mn-LNO. The following ORR activity trend was observed as a function of oxide composition: Mn-LNO > Co-LNO > LNO ≈ Cu-LNO > Cr-LNO.

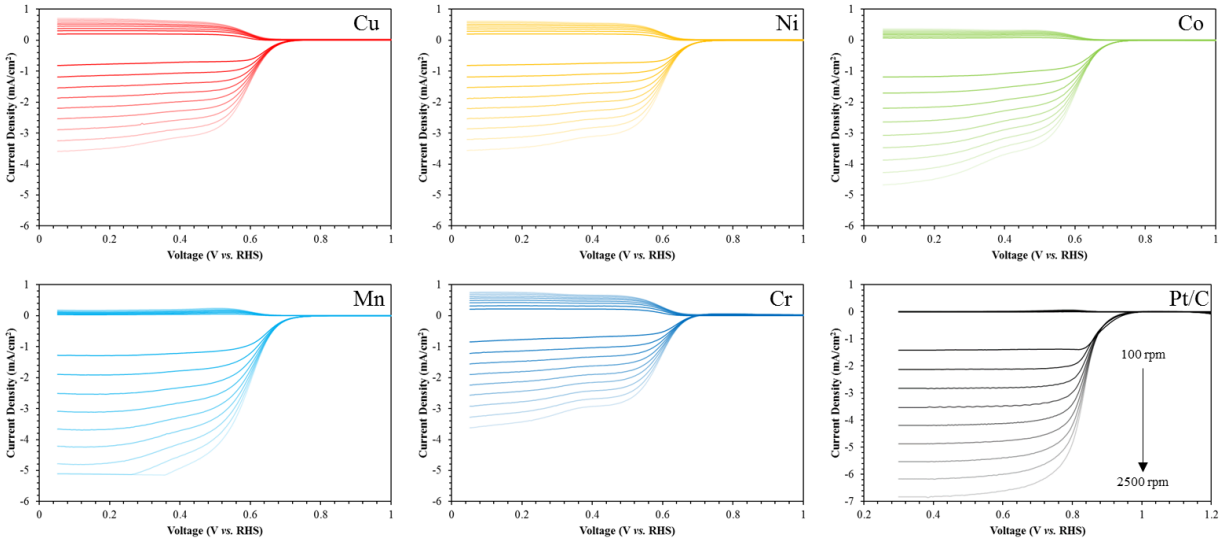

Figure 6.3 Rotating Ring-Disk Voltammograms of $La_2Ni_{0.875}M_{0.125}O_4$ (M is specified in the figure) and Pt/C electrocatalysts deposited on glassy carbon electrode (5 mm diameter) in O_2 saturated 0.1 M KOH electrolyte at various rotating speeds (9 perfect squares between 100 and 2500 rpm) using 10 mVs^{-1} scan rate. The catalyst loading in these experiments was fixed at 250 $\mu g/cm^2$ for the oxides and 65 $\mu g/cm^2$ for commercial Pt/C. The negative current value is related to the disk activity while the positive current values represent the ring electrode activity (held at 1.2 V constant potential throughout the measurement). The Pt/C voltammetry scans show that the diffusion limited current density is about -5.6 mA/cm^2 at 1600 rpm, which agrees with the reported value for $4e^-$ ORR on single and poly-crystalline Pt electrodes. The onset potential for the control experiment with Pt/C also is consistent with literature at 0.91 V.

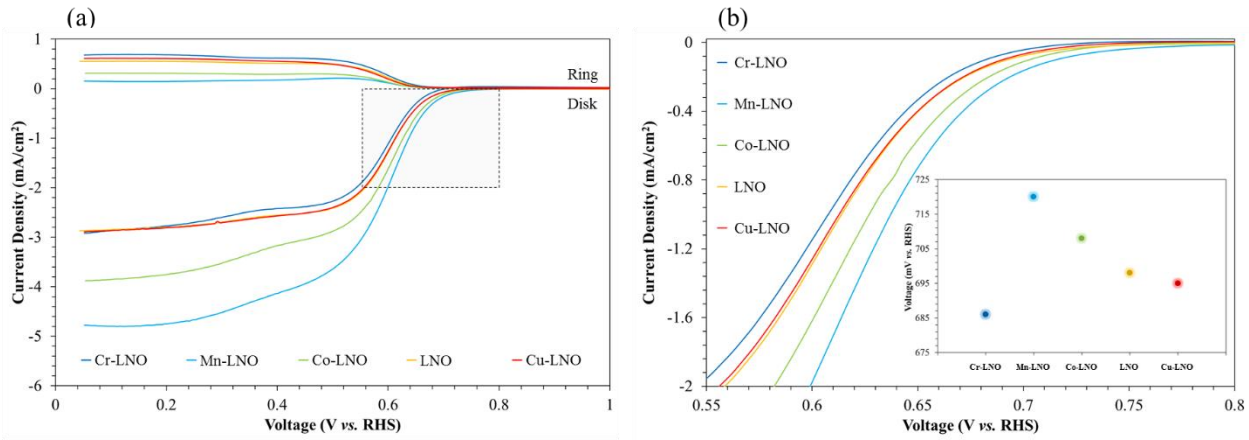

Figure 6.4 (a) Rotating ring-disk voltammograms of $La_2Ni_{0.875}M_{0.125}O_4$ thin-films in O_2-saturated 0.1 M KOH at 10 mV/s scan rate and 1600 rpm rotation speed. (b) Zoomed-in view of the boxed region shown in (a). Inset in (b) shows the plotted onset potentials of the oxides as a function of composition.

The number of electrons transferred for all the catalysts were determined using two methods: (i) Koutecky-Levich (K-L) analysis (Figure 6.5a), and (ii) RRDE analysis (Figure 6.5b) (see Chapter 3 for more details about (K-L) analysis and RRDE analysis). Both K-L and RRDE analyses show that ORR on nanostructured Mn-LNO selectively prefers a 4 e^- pathway. RRDE analysis also shows minimal H_2O_2 formation in the case of nanostructured Mn-doped LNO suggesting that it is the most selective toward the direct 4e^- ORR process, similar to platinum-based electrocatalysts.[7,8] The following trend was found between number of electrons involved in ORR and the compositions of the oxides: Mn-LNO > Co-LNO > LNO ≈ Cu-LNO > Cr-LNO.

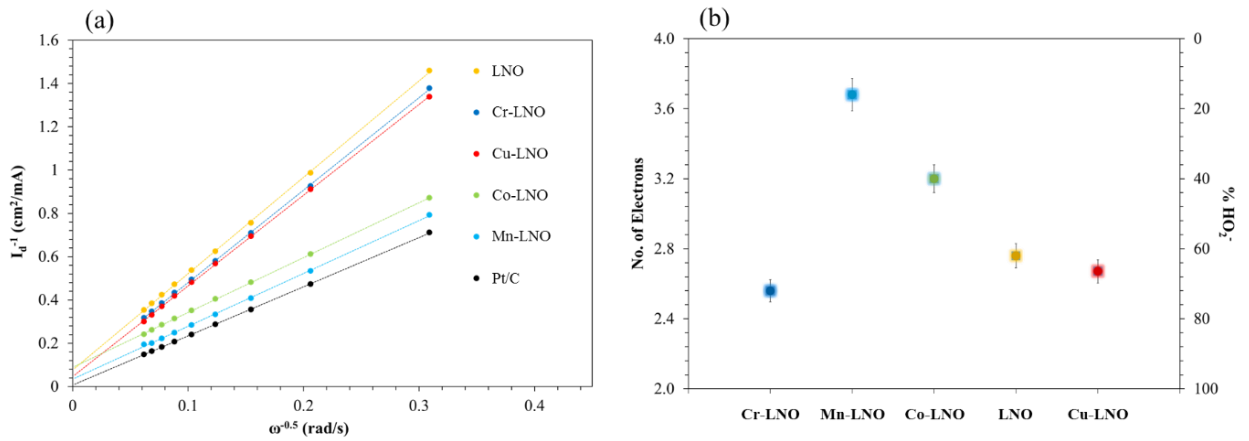

Figure 6.5 (a) Koutecky–Levich plots of $La_2Ni_{0.875}M_{0.125}O_4$ calculated at 0.4 V vs RHE (b) number of electrons transferred and hydrogen peroxide formation during ORR calculated at 0.4 V for all oxides.

6.4.3. Electrocatalytic Activity of Inherent Metal Oxides (NiO, MnO and Mn_2O_3)

Thus far, we have shown that nanostructured Mn-LNO exhibits the highest activity and selectivity towards the direct $4e^-$ path for ORR. This could potentially be due to Mn^{3+} in the structure.[13,14] The general oxidation state of the transition metal in the R-P oxide structure is +2, but this can vary depending on the oxygen hyper-stoichiometry, which can increase the oxidation state of the transition metal to +3. To gain insight on the nature of the active sites in nanostructured Mn-LNO, its ORR electrocatalytic activity was compared to the monometallic parent oxides of the transition metals, Mn and Ni (NiO, MnO and Mn_2O_3) (Figure 6.6). Figure 6.6 shows that the divalent transition metal oxides (NiO and MnO) are less active than the trivalent Mn oxide (Mn_2O_3), consistent with literature reports[278]. The polarization curve of NiO shows a more positive onset potential (0.82 V), which is explained by the electrochemical reduction behavior of the oxide to hydroxide on the catalyst surface, as observed during CV in an Ar-saturated electrolyte (Figure 6.7). The reduction peak potential (~ 0.87 V) is consistent with previous findings.[279] The onset potential of Mn_2O_3 is the closest to nanostructured Mn-LNO oxide, suggesting similar active sites for ORR.

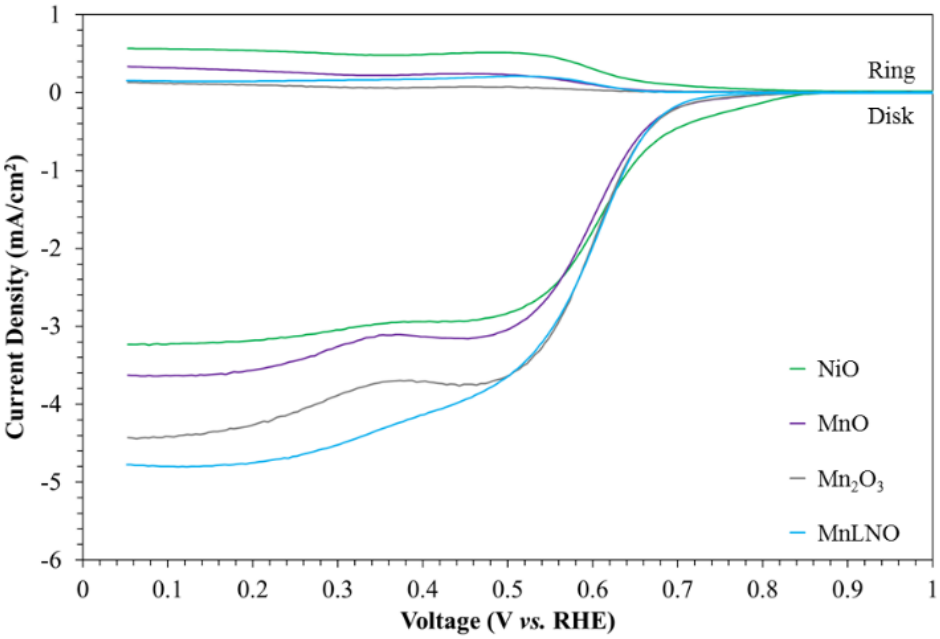

Figure 6.6 Rotating ring-disk voltammograms of NiO, MnO, Mn_2O_4 and Mn-LNO thin-films in O_2-saturated 0.1 M KOH at 10 mVs^{-1} scan rate and 1600 rpm rotation speed.

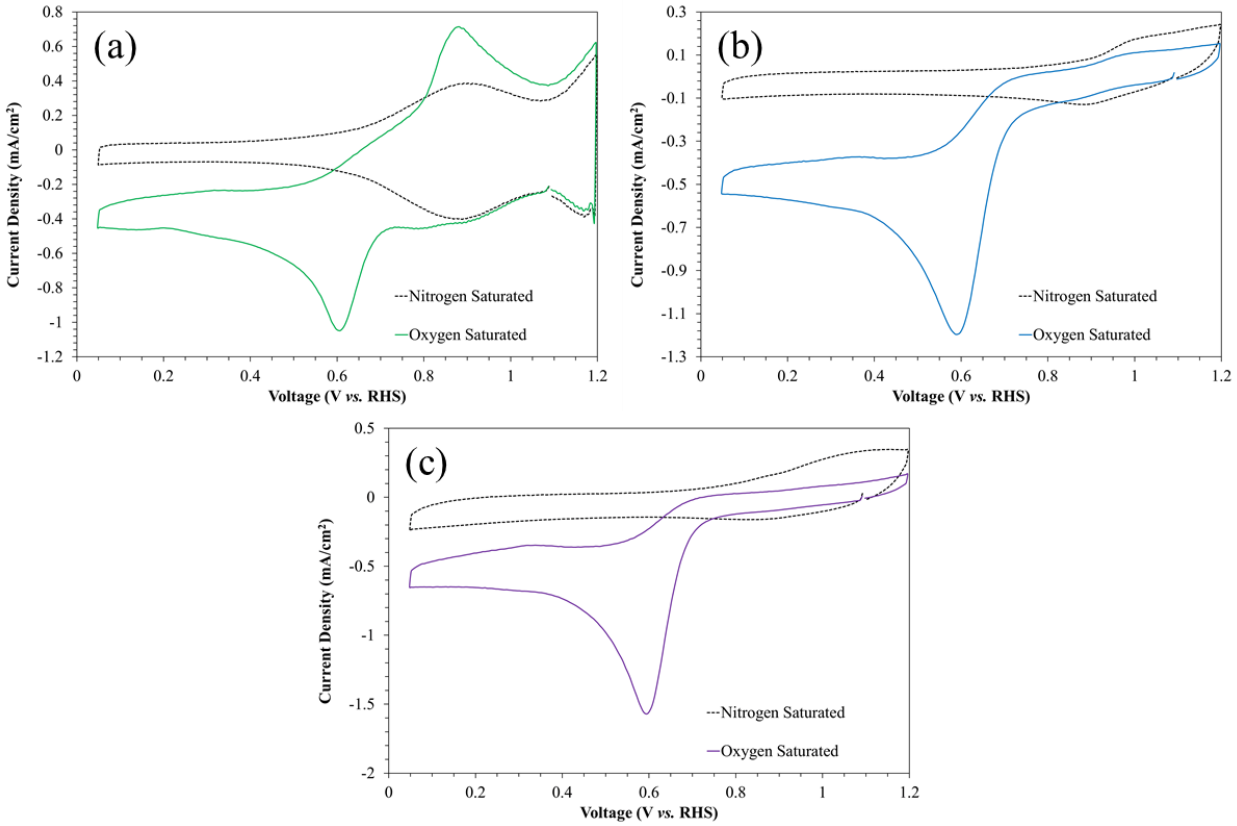

Figure 6.7 Cyclic Voltammograms (CVs) (a) NiO (b) MnO and (c) Mn_2O_3 deposited on glassy carbon electrode (5 mm diameter) in O_2-saturated (solid lines) and Ar-saturated (dash lines) 0.1 M KOH electrolyte using 50 mV s^{-1} scan rate.

6.4.4. ORR Kinetic Model

Reaction rate constant analysis for ORR in alkaline media was performed to determine the reaction pathway that dominates in these oxides. The commonly reported mechanistic pathways for ORR illustrated in Scheme 6.1 was used for this analysis.[280]

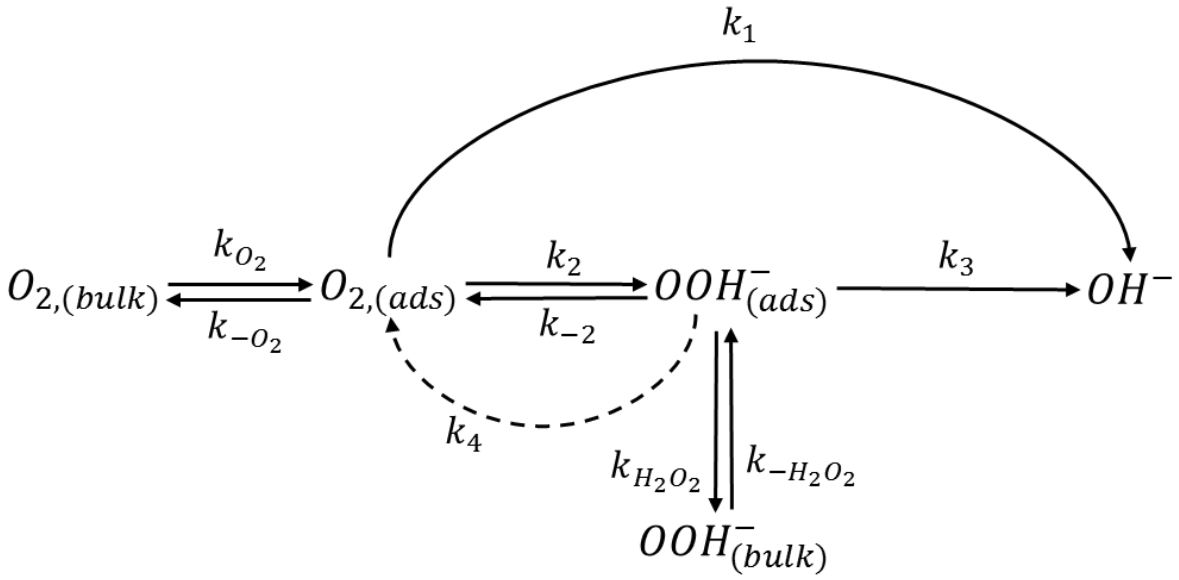

Scheme 6.1 ORR reaction scheme in alkaline media

In this reaction scheme, k_1 refers to the reaction rate constant associated with the direct $4e^-$ transfer path, while k_2 and k_3 are the reaction rate constants associated with the sequential $2e^-$ transfer path, and k_3 is the reaction rate constant associated with electrochemical H_2O_2 reduction (HPRR). Chemical decomposition (or oxidation) of H_2O_2 to H_2O and O_2 is also considered as represented by reaction rate constant, k_4. On the other hand, electrochemical oxidation of H_2O_2, which is represented by the reaction rate constant k_{-2}, is neglected since it is not favored on the applied potential window used for these experiments.

The kinetic model derivation is illustrated in the following sets of equations using these assumptions:

- No catalytic decomposition of H_2O_2 ($k_4 = 0$)

- Oxygen reduction reaction is taking place in the Tafel regime for both direct ($4e^-$) and series ($2e^-$) paths such that the values of k_{-1}, k_{-2} and k_{-3} are small and neglected
- Adsorption and desorption of H_2O_2 is fast
- The rate constant for H_2O_2 electrochemical oxidation is negligible
- Oxygen diffusion and H_2O_2 diffusion are in equilibrium

The reaction rates for each individual step:

$r_{O_2} = k_{O_2} C_{O_2 b}$

$r_{-O_2} = k_{-O_2} C_{O_2 *}$

$r_1 = k_1 C_{O_2 *}$

$r_2 = k_2 C_{O_2 *}$

$r_3 = k_3 C_{H_2O_2 *}$

$r_{H_2O_2} = k_{H_2O_2} C_{H_2O_2 *}$

$r_{-H_2O_2} = k_{-H_2O_2} C_{H_2O_2 b}$

The Levich equation relates the disk diffusion limited current (for O_2 diffusion)

$I_i = 0.62 n F A D_{O_2}^{2/3} \upsilon^{-1/6} C_i \omega^{1/2}$

The electrochemical reaction rate is directly related to the current value

$I_i = n F A r_i$

Accordingly;

$n F A k_{O_2} C_{O_2 b} = 0.62 n F A D_{O_2}^{2/3} \upsilon^{-1/6} C_{O_2 b} \omega^{1/2}$

$k_{O_2} = 0.62 D_{O_2}^{2/3} \upsilon^{-1/6} \omega^{1/2} = Z_1 \omega^{1/2}$

The same for r_{-O_2}

$k_{-O_2} = 0.62 D_{O_2}^{2/3} \upsilon^{-1/6} \omega^{1/2} = Z_1 \omega^{1/2}$

Same for $r_{H_2O_2}$ and $r_{-H_2O_2}$

$k_{H_2O_2} = k_{-H_2O_2} = 0.62 D_{H_2O_2}^{2/3} \upsilon^{-1/6} \omega^{1/2} = Z_2 \omega^{1/2}$

- Material balance for O_2*

$r_{O_2} - r_{-O_2} - r_1 - r_2 = 0$

$k_{O_2} C_{O_2 b} - k_{-O_2} C_{O_2 b} - k_1 C_{O_2 *} - k_2 C_{O_2 *} = 0$

$Z_1 \omega^{1/2} C_{O_2 b} - Z_1 \omega^{1/2} C_{O_2 *} - k_1 C_{O_2 *} - k_2 C_{O_2 *} = 0$

$Z_1 \omega^{1/2} (C_{O_2 b} - C_{O_2 *}) - (k_1 + k_2) C_{O_2 *} = 0$

- Material balance for H_2O_2*

$r_2 - r_3 - r_{H_2O_2} + r_{-H_2O_2} = 0$

$k_2 C_{O_2 *} - k_3 C_{H_2O_2 *} - Z_2 \omega^{1/2} C_{H_2O_2 *} + Z_2 \omega^{1/2} C_{H_2O_2 b} = 0$

$k_2 C_{O_2 *} - (k_3 + Z_2 \omega^{1/2}) C_{H_2O_2 *} = 0$

The disk current (I_d) is represented by the total reaction rates involving electron transfer

$I_d = 2FA(2r_1 + r_2 + r_3)$ reaction path 1 has double electron transfer compared to 2 and 3

$I_d = 2FA((2k_1 + k_2) C_{O_2 *} + k_3 C_{H_2O_2 *})$

The ring current (I_r) represents the electrochemical oxidation of H_2O_2 evolved from the disk during the reaction (2 e^-)

$I_r = 2ANFZ_2 C_{H_2O_2 *} \omega^{1/2}$

The ratio between the disk current and the ring current is calculated as following:

$$\frac{I_d}{I_r} = \frac{2FA\{(2k_1 + k_2)C_{O_2*} + k_3 C_{H_2O_2*}\}}{2ANFZ_2 C_{H_2O_2*}\omega^{1/2}} = \frac{1 + 2\,{}^{k_1}/_{k_2}}{N} + \frac{2(1 + {}^{k_1}/_{k_2})k_3}{NZ_2}\omega^{-1/2}$$

Plot of $\frac{I_d}{I_r}$ vs. $\omega^{-1/2}$

If the plot is linear, then;

$$Intercept = I_1 = \frac{1 + 2\,{}^{k_1}/_{k_2}}{N}$$

$$Slope = S_1 = \frac{2(1 + {}^{k_1}/_{k_2})k_3}{NZ_2}$$

Accordingly, calculation of k_1/k_2 ratio is possible from the intercept value (I_1)

$${}^{k_1}/_{k_2} = \frac{NI_1 - 1}{2}$$

Performing this computation throughout the whole voltage window, will lead to the evaluation of k_1/k_2 as a function of potential as shown in Figure 6.10.

To gain insight into the most dominant reaction pathway for ORR on these oxides, isolated studies for chemical decomposition of H_2O_2 and HPRR in an Ar-saturated alkaline solution (see Section 3.4.9) were performed. From the results of the H_2O_2 chemical decomposition experiments, it was determined that all the R-P oxides in this study show negligible catalytic activity toward these processes. The rate constant for these R-P oxides are found to be negligible. The insignificant activity of these oxides toward H_2O_2 decomposition was attributed to the absence of the B-site transition metals in a +4 oxidation state. This agrees with the previously reported case of Mn^{4+} that was found responsible for H_2O_2 recycling via disproportionation/decomposition.[12,14] This was confirmed by the XPS spectra (Figure 6.8), which show that all the B-site metals of the R-P oxides considered have a predominant oxidation state of +2/+3.

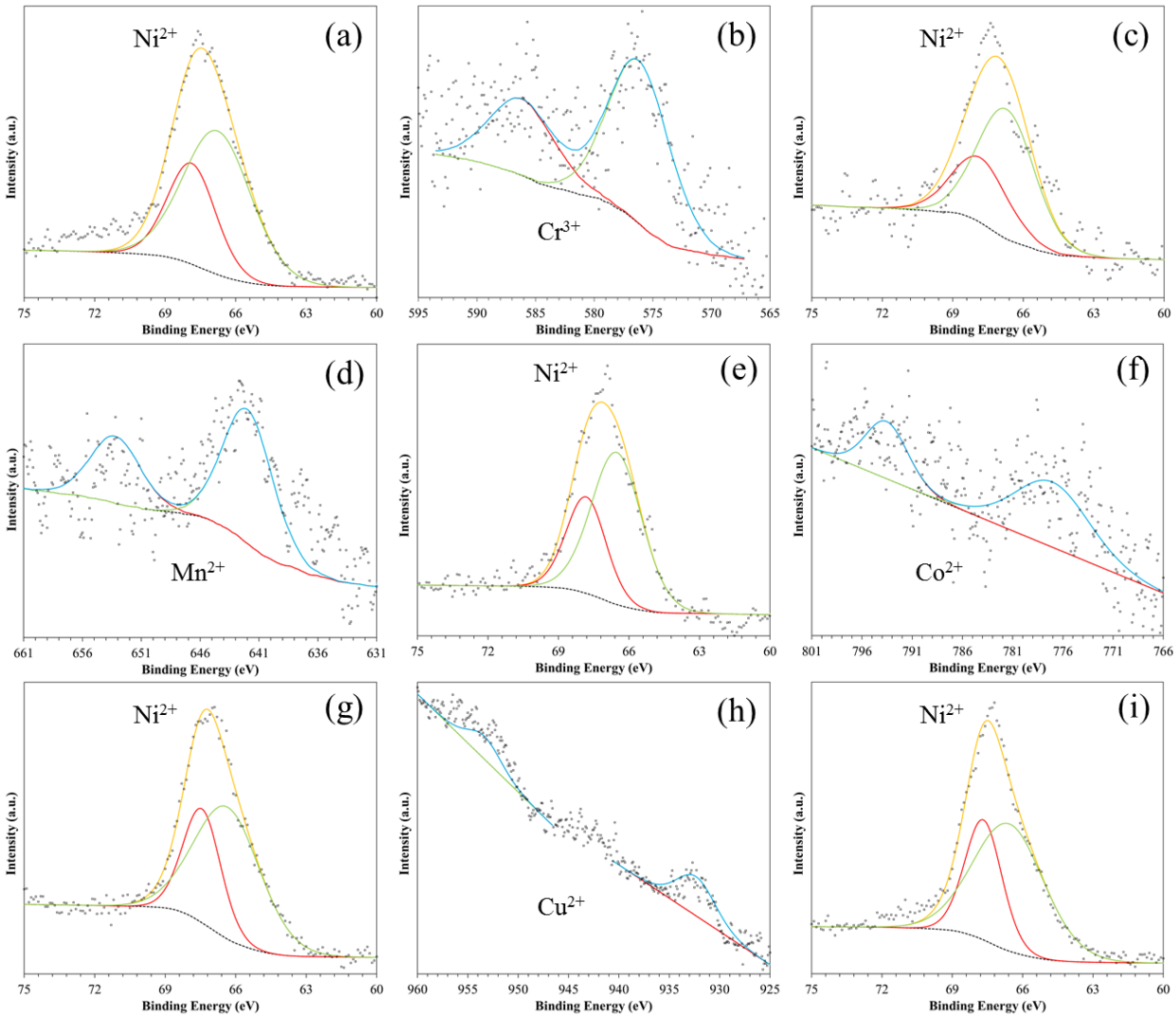

Figure 6.8 High-resolution XPS scan of Ni 3p region (Envelope: orange curve, Raw data: black squares, 3p $^{3}/_{2}$ fit: green curve and 3p ½ fit: red curve) in (a) Cr-LNO, (c) Mn-LNO, (e) Co-LNO, (g) Cu-LNO and (i) LNO. High resolution XPS scan of M-site 2p region (Envelope: blue curve, Raw data: black squares, 2p $^{3}/_{2}$ fit: green curve and 2p ½ fit: red curve) of: Cr-site in (b) Cr-LNO, Mn-site in (d) Mn-LNO, Co-site in (f) Co-LNO, Cu-site in (h) Cu-LNO.

6.4.5. Hydrogen Peroxide Reduction Reaction

HPRR studies were used to investigate the electrochemical reduction of H_2O_2 to OH^- and determine the rate constant, k_3. HPRR voltammograms of these oxides reveal that they exhibit negligible activity towards this step. Figure 6.9 shows that in the HPRR potential regime between 0.7 to 0.8 V, the current densities of these oxides (e.g. Cu-LNO, LNO, Co-LNO) do not appreciably change compared to a $LaMnO_3$ (used as a basis for comparison since it has shown

activity for this process). To further support these findings, the principle of hydrodynamic voltammetry was employed. Based on the reaction scheme shown above, the detected disk currents in the experiment come from two electrochemical reduction pathways (i.e. the reactions represented by k_1 and k_3) that produce OH^- ions. This initially makes it challenging to distinguish between the different pathways contributing to the production of OH^-. However, by varying the region of interest based on the potentials, RDE can be used to predict the change in electrochemical activity by differentiating the regions where these reactions happen, RDE can distinguish between the two different reduction activities, via., ORR and HPRR.[275] Figure 6.9 (b) shows the polarization curve for HPRR of an R-P oxide, (Co-LNO, as an example); at the HPRR potential region (0.7 to 0.8 V), there was no significant activity at the various rotation speeds.

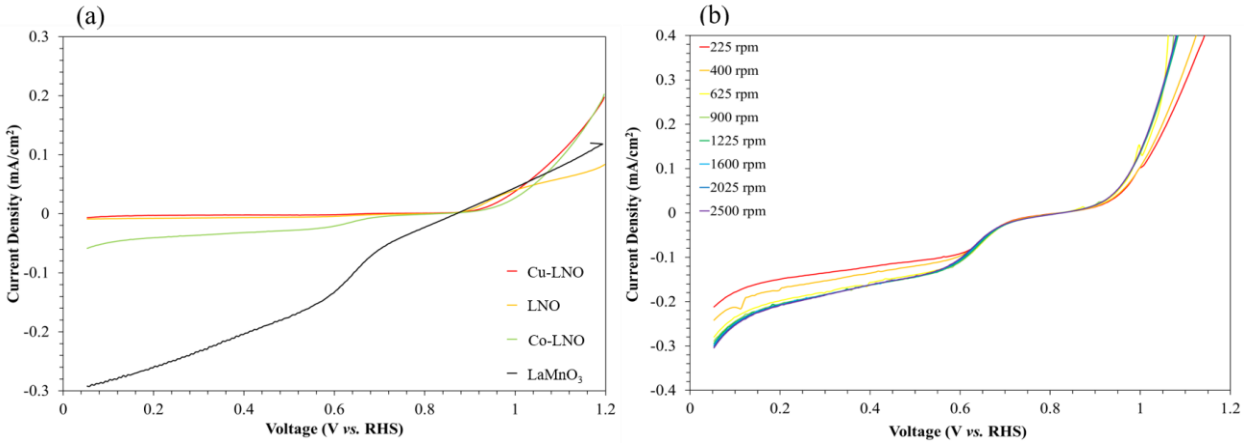

Figure 6.9 (a) HPRR voltammograms of R-P oxides (b) HPRR voltammogram of CoLNO at different speeds at 1600 rpm using 10 mV s^{-1} scan.

The absence of activity of R-P oxides for both HPRR and H_2O_2 chemical decomposition indicates that ORR activity of these materials cannot be enhanced by recycling H_2O_2 produced during ORR, since it can solely follow the direct $4e^-$ transfer path. Therefore, the activity of these oxides for ORR is predominantly a direct $4e^-$ transfer path on Mn-LNO and Co-LNO whereas, a single-step $2e^-$ transfer path leading to the production of OOH^- occurs on LNO, CuLNO and CrLNO. Analysis of the two reaction constants that were associated with these reactions (k_1 and

k_2) provides a clearer insight regarding the selectivity of these R-P oxides towards ORR. As illustrated in Figure 6.10, Mn-LNO has the highest k_1/k_2 ratio indicative of its high selectivity and activity toward ORR.

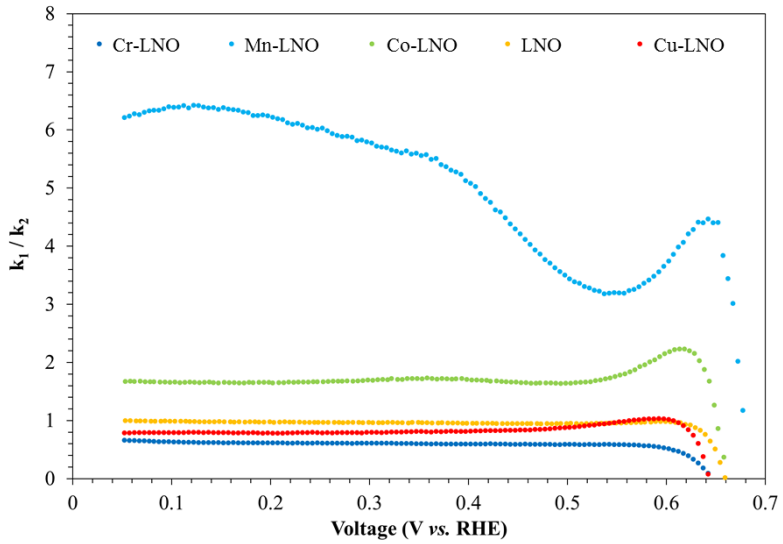

Figure 6.10 k_1/k_2 ratios of R-P oxides as a function of potential.

6.4.6. Electrochemical Cycling Stability Tests

As the best performing ORR electrocatalyst, nanostructured Mn-LNO was subjected to 10,000 cycles of CV scanning to study its stability. Figure 6.11 a shows the LSVs before and after 10,000 cycles of CV scans for Mn-LNO-containing electrode and carbon-only electrode. LSV curves indicate that there was minimal increase in overpotential (~52 mV @ -1 mA cm^{-2}) upon cycling. Similar on both Mn-LNO with carbon and carbon-only electrodes. This suggests that the increase in overpotential losses after 10,000 cycles could mainly be ascribed to the carbon support.

XPS characterization of the thin films containing nanostructured Mn-LNO before and after 10,000 cyclic voltammetry scans were also performed. Figures 6.11 b to 6 e show that the major oxidation states of the B site metals (Ni and Mn) are similar before and after cycling. This suggests that no detectable changes in the oxide structure have occurred during cycling, supporting the idea that the change in the activity of the electrode during cycling could stem from the carbon support.

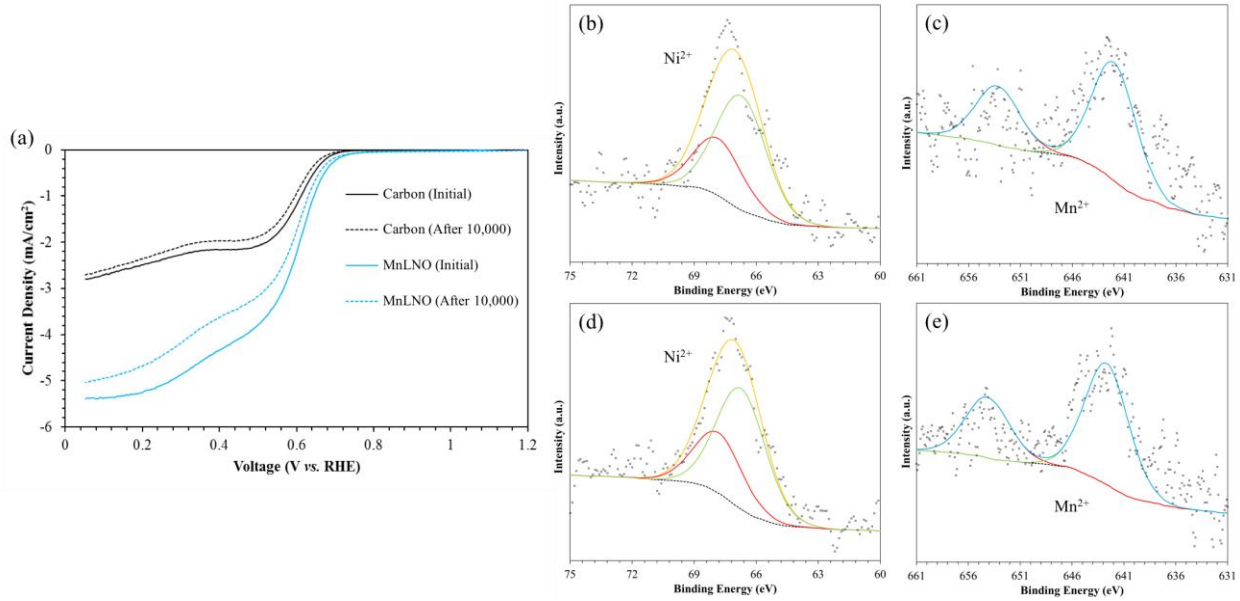

Figure 6.11 (a) Cycling stability test of XC-72 carbon thin films with (light blue curves) and without Mn-LNO (black curves): LSVs before and after 10,000 cycles. High-resolution XPS scan of Ni 3p region before (b) and after (d) 10,000 CV scans with orange curve as the envelope, scatter points are the raw data, and green and red curves for Ni 3p $^{3}/_{2}$ and 3p $^{1}/_{2}$ fit respectively. High-resolution XPS scan of Mn 2p region before (c) and after (e) 10,000 CV scans with orange curve as the envelope, scatter points are the raw data, and green and red curves for Mn 2p $^{3}/_{2}$ and 2p $^{1}/_{2}$ fit respectively.

6.5. Conclusions

In this contribution, we have utilized a reverse-microemulsion method to control the formation of nanorod lanthanum nickelate oxides with various transition metal dopants. Rotating ring-disk electrode studies show a superior behavior of nanostructured Mn doped LNO. We find that Mn-LNO exhibits the lowest overpotential for ORR with comparable product selectivity to platinum-based electrocatalysts. Its selectivity to the direct $4e^-$ process was verified by the minimum formation of hydroperoxide as detected by the ring electrode during the reaction. Based on all these observations, we attribute the increase in the electrocatalytic activity of manganese LNO to the existence of trivalent transition metal (Mn^{3+}) on the B-site terminated nanorods. The high ORR selectivity of Mn-LNO electrocatalyst is attributed the preferential direct $4e^-$ process, rather than the series of 2e- processes that involves formation of hydroperoxide as reaction

intermediate. Furthermore, we find that Mn-LNO electrocatalysts is chemically inert toward HPRR, reinforcing the previous finding that ORR proceeds via direct $4e^-$ reaction pathway. The stability of Mn-LNO has also been analyzed using extensive cycling via 10,000 cyclic voltammetry scans (as recommended by DOE testing protocol). Mn-LNO exhibits good stability (verified using XPS) with minimum degradation of the electrode induced by the carbon support.

CHAPTER 7. GENERAL CONCLUSIONS AND FUTURE WORK

7.1. Summary

In this thesis, a comprehensive study of the effect of the lanthanide and transition-metal site composition of first series R-P oxides on the ORR and OER activity at low temperatures is discussed. The combination of multiple spectroscopic and microscopic techniques, alongside electrochemical investigation methods, facilitated the identification of optimal nanostructured R-P oxides for these processes. This chapter briefs the major conclusion derived from this thesis. Also, it discusses future work that can possibly be implemented to further improve the ORR/OER electrocatalytic activity of these materials.

7.2. General Conclusions

This work demonstrates the ability to engineer first-order R-P series layered oxides with various chemical compositions. We have successfully synthesized high surface area pure-phase R-P oxides in different geometries (nanospheres and nanorods). These oxides were utilized in low temperature energy storage (Li-O_2 battery) and conversion (alkaline fuel cell) devices, as active electrocatalysts. Their electrocatalytic activity was examined by state-of-the-art electrochemical characterization techniques. The main conclusions drawn from this work are summarized below.

- The composition of the A-site in first-order Ruddlesden-Popper series of layered oxides (A_2BO_4) has an effect on the electrochemical activity of Li-O_2 cathodes. Among the lanthanides that form stable Ruddlesden-Popper oxide structures, La_2NiO_4 exhibits the best electrochemical performance when incorporated in Li-O_2 cathodes. The electrochemical performance of La_2NiO_4 electrocatalyst could be further improved by doping the A-site with alkaline earth metals, such as Ba. We show that $Ba_{0.25}La_{1.75}NiO_4$ exhibits the best discharge capacity and lowest OER potential when compared to undoped La_2NiO_4,

$Sr_{0.25}La_{1.75}NiO_4$ and $Ca_{0.25}La_{1.75}NiO_4$. The reason for this could be due to the fact that doping the La-site with Ba leads to an O surface chemistry that facilitates the oxygen evolution reaction with the lowest oxygen barrier. The low overpotential loss of $Ba_{0.25}La_{1.75}NiO_4$ during recharge might be influenced by the early high discharge voltage, which in turn could be explained by the formation of electrochemical reaction intermediate species (i.e. LiO_2) during discharge that stabilize at the catalyst surface. The dissociations of these lithium deficient materials are favorably decomposed (during recharge phase) at lower potentials than Li_2O_2 or Li_2O. These findings set the race in the discovery of more active electrocatalysts that can stabilize the formation of transient reaction products at room temperature.

- The reverse-microemulsion method developed in this thesis was successfully used to synthesize layered nickelate oxide (LNO) nanostructures with rod-shaped morphology that are highly active and stable cathode electrocatalysts for non-aqueous Li–O_2 cathodes. We have found that LNO nanorods are more active than LNO nanosphere in Li-O_2 battery. Our electrochemical studies show that the incorporation of LNO nanorods in carbon-based cathodes for Li–O_2 cells resulted in the lowering of the charging potential, and the enhancement of the reversible specific discharge capacities as compared to the battery cells with carbon-only cathodes. These improvements are attributed to the fact that LNO nanorods facilitate the formation of smaller Li_2O_2 particles, and catalyze oxygen evolution reaction during charging with a lower energy barrier than carbon. Electrochemical cycling experiments also show that LNO nanorods enhanced the stability of the battery cells by minimizing the formation of undesired discharge products. We anticipate that the controlled synthesis of highly active LNO electrocatalysts, such as the one described here,

will provide a new strategy for synthesizing nanostructured, layered metal oxide systems and open up opportunities for utilizing them as effective non-precious metal-based cathode electrocatalysts for high energy storage systems.

- Rotating ring-disk electrode studies of ORR in alkaline media showed a superior behavior of nanostructured Mn-doped LNO oxide with comparable product selectivity to platinum-based electrocatalysts. Its selectivity to the direct $4e^-$ process was verified by the minimum formation of hydroperoxide as detected by the ring electrode during the reaction. The stability of Mn-LNO was analyzed using extensive cycling via 10,000 cyclic voltammetry scans (as recommended by DOE testing protocol).[281] Mn-LNO exhibited good stability (verified using XPS) with minimum degradation of the electrode induced by the carbon support.

7.3. Future Work Directions

The conclusions drawn from chapter 4 in this thesis, can be further explored, to gain better understanding on the factors assisting the stabilization of lithium-deficient species on the catalyst surface. LiO_2 has shown to dissociate electrochemically at lower potentials than Li_2O_2.[25] Coupled electrochemical and spectroscopic techniques can be utilized to underline the reaction mechanism associated with the formation and dissociation of lithium oxides species.

In chapter 6, we have mainly discussed the effect of the B-site composition of first series R-P oxides on ORR in alkaline media. A future direction would include determining the effect of the B-site composition of R-P oxides toward OER in alkaline media. The effect of the B-site can also be investigated in Li-O_2 batteries. Initial kinetic behavior of these oxide electrocatalysts can be obtained by constructing Tafel plots (voltage vs. current density) using various discharge voltages, while monitoring the current response. The exchange current density can be extracted by

extrapolating the linear Tafel plot region to the x-axis (current density). The exchange current density can provide an insight to the inherent kinetic electrocatalytic activity of the catalyst employed. This value (exchange current density) represents the reaction rate at thermodynamic potential associated with each electrocatalyst.[282] Higher value correlates to faster kinetics, while lower value correlates to sluggish electrochemical reaction.

Another challenge with Li-air carbon cathode is the inability to conduct lithium ions. The liquid electrolyte is incorporated in the cathode to facilitate the mobilization of Li^+ to the active sites for the reaction to occur. Unfortunately, most of the non-aqueous electrolytes are very unstable under electrochemical oxidation conditions, leading to rapid deactivation of the battery cell.[216] To address this challenge, incorporation of high surface area carbon cathodes functionalized with crown ether groups that allow for transport of the Li^+ is a potential approach. 12-crown-4-ether ring is a cyclic tetramer of ethylene oxide that has been shown to exhibit high conductivity of lithium cations.[283] The hypothesis is that functionalizing the carbon cathode with these moieties will enhance the Li^+ conductivity throughout the electrode and open up opportunities for shielding the aprotic electrolyte from the electrochemical oxidation conditions at the cathode during operation.

APPENDIX STANDARD ELECTRODE POTENTIALS

Table A1 Standard electrode potentials in aqueous solution at 25 °C.[19]

Half-Cell Reaction	Standard Potential E^0 (volts)	Half-Reaction	Standard Potential E^0 (volts)
$Li^+ + e^- \rightarrow Li$	-3.05	$IO^- + H_2O + 2e^- \rightarrow I^- + 2OH^-$	0.49
$K^+ + e^- \rightarrow K$	-2.92	$Cu^+ + e^- \rightarrow Cu$	0.52
$Ca^{2+} + 2e^- \rightarrow Ca$	-2.76	$I_2 + 2e^- \rightarrow 2I^-$	0.54
$Na^+ + e^- \rightarrow Na$	-2.71	$ClO_2{}^- + H_2O + 2e^- \rightarrow ClO^- + 2OH^-$	0.59
$Mg^{2+} + 2e^- \rightarrow Mg$	-2.38	$Fe^{3+} + e^- \rightarrow Fe^{2+}$	0.77
$Al^{3+} + 3e^- \rightarrow Al$	-1.66	$Hg_2{}^{2+} + 2e^- \rightarrow 2Hg$	0.80
$2H_2O + 2e^- \rightarrow H_2 + 2OH^-$	-0.83	$Ag^+ + e^- \rightarrow Ag$	0.80
$Zn^{2+} + 2e^- \rightarrow Zn$	-0.76	$Hg^{2+} + 2e^- \rightarrow Hg$	0.85
$Cr^{3+} + 3e^- \rightarrow Cr$	-0.74	$ClO^- + H_2O + 2e^- \rightarrow Cl^- + 2OH^-$	0.90
$Fe^{2+} + 2e^- \rightarrow Fe$	-0.41	$2Hg^{2+} + 2e^- \rightarrow Hg_2{}^{2+}$	0.90
$Cd^{2+} + 2e^- \rightarrow Cd$	-0.40	$NO_3{}^- + 4H^+ + 3e^- \rightarrow NO + 2H_2O$	0.96
$Ni^{2+} + 2e^- \rightarrow Ni$	-0.23	$Br_2 + 2e^- \rightarrow 2Br^-$	1.07
$Sn^{2+} + 2e^- \rightarrow Sn$	-0.14	$O_2 + 4H^+ + 4e^- \rightarrow 2H_2O$	1.23
$Pb^{2+} + 2e^- \rightarrow Pb$	-0.13	$Cr_2O_7{}^{2-} + 14H^+ + 6e^- \rightarrow 2Cr^{3+} + 7H_2O$	1.33
$Fe^{3+} + 3e^- \rightarrow Fe$	-0.04	$Cl_2 + 2e^- \rightarrow 2Cl^-$	1.36
$H^+ + 2e^- \rightarrow H_2$	0.00	$Ce^{4+} + e^- \rightarrow Ce^{3+}$	1.44
$Sn^{4+} + 2e^- \rightarrow Sn^{2+}$	0.15	$MnO_4{}^- + 8H^+ + 5e^- \rightarrow Mn^{2+} + 4H_2O$	1.49
$Cu^{2+} + e^- \rightarrow Cu^+$	0.16	$H_2O_2 + 2H^+ + 2e^- \rightarrow 2H_2O$	1.78
$ClO_4{}^- + H_2O + 2e^- \rightarrow ClO_3{}^- + 2OH^-$	0.17	$Co^{3+} + e^- \rightarrow Co^{2+}$	1.82
$AgCl + e^- \rightarrow Ag + Cl^-$	0.22	$S_2O_8{}^{2-} + 2e^- \rightarrow 2SO_4{}^{2-}$	2.01
$Cu^{2+} + 2e^- \rightarrow Cu$	0.34	$O_3 + 2H^+ + 2e^- \rightarrow O_2 + H_2O$	2.07
$ClO_3{}^- + H_2O + 2e^- \rightarrow ClO_2{}^- + 2OH^-$	0.35	$F_2 + 2e^- \rightarrow 2F^-$	2.87

REFERENCES

(1) *National Oceanic & Atmospheric Administration (NOAA), monthly measurements*, www.esrl.noaa.gov.

(2) *NASA's Goddard Institute for Space Studies*, www.giss.nasa.gov.

(3) *Intergovernmental Panel on Climate Change 2013*, www.ipcc.ch/report/ar5/wg1.

(4) Girishkumar, G.; McCloskey, B.; Luntz, A. C.; Swanson, S.; Wilcke, W. *J Phys Chem Lett* **2010**, *1*, 2193.

(5) *U.S. Energy Information Administration, Monthly Energy Review*, www.eia.gov.

(6) *BP Statistical Review of World Energy 2016*, www.bp.com/statisticalreview.

(7) Obama, B. *Science* **2017**, *355*, 126.

(8) Dong, X.; Chen, L.; Liu, J.; Haller, S.; Wang, Y.; Xia, Y. *Science advances* **2016**, *2*, e1501038.

(9) Linden, D.; Reddy, T. *Handbook of Batteries, 4th Edition*; McGraw-Hill Education, 2010.

(10) Wang, J. J.; Li, Y. L.; Sun, X. L. *Nano Energy* **2013**, *2*, 443.

(11) Littauer, E. L.; Tsai, K. C. *J Electrochem Soc* **1976**, *123*, 771.

(12) Abraham, K. M.; Jiang, Z. *J Electrochem Soc* **1996**, *143*, 1.

(13) Pegis, M. L.; Roberts, J. A. S.; Wasylenko, D. J.; Mader, E. A.; Appel, A. M.; Mayer, J. M. *Inorg Chem* **2015**, *54*, 11883.

(14) Larcher, D.; Tarascon, J. M. *Nat Chem* **2015**, *7*, 19.

(15) Tse, E. C. M.; Barile, C. J.; Kirchschlager, N. A.; Li, Y.; Gewargis, J. P.; Zimmerman, S. C.; Hosseini, A.; Gewirth, A. A. *Nat Mater* **2016**, *advance online publication*.

(16) Chen, J.; Takanabe, K.; Ohnishi, R.; Lu, D.; Okada, S.; Hatasawa, H.; Morioka, H.; Antonietti, M.; Kubota, J.; Domen, K. *Chem Commun* **2010**, *46*, 7492.

(17) Jiao, Y.; Zheng, Y.; Jaroniec, M.; Qiao, S. Z. *Chem Soc Rev* **2015**, *44*, 2060.

(18) Song, C.; Zhang, J. In *PEM Fuel Cell Electrocatalysts and Catalyst Layers: Fundamentals and Applications*; Zhang, J., Ed.; Springer London: London, 2008, p 89.

(19) Bard, A. J.; Faulkner, L. R. *Electrochemical Methods: Fundamentals and Applications*; Wiley, 2000.

(20) Wang, Z.-L.; Xu, D.; Xu, J.-J.; Zhang, X.-B. *Chem Soc Rev* **2014**, *43*, 7746.

(21) Laoire, C. O.; Mukerjee, S.; Abraham, K. M.; Plichta, E. J.; Hendrickson, M. A. *J Phys Chem C* **2009**, *113*, 20127.

(22) Laoire, C. O.; Mukerjee, S.; Abraham, K. M.; Plichta, E. J.; Hendrickson, M. A. *J Phys Chem C* **2010**, *114*, 9178.

(23) Peng, Z. Q.; Freunberger, S. A.; Hardwick, L. J.; Chen, Y. H.; Giordani, V.; Barde, F.; Novak, P.; Graham, D.; Tarascon, J. M.; Bruce, P. G. *Angew Chem Int Edit* **2011**, *50*, 6351.

(24) Lu, J.; Lee, Y. J.; Luo, X. Y.; Lau, K. C.; Asadi, M.; Wang, H. H.; Brombosz, S.; Wen, J. G.; Zhai, D. Y.; Chen, Z. H.; Miller, D. J.; Jeong, Y. S.; Park, J. B.; Fang, Z. Z.; Kumar, B.; Salehi-Khojin, A.; Sun, Y. K.; Curtiss, L. A.; Amine, K. *Nature* **2016**, *529*, 377.

(25) Yang, J. B.; Zhai, D. Y.; Wang, H. H.; Lau, K. C.; Schlueter, J. A.; Du, P.; Myers, D. J.; Sun, Y. K.; Curtiss, L. A.; Amine, K. *Phys Chem Chem Phys* **2013**, *15*, 3764.

(26) Zhai, D. Y.; Lau, K. C.; Wang, H. H.; Wen, J. G.; Miller, D. J.; Lu, J.; Kang, F. Y.; Li, B. H.; Yang, W. G.; Gao, J.; Indacochea, E.; Curtiss, L. A.; Amine, K. *Nano Lett* **2015**, *15*, 1041.

(27) Zhai, D. Y.; Wang, H. H.; Lau, K. C.; Gao, J.; Redfern, P. C.; Kang, F. Y.; Li, B. H.; Indacochea, E.; Das, U.; Sun, H. H.; Sun, H. J.; Amine, K.; Curtiss, L. A. *J Phys Chem Lett* **2014**, *5*, 2705.

(28) Zhai, D. Y.; Wang, H. H.; Yang, J. B.; Lau, K. C.; Li, K. X.; Amine, K.; Curtiss, L. A. *J Am Chem Soc* **2013**, *135*, 15364.

(29) Wang, H. H.; Lee, Y. J.; Assary, R. S.; Zhang, C. J.; Luo, X. Y.; Redfern, P. C.; Lu, J.; Lee, Y. J.; Kim, D. H.; Kang, T. G.; Indacochea, E.; Lau, K. C.; Amine, K.; Curtiss, L. A. *J Phys Chem C* **2017**, *121*, 9657.

(30) Gittleson, F. S.; Sekol, R. C.; Doubek, G.; Linardi, M.; Taylor, A. D. *Phys Chem Chem Phys* **2014**, *16*, 3230.

(31) Peng, Z. Q.; Freunberger, S. A.; Chen, Y. H.; Bruce, P. G. *Science* **2012**, *337*, 563.

(32) Harding, J. R.; Lu, Y. C.; Tsukada, Y.; Shao-Horn, Y. *Phys Chem Chem Phys* **2012**, *14*, 10540.

(33) Fan, W. G.; Guo, X. X.; Xiao, D. D.; Gu, L. *J Phys Chem C* **2014**, *118*, 7344.

(34) Lu, Y. C.; Gasteiger, H. A.; Shao-Horn, Y. *J Am Chem Soc* **2011**, *133*, 19048.

(35) Zhu, D.; Zhang, L.; Song, M.; Wang, X. F.; Chen, Y. G. *Chem Commun* **2013**, *49*, 9573.

(36) Lu, J.; Lei, Y.; Lau, K. C.; Luo, X. Y.; Du, P.; Wen, J. G.; Assary, R. S.; Das, U.; Miller, D. J.; Elam, J. W.; Albishri, H. M.; Abd El-Hady, D.; Sun, Y. K.; Curtiss, L. A.; Amine, K. *Nat Commun* **2013**, *4*.

(37) Shen, Y.; Sun, D.; Yu, L.; Zhang, W.; Shang, Y. Y.; Tang, H. R.; Wu, J. F.; Cao, A. Y.; Huang, Y. H. *Carbon* **2013**, *62*, 288.

(38) Xu, J. J.; Wang, Z. L.; Xu, D.; Zhang, L. L.; Zhang, X. B. *Nat Commun* **2013**, *4*.

(39) Yang, Y.; Shi, M.; Zhou, Q. F.; Li, Y. S.; Fu, Z. W. *Electrochem Commun* **2012**, *20*, 11.

(40) Lu, Y.; Wen, Z. Y.; Jin, J.; Cui, Y. M.; Wu, M. F.; Sun, S. J. *J Solid State Electr* **2012**, *16*, 1863.

(41) Lim, H. D.; Song, H.; Gwon, H.; Park, K. Y.; Kim, J.; Bae, Y.; Kim, H.; Jung, S. K.; Kim, T.; Kim, Y. H.; Lepro, X.; Ovalle-Robles, R.; Baughman, R. H.; Kang, K. *Energ Environ Sci* **2013**, *6*, 3570.

(42) Wang, L. X.; Ara, M.; Wadumesthrige, K.; Salley, S.; Ng, K. Y. S. *J Power Sources* **2013**, *234*, 8.

(43) Lu, Y. C.; Gasteiger, H. A.; Parent, M. C.; Chiloyan, V.; Shao-Horn, Y. *Electrochem Solid St* **2010**, *13*, A69.

(44) Lee, S.; Zhu, S. L.; Milleville, C. C.; Lee, C. Y.; Chen, P. W.; Takeuchi, K. J.; Takeuchi, E. S.; Marschilok, A. C. *Electrochem Solid St* **2010**, *13*, A162.

(45) Marschilok, A. C.; Zhu, S. L.; Milleville, C. C.; Lee, S. H.; Takeuchi, E. S.; Takeuchi, K. J. *J Electrochem Soc* **2011**, *158*, A223.

(46) Sun, B.; Huang, X. D.; Chen, S. Q.; Munroe, P.; Wang, G. X. *Nano Lett* **2014**, *14*, 3145.

(47) Jung, H. G.; Jeong, Y. S.; Park, J. B.; Sun, Y. K.; Scrosati, B.; Lee, Y. J. *Acs Nano* **2013**, *7*, 3532.

(48) Li, F. J.; Tang, D. M.; Jian, Z. L.; Liu, D. Q.; Golberg, D.; Yamada, A.; Zhou, H. S. *Adv Mater* **2014**, *26*, 4659.

(49) Huang, K.; Li, Y. F.; Xing, Y. C. *Electrochim Acta* **2013**, *103*, 44.

(50) Wang, C.; Markovic, N. M.; Stamenkovic, V. R. *Acs Catal* **2012**, *2*, 891.

(51) Ko, B. K.; Kim, M. K.; Kim, S. H.; Lee, M. A.; Shim, S. E.; Baeck, S. H. *J Mol Catal a-Chem* **2013**, *379*, 9.

(52) Zhang, J. Q.; Chen, G. L.; An, M. Z.; Wang, P. *Int J Electrochem Sc* **2012**, *7*, 11957.

(53) Lu, Y. C.; Xu, Z. C.; Gasteiger, H. A.; Chen, S.; Hamad-Schifferli, K.; Shao-Horn, Y. *J Am Chem Soc* **2010**, *132*, 12170.

(54) Yin, J.; Fang, B.; Luo, J.; Wanjala, B.; Mott, D.; Loukrakpam, R.; Ng, M. S.; Li, Z.; Hong, J.; Whittingham, M. S.; Zhong, C. J. *Nanotechnology* **2012**, *23*.

(55) Zhang, J. Q.; Li, D.; Zhu, Y. M.; Chen, M. M.; An, M. Z.; Yang, P. X.; Wang, P. *Electrochim Acta* **2015**, *151*, 415.

(56) Yang, Y.; Liu, W.; Wang, Y. M.; Wang, X. C.; Xiao, L.; Lu, J. T.; Zhuang, L. *Phys Chem Chem Phys* **2014**, *16*, 20618.

(57) Kim, H.; Lim, H. D.; Kim, J.; Kang, K. *J Mater Chem A* **2014**, *2*, 33.

(58) Terashima, C.; Iwai, Y.; Cho, S. P.; Ueno, T.; Zettsu, N.; Saito, N.; Takai, O. *Int J Electrochem Sc* **2013**, *8*, 5407.

(59) Thapa, A. K.; Shin, T. H.; Ida, S.; Sumanasekera, G. U.; Sunkara, M. K.; Ishihara, T. *J Power Sources* **2012**, *220*, 211.

(60) Lei, Y.; Lu, J.; Luo, X. Y.; Wu, T. P.; Du, P.; Zhang, X. Y.; Ren, Y.; Wen, J. G.; Miller, D. J.; Miller, J. T.; Sun, Y. K.; Elam, J. W.; Amine, K. *Nano Lett* **2013**, *13*, 4182.

(61) Safari, M.; Adams, B. D.; Nazar, L. F. *J Phys Chem Lett* **2014**, *5*, 3486.

(62) Bhatt, M. D.; Geaney, H.; Nolan, M.; O'Dwyer, C. *Phys Chem Chem Phys* **2014**, *16*, 12093.

(63) Zhang, L. L.; Zhang, F. F.; Huang, G.; Wang, J. W.; Du, X. C.; Qin, L.; Wang, L. M. *J Power Sources* **2014**, *261*, 311.

(64) Liu, S. Y.; Zhu, Y. G.; Xie, J.; Huo, Y.; Yang, H. Y.; Zhu, T. J.; Cao, G. S.; Zhao, X. B.; Zhang, S. C. *Adv Energy Mater* **2014**, *4*.

(65) Kavakli, C.; Meini, S.; Harzer, G.; Tsiouvaras, N.; Piana, M.; Siebel, A.; Garsuch, A.; Gasteiger, H. A.; Herranz, J. *Chemcatchem* **2013**, *5*, 3358.

(66) Yang, Y.; Shi, M.; Li, Y. S.; Fu, Z. W. *J Electrochem Soc* **2012**, *159*, A1917.

(67) Thapa, A. K.; Ishihara, T. *J Power Sources* **2011**, *196*, 7016.

(68) Thapa, A. K.; Hidaka, Y.; Hagiwara, H.; Ida, S.; Ishihara, T. *J Electrochem Soc* **2011**, *158*, A1483.

(69) Zahoor, A.; Jang, H. S.; Jeong, J. S.; Christy, M.; Hwang, Y. J.; Nahm, K. S. *Rsc Adv* **2014**, *4*, 8973.

(70) Hintennach, A.; Rosenberg, S. *Russ J Electrochem+* **2014**, *50*, 933.

(71) Choi, H. A.; Jang, H.; Hwang, H.; Choi, M.; Lim, D.; Shim, S. E.; Baeck, S. H. *Electron Mater Lett* **2014**, *10*, 957.

(72) Park, M. S.; Kim, J. H.; Kim, K. J.; Jeong, G.; Kim, Y. J. *J Nanosci Nanotechno* **2013**, *13*, 3611.

(73) Park, H. W.; Lee, D. U.; Nazar, L. F.; Chen, Z. W. *J Electrochem Soc* **2013**, *160*, A344.

(74) Kalubarme, R. S.; Ahn, C. H.; Park, C. J. *Scripta Mater* **2013**, *68*, 619.

(75) Zhang, L. L.; Wang, Z. L.; Xu, D.; Xu, J. J.; Zhang, X. B.; Wang, L. M. *Chinese Sci Bull* **2012**, *57*, 4210.

(76) Li, J. X.; Wang, N.; Zhao, Y.; Ding, Y. H.; Guan, L. H. *Electrochem Commun* **2011**, *13*, 698.

(77) Huang, Z.; Zhang, M.; Cheng, J. F.; Gong, Y. P.; Li, X.; Chi, B.; Pu, J.; Jian, L. *J Alloy Compd* **2015**, *626*, 173.

(78) Zhang, M.; Xu, Q.; Sang, L.; Ding, F.; Liu, X. J.; Jiao, L. F. *T Nonferr Metal Soc* **2014**, *24*, 164.

(79) Thapa, A. K.; Pandit, B.; Paudel, H. S.; Thapa, R.; Ida, S.; Jasinski, J. B.; Sumanasekera, G. U.; Ishihara, T. *Electrochim Acta* **2014**, *127*, 410.

(80) Jang, I. C.; Ida, S.; Ishihara, T. *Electrochemistry* **2014**, *82*, 267.

(81) Jung, K. N.; Riaz, A.; Lee, S. B.; Lim, T. H.; Park, S. J.; Song, R. H.; Yoon, S.; Shin, K. H.; Lee, J. W. *J Power Sources* **2013**, *244*, 328.

(82) Thapa, A. K.; Saimen, K.; Ishihara, T. *Electrochem Solid St* **2010**, *13*, A165.

(83) Zhang, J. K.; Li, P. F.; Wang, Z. H.; Qiao, J. S.; Rooney, D.; Sun, W.; Sun, K. N. *J Mater Chem A* **2015**, *3*, 1504.

(84) Zhao, G. Y.; Lv, J. X.; Xu, Z. M.; Zhang, L.; Sun, K. N. *J Power Sources* **2014**, *248*, 1270.

(85) Zeng, J.; Francia, C.; Amici, J.; Bodoardo, S.; Penazzi, N. *J Power Sources* **2014**, *272*, 1003.

(86) Liu, Q. C.; Xu, J. J.; Chang, Z. W.; Zhang, X. B. *J Mater Chem A* **2014**, *2*, 6081.

(87) Zhao, G. Y.; Xu, Z. M.; Sun, K. N. *J Mater Chem A* **2013**, *1*, 12862.

(88) Yoon, T. H.; Park, Y. J. *J Power Sources* **2013**, *244*, 344.

(89) Yang, W.; Salim, J.; Ma, C.; Ma, Z. H.; Sun, C. W.; Li, J. Q.; Chen, L. Q.; Kim, Y. *Electrochem Commun* **2013**, *28*, 13.

(90) Park, C. S.; Kim, K. S.; Park, Y. J. *J Power Sources* **2013**, *244*, 72.

(91) Park, C. S.; Kim, J. H.; Park, Y. J. *J Electroceram* **2013**, *31*, 224.

(92) Lim, H. D.; Gwon, H.; Kim, H.; Kim, S. W.; Yoon, T.; Choi, J. W.; Oh, S. M.; Kang, K. *Electrochim Acta* **2013**, *90*, 63.

(93) Yoon, T. H.; Park, Y. J. *Nanoscale Res Lett* **2012**, *7*, 1.

(94) Ishihara, T.; Thapa, A. K.; Hidaka, Y.; Ida, S. *Electrochemistry* **2012**, *80*, 731.

(95) Cui, Y. M.; Wen, Z. Y.; Sun, S. J.; Lu, Y.; Jin, J. *Solid State Ionics* **2012**, *225*, 598.

(96) Sun, B.; Liu, H.; Munroe, P.; Ahn, H.; Wang, G. X. *Nano Res* **2012**, *5*, 460.

(97) Lu, J.; Qin, Y.; Du, P.; Luo, X. Y.; Wu, T. P.; Ren, Y.; Wen, J. G.; Miller, D. J.; Miller, J. T.; Amine, K. *Rsc Adv* **2013**, *3*, 8276.

(98) Zhang, W. Y.; Zeng, Y.; Xu, C.; Tan, H. T.; Liu, W. L.; Zhu, J. X.; Xiao, N.; Hng, H. H.; Ma, J.; Hoster, H. E.; Yazami, R.; Yan, Q. Y. *Rsc Adv* **2012**, *2*, 8508.

(99) Lim, S. H.; Kim, D. H.; Byun, J. Y.; Kim, B. K.; Yoon, W. Y. *Electrochim Acta* **2013**, *107*, 681.

(100) Lim, S. H.; Kim, B. K.; Yoon, W. Y. *J Appl Electrochem* **2012**, *42*, 1045.

(101) Jian, Z. L.; Liu, P.; Li, F. J.; He, P.; Guo, X. W.; Chen, M. W.; Zhou, H. S. *Angew Chem Int Edit* **2014**, *53*, 442.

(102) Yilmaz, E.; Yogi, C.; Yamanaka, K.; Ohta, T.; Byon, H. R. *Nano Lett* **2013**, *13*, 4679.

(103) Zhao, G. Y.; Niu, Y. N.; Zhang, L.; Sun, K. N. *J Power Sources* **2014**, *270*, 386.

(104) Lin, X. J.; Zhou, L.; Huang, T.; Yu, A. S. *Int J Electrochem Sc* **2012**, *7*, 9550.

(105) Xu, J. J.; Xu, D.; Wang, Z. L.; Wang, H. G.; Zhang, L. L.; Zhang, X. B. *Angew Chem Int Edit* **2013**, *52*, 3887.

(106) Yang, W.; Salim, J.; Li, S. A.; Sun, C. W.; Chen, L. Q.; Goodenough, J. B.; Kim, Y. *J Mater Chem* **2012**, *22*, 18902.

(107) Song, M.; Zhu, D.; Zhang, L.; Wang, X. F.; Mi, R.; Liu, H.; Mei, J.; Lau, L. W. M.; Chen, Y. G. *J Solid State Electr* **2014**, *18*, 739.

(108) Shui, J. L.; Du, F.; Xue, C. M.; Li, Q.; Dai, L. M. *Acs Nano* **2014**, *8*, 3015.

(109) Sun, N.; Liu, H. X.; Yu, Z. Y.; Zheng, Z. N.; Shao, C. Y. *Solid State Ionics* **2014**, *268*, 125.

(110) Ma, Z.; Yuan, X. X.; Li, L.; Ma, Z. F. *Chem Commun* **2014**, *50*, 14855.

(111) Jin, C.; Yang, Z. B.; Cao, X. C.; Lu, F. L.; Yang, R. Z. *Int J Hydrogen Energ* **2014**, *39*, 2526.

(112) Du, Z. Z.; Yang, P.; Wang, L.; Lu, Y. H.; Goodenough, J. B.; Zhang, J.; Zhang, D. W. *J Power Sources* **2014**, *265*, 91.

(113) Zhang, J.; Wang, L. J.; Xu, L. L.; Ge, X. M.; Zhao, X.; Lai, M.; Liu, Z. L.; Chen, W. *Nanoscale* **2015**, *7*, 720.

(114) Xu, Y. J.; Bian, W. Y.; Wu, J.; Tian, J. H.; Yang, R. Z. *Electrochim Acta* **2015**, *151*, 276.

(115) Li, Y.; Zou, L. L.; Li, J.; Guo, K.; Dong, X. W.; Li, X. W.; Xue, X. Z.; Zhang, H. F.; Yang, H. *Electrochim Acta* **2014**, *129*, 14.

(116) Jadhav, H. S.; Kalubarme, R. S.; Roh, J. W.; Jung, K. N.; Shin, K. H.; Park, C. N.; Park, C. J. *J Electrochem Soc* **2014**, *161*, A2188.

(117) Zhang, L. X.; Zhang, S. L.; Zhang, K. J.; Xu, G. J.; He, X.; Dong, S. M.; Liu, Z. H.; Huang, C. S.; Gu, L.; Cui, G. L. *Chem Commun* **2013**, *49*, 3540.

(118) Sun, B.; Zhang, J. Q.; Munroe, P.; Ahn, H. J.; Wang, G. *Electrochem Commun* **2013**, *31*, 88.

(119) Li, Y.; Guo, K.; Li, J.; Dong, X. W.; Yuan, T.; Li, X. W.; Yang, H. *Acs Appl Mater Inter* **2014**, *6*, 20949.

(120) Minowa, H.; Hayashi, M.; Hayashi, K.; Kobayashi, R.; Takahashi, K. *J Power Sources* **2013**, *244*, 17.

(121) Oh, S. H.; Black, R.; Pomerantseva, E.; Lee, J. H.; Nazar, L. F. *Nat Chem* **2012**, *4*, 1004.

(122) Jung, K. N.; Jung, J. H.; Im, W. B.; Yoon, S.; Shin, K. H.; Lee, J. W. *Acs Appl Mater Inter* **2013**, *5*, 9902.

(123) Jung, K. N.; Lee, J. I.; Im, W. B.; Yoon, S.; Shin, K. H.; Lee, J. W. *Chem Commun* **2012**, *48*, 9406.

(124) Zhu, Z.; Kushima, A.; Yin, Z.; Qi, L.; Amine, K.; Lu, J.; Li, J. **2016**, *1*, 16111.

(125) Nørskov, J. K.; Rossmeisl, J.; Logadottir, A.; Lindqvist, L.; Kitchin, J. R.; Bligaard, T.; Jónsson, H. *The Journal of Physical Chemistry B* **2004**, *108*, 17886.

(126) Shao, M.; Peles, A.; Shoemaker, K. *Nano Lett* **2011**, *11*, 3714.

(127) Chen, J.; Lim, B.; Lee, E. P.; Xia, Y. *Nano Today* **2009**, *4*, 81.

(128) Choi, C. H.; Kim, M.; Kwon, H. C.; Cho, S. J.; Yun, S.; Kim, H.-T.; Mayrhofer, K. J. J.; Kim, H.; Choi, M. **2016**, *7*, 10922.

(129) Deshpande, S.; Kitchin, J. R.; Viswanathan, V. *Acs Catal* **2016**, *6*, 5251.

(130) Yue, J.; Du, Z.; Shao, M. *The Journal of Physical Chemistry Letters* **2015**, *6*, 3346.

(131) Yano, H.; Kataoka, M.; Yamashita, H.; Uchida, H.; Watanabe, M. *Langmuir* **2007**, *23*, 6438.

(132) Wang, W.; Wang, Z.; Yang, M.; Zhong, C.-J.; Liu, C.-J. *Nano Energy* **2016**, *25*, 26.

(133) Nesselberger, M.; Ashton, S.; Meier, J. C.; Katsounaros, I.; Mayrhofer, K. J. J.; Arenz, M. *J Am Chem Soc* **2011**, *133*, 17428.

(134) Stamenkovic, V. R.; Mun, B. S.; Arenz, M.; Mayrhofer, K. J. J.; Lucas, C. A.; Wang, G.; Ross, P. N.; Markovic, N. M. *Nat Mater* **2007**, *6*, 241.

(135) Escudero-Escribano, M.; Malacrida, P.; Hansen, M. H.; Vej-Hansen, U. G.; Velázquez-Palenzuela, A.; Tripkovic, V.; Schiøtz, J.; Rossmeisl, J.; Stephens, I. E. L.; Chorkendorff, I. *Science* **2016**, *352*, 73.

(136) Gong, K.; Du, F.; Xia, Z.; Durstock, M.; Dai, L. *Science* **2009**, *323*, 760.

(137) Yang, L.; Jiang, S.; Zhao, Y.; Zhu, L.; Chen, S.; Wang, X.; Wu, Q.; Ma, J.; Ma, Y.; Hu, Z. *Angewandte Chemie International Edition* **2011**, *50*, 7132.

(138) Liu, Z.-W.; Peng, F.; Wang, H.-J.; Yu, H.; Zheng, W.-X.; Yang, J. *Angewandte Chemie International Edition* **2011**, *50*, 3257.

(139) Zhao, Y.; Yang, L.; Chen, S.; Wang, X.; Ma, Y.; Wu, Q.; Jiang, Y.; Qian, W.; Hu, Z. *J Am Chem Soc* **2013**, *135*, 1201.

(140) Shi, Q.; Peng, F.; Liao, S.; Wang, H.; Yu, H.; Liu, Z.; Zhang, B.; Su, D. *J Mater Chem A* **2013**, *1*, 14853.

(141) Shui, J.; Wang, M.; Du, F.; Dai, L. *Science Advances* **2015**, *1*.

(142) Liu, X.; Dai, L. **2016**, *1*, 16064.

(143) Osgood, H.; Devaguptapu, S. V.; Xu, H.; Cho, J.; Wu, G. *Nano Today* **2016**, *11*, 601.

(144) Chen, D.; Chen, C.; Baiyee, Z. M.; Shao, Z.; Ciucci, F. *Chem Rev* **2015**, *115*, 9869.

(145) Xiao, J.; Kuang, Q.; Yang, S.; Xiao, F.; Wang, S.; Guo, L. *Sci Rep-Uk* **2013**, *3*, 2300.

(146) Liang, Y. Y.; Li, Y. G.; Wang, H. L.; Zhou, J. G.; Wang, J.; Regier, T.; Dai, H. J. *Nat Mater* **2011**, *10*, 780.

(147) Stoerzinger, K. A.; Risch, M.; Han, B. H.; Shao-Horn, Y. *Acs Catal* **2015**, *5*, 6021.

(148) Emsley, J. *Nature's building blocks: an AZ guide to the elements*; Oxford University Press, 2011.

(149) Gorlin, Y.; Jaramillo, T. F. *J Am Chem Soc* **2010**, *132*, 13612.

(150) Ng, J. W. D.; Tang, M.; Jaramillo, T. F. *Energ Environ Sci* **2014**, *7*, 2017.

(151) Mao, L.; Zhang, D.; Sotomura, T.; Nakatsu, K.; Koshiba, N.; Ohsaka, T. *Electrochim Acta* **2003**, *48*, 1015.

(152) Ramadass, N. *Materials Science and Engineering* **1978**, *36*, 231.

(153) Risch, M. *Catalysts* **2017**, *7*, 154.

(154) Wei, X.; Hug, P.; Figi, R.; Trottmann, M.; Weidenkaff, A.; Ferri, D. *Applied Catalysis B: Environmental* **2010**, *94*, 27.

(155) Chen, C.-Q.; Li, W.; Cao, C.-Y.; Song, W.-G. *J Mater Chem* **2010**, *20*, 6968.

(156) Hardin, W. G.; Slanac, D. A.; Wang, X.; Dai, S.; Johnston, K. P.; Stevenson, K. J. *The Journal of Physical Chemistry Letters* **2013**, *4*, 1254.

(157) Ngamou, P. H. T.; Bahlawane, N. *Chem Mater* **2010**, *22*, 4158.

(158) Natile, M. M.; Ugel, E.; Maccato, C.; Glisenti, A. *Applied Catalysis B: Environmental* **2007**, *72*, 351.

(159) Mathur, A.; Kushwaha, H. S.; Vaish, R.; Halder, A. *Rsc Adv* **2016**, *6*, 94826.

(160) Han, B. H.; Stoerzinger, K. A.; Tileli, V.; Gamalski, A. D.; Stach, E. A.; Shao-Horn, Y. *Nature Materials* **2017**, *16*, 121.

(161) Sunarso, J.; Torriero, A. A. J.; Zhou, W.; Howlett, P. C.; Forsyth, M. *J Phys Chem C* **2012**, *116*, 5827.

(162) Ge, X. M.; Li, B.; Wuu, D.; Sumboja, A.; An, T.; Hor, T. S. A.; Zong, Y.; Liu, Z. L. *J Mol Eng Mater* **2015**, *3*.

(163) Jin, C.; Cao, X. C.; Lu, F. L.; Yang, Z. R.; Yang, R. Z. *Int J Hydrogen Energ* **2013**, *38*, 10389.

(164) Yuan, X. Z.; Qu, W.; Fahlman, J.; Ivey, D. G.; Zhang, X. *Energy Technology/Battery (General) - 223rd Ecs Meeting* **2013**, *53*, 265.

(165) Hayashi, M.; Hyodo, T.; Miura, N.; Yamazoe, N. *Electrochemistry* **2000**, *68*, 112.

(166) Celorrio, V.; Dann, E.; Calvillo, L.; Morgan, D. J.; Hall, S. R.; Fermin, D. J. *Chemelectrochem* **2016**, *3*, 283.

(167) Christ, J. M.; Ngo, C.; Batson, T.; Cadigan, C. A.; Tong, J. H.; Richards, R. M.; O'Hayre, R.; Pylypenko, S. *Catal Sci Technol* **2016**, *6*, 7744.

(168) Fabbri, E.; Nachtegaal, M.; Cheng, X.; Schmidt, T. J. *Adv Energy Mater* **2015**, *5*.

(169) Fabbri, E.; Mohamed, R.; Levecque, P.; Conrad, O.; Kotz, R.; Schmidt, T. J. *Acs Catal* **2014**, *4*, 1061.

(170) Vignesh, A.; Prabu, M.; Shanmugam, S. *Acs Appl Mater Inter* **2016**, *8*, 6019.

(171) Suntivich, J.; Gasteiger, H. A.; Yabuuchi, N.; Nakanishi, H.; Goodenough, J. B.; Shao-Horn, Y. *Nature Chemistry* **2011**, *3*, 546.

(172) Sunarso, J.; Torriero, A. A. J.; Zhou, W.; Howlett, P. C.; Forsyth, M. *J Phys Chem C* **2012**, *116*, 26108.

(173) Celorrio, V.; Dann, E.; Calvillo, L.; Morgan, D. J.; Hall, S. R.; Fermin, D. J. *Chemelectrochem* **2016**, *3*, 283.

(174) Hyodo, T.; Hayashi, M.; Mitsutake, S.; Miura, N.; Yamazoe, N. *Praseodymium–calcium manganites (Pr1−xCaxMnO3) as electrode catalyst for oxygen reduction in alkaline solution*, 1997; Vol. 27.

(175) Celorrio, V.; Calvillo, L.; Dann, E.; Granozzi, G.; Aguadero, A.; Kramer, D.; Russell, A. E.; Fermin, D. J. *Catal Sci Technol* **2016**, *6*, 7231.

(176) Stoerzinger, K. A.; Lü, W.; Li, C.; Ariando; Venkatesan, T.; Shao-Horn, Y. *The Journal of Physical Chemistry Letters* **2015**, *6*, 1435.

(177) Mehta, A.; Heaney, P. J. *Phys Rev B* **1994**, *49*, 563.

(178) Ye, N.; Hertz, J. L. *Acta Mater* **2014**, *63*, 123.

(179) Ma, X. F.; Carneiro, J. S. A.; Gu, X. K.; Qin, H.; Xin, H. L.; Sun, K.; Nikolla, E. *Acs Catalysis* **2015**, *5*, 4013.

(180) Carneiro, J. S. A.; Brocca, R. A.; Lucena, M. L. R. S.; Nikolla, E. *Appl Catal B-Environ* **2017**, *200*, 106.

(181) Paulus, W.; Cousson, A.; Dhalenne, G.; Berthon, J.; Revcolevschi, A.; Hosoya, S.; Treutmann, W.; Heger, G.; Le Toquin, R. *Solid State Sci* **2002**, *4*, 565.

(182) Naumovich, E. N.; Kharton, V. V. *Journal of Molecular Structure: THEOCHEM* **2010**, *946*, 57.

(183) Read, M. S. D.; Islam, M. S.; King, F.; Hancock, F. E. *The Journal of Physical Chemistry B* **1999**, *103*, 1558.

(184) Yakal-Kremski, K.; Mogni, L. V.; Montenegro-Hernandez, A.; Caneiro, A.; Barnett, S. A. *J Electrochem Soc* **2014**, *161*, F1366.

(185) Boehm, E.; Bassat, J. M.; Dordor, P.; Mauvy, F.; Grenier, J. C.; Stevens, P. *Solid State Ionics* **2005**, *176*, 2717.

(186) Boehm, E.; Bassat, J. M.; Dordor, P.; Mauvy, F.; Grenier, J. C.; Stevens, P. *Solid State Ionics* **2005**, *176*, 2717.

(187) Egger, A.; Bucher, E.; Sitte, W. *J Electrochem Soc* **2011**, *158*, B573.

(188) Takeda, Y.; Kanno, R.; Sakano, M.; Yamamoto, O.; Takano, M.; Bando, Y.; Akinaga, H.; Takita, K.; Goodenough, J. B. *Mater Res Bull* **1990**, *25*, 293.

(189) Alonso, J. A.; Amador, J.; Gutiérrez-Puebla, E.; Monge, M. A.; Rasines, I.; Ruíz-Valero, C.; Campá, J. A. *Solid State Communications* **1990**, *76*, 1327.

(190) Shi, C.-Y.; Hu, Z.-B.; Hao, Y.-M. *J Alloy Compd* **2011**, *509*, 1333.

(191) Das, A.; Xhafa, E.; Nikolla, E. *Catal Today* **2016**, *277*, 214.

(192) Mauvy, F.; Boehm, E.; Bassat, J. M.; Grenier, J. C.; Fouletier, J. *Solid State Ionics* **2007**, *178*, 1200.

(193) Munnings, C. N.; Skinner, S. J.; Amow, G.; Whitfield, P. S.; Davidson, I. J. *Solid State Ionics* **2005**, *176*, 1895.

(194) Kharton, V.; Yaremchenko, A.; Tsipis, E.; Valente, A.; Patrakeev, M.; Shaula, A.; Frade, J.; Rocha, J. *Applied Catalysis A: General* **2004**, *261*, 25.

(195) Gu, X.-K.; Nikolla, E. *Acs Catal* **2017**, *7*, 5912.

(196) Tarancon, A.; Burriel, M.; Santiso, J.; Skinner, S. J.; Kilner, J. A. *J Mater Chem* **2010**, *20*, 3799.

(197) Adler, S. B. *Solid State Ionics* **1998**, *111*, 125.

(198) Adler, S. B.; Lane, J.; Steele, B. *J Electrochem Soc* **1996**, *143*, 3554.

(199) Shojaei, S.; Hassanzadeh-Tabrizi, S. A.; Ghashang, M. *Ceram Int* **2014**, *40*, 9609.

(200) Malik, M. A.; Wani, M. Y.; Hashim, M. A. *Arab J Chem* **2012**, *5*, 397.

(201) Aurbach, D.; McCloskey, B. D.; Nazar, L. F.; Bruce, P. G. **2016**, *1*, 16128.

(202) Hojberg, J.; McCloskey, B. D.; Hjelm, J.; Vegge, T.; Johansen, K.; Norby, P.; Luntz, A. C. *Acs Appl Mater Inter* **2015**, *7*, 4039.

(203) Beattie, S. D.; Manolescu, D. M.; Blair, S. L. *J Electrochem Soc* **2009**, *156*, A44.

(204) Shinozaki, K.; Zack, J. W.; Pylypenko, S.; Pivovar, B. S.; Kocha, S. S. *J Electrochem Soc* **2015**, *162*, F1384.

(205) Yunker, P. J.; Still, T.; Lohr, M. A.; Yodh, A. G. *Nature* **2011**, *476*, 308.

(206) Perego, G. *Catal Today* **1998**, *41*, 251.

(207) Wikipedia contributors. "Rooney Rule." Wikipedia, T. F. E. W., The Free Encyclopedia, 7 Sep. 2016. Web. 7 Sep. 2016.

(208) Nikolla, E., University of Michigan, 2009.

(209) Zhang, X. F.; Zhang, Z. *Progress in Transmission Electron Microscopy 1: Concepts and Techniques*; Springer, 2001.

(210) Pennycook, S. J.; Nellist, P. D. *Scanning Transmission Electron Microscopy: Imaging and Analysis*; Springer New York, 2011.

(211) Keast, V. J.; Scott, A. J.; Brydson, R.; Williams, D. B.; Bruley, J. *J Microsc-Oxford* **2001**, *203*, 135.

(212) Lowell, S.; Shields, J. E.; Thomas, M. A.; Thommes, M. *Characterization of Porous Solids and Powders: Surface Area, Pore Size and Density*; Springer Netherlands, 2012.

(213) Shervedani, R. K.; Lasia, A. *J Electrochem Soc* **1998**, *145*, 2219.

(214) Black, R.; Adams, B.; Nazar, L. F. *Adv Energy Mater* **2012**, *2*, 801.

(215) Bruce, P. G.; Freunberger, S. A.; Hardwick, L. J.; Tarascon, J. M. *Nat Mater* **2012**, *11*, 19.

(216) Christensen, J.; Albertus, P.; Sanchez-Carrera, R. S.; Lohmann, T.; Kozinsky, B.; Liedtke, R.; Ahmed, J.; Kojic, A. *J Electrochem Soc* **2012**, *159*, R1.

(217) Rolison, D. R.; Nazar, L. F. *Mrs Bull* **2011**, *36*, 486.

(218) Kuboki, T.; Okuyama, T.; Ohsaki, T.; Takami, N. *J Power Sources* **2005**, *146*, 766.

(219) Read, J.; Mutolo, K.; Ervin, M.; Behl, W.; Wolfenstine, J.; Driedger, A.; Foster, D. *J Electrochem Soc* **2003**, *150*, A1351.

(220) Lu, Y. C.; Gallant, B. M.; Kwabi, D. G.; Harding, J. R.; Mitchell, R. R.; Whittingham, M. S.; Shao-Horn, Y. *Energ Environ Sci* **2013**, *6*, 750.

(221) Shao, Y. Y.; Park, S.; Xiao, J.; Zhang, J. G.; Wang, Y.; Liu, J. *Acs Catal* **2012**, *2*, 844.

(222) Sun, B.; Munroe, P.; Wang, G. X. *Sci Rep-Uk* **2013**, *3*.

(223) Zhu, C. Z.; Shi, Q. R.; Fu, S. F.; Song, J. H.; Xia, H. B.; Du, D.; Lin, Y. H. *Adv Mater* **2016**, *28*, 8779.

(224) Escudero-Escribano, M.; Malacrida, P.; Hansen, M. H.; Vej-Hansen, U. G.; Velazquez-Palenzuela, A.; Tripkovic, V.; Schiotz, J.; Rossmeisl, J.; Stephens, I. E. L.; Chorkendorff, I. *Science* **2016**, *352*, 73.

(225) Ogasawara, T.; Debart, A.; Holzapfel, M.; Novak, P.; Bruce, P. G. *J Am Chem Soc* **2006**, *128*, 1390.

(226) Lei, Y.; Lu, J.; Luo, X.; Wu, T.; Du, P.; Zhang, X.; Ren, Y.; Wen, J.; Miller, D. J.; Miller, J. T.; Sun, Y. K.; Elam, J. W.; Amine, K. *Nano Lett* **2013**, *13*, 4182.

(227) Meng, T. J.; Ara, M.; Wang, L. X.; Naik, R.; Ng, K. Y. S. *J Mater Sci* **2014**, *49*, 4058.

(228) Minowa, H.; Hayashi, M.; Takahashi, M.; Shodai, T. *Electrochemistry* **2010**, *78*, 353.

(229) Zhao, Y. L.; Xu, L.; Mai, L. Q.; Han, C. H.; An, Q. Y.; Xu, X.; Liu, X.; Zhang, Q. J. *P Natl Acad Sci USA* **2012**, *109*, 19569.

(230) Zhang, G. Q.; Hendrickson, M.; Plichta, E. J.; Au, M.; Zheng, J. P. *J Electrochem Soc* **2012**, *159*, A310.

(231) Jung, K. N.; Jung, J. H.; Im, W. B.; Yoon, S.; Shin, K. H.; Lee, J. W. *ACS Appl Mater Interfaces* **2013**, *5*, 9902.

(232) Skinner, S. J.; Kilner, J. A. *Solid State Ionics* **2000**, *135*, 709.

(233) Ma, X.; Wang, B.; Xhafa, E.; Sun, K.; Nikolla, E. *Chemical Communications* **2015**, *51*, 137.

(234) Nacy, A.; Ma, X. F.; Nikolla, E. *Topics in Catalysis* **2015**, *58*, 513.

(235) Jung, H. G.; Hassoun, J.; Park, J. B.; Sun, Y. K.; Scrosati, B. *Nat Chem* **2012**, *4*, 579.

(236) Laberty, C.; Zhao, F.; Swider-Lyons, K. E.; Virkar, A. V. *Electrochemical and Solid-State Letters* **2007**, *10*, B170.

(237) Schuler, J. A.; Lubbe, H.; Hessler-Wyser, A.; Van Herle, J. *J Power Sources* **2012**, *213*, 223.

(238) Alqurashi, G. K.; Al-Shehri, A.; Narasimharao, K. *Rsc Adv* **2016**, *6*, 71076.

(239) Chen, L.; Huang, R.; Ma, Y. J.; Luo, S. L.; Au, C. T.; Yin, S. F. *Rsc Adv* **2013**, *3*, 24354.

(240) Deka, P.; Hazarika, A.; Deka, R. C.; Bharali, P. *Rsc Adv* **2016**, *6*, 95292.

(241) Li, J. M.; Qu, Z. P.; Qin, Y.; Wang, H. *Appl Surf Sci* **2016**, *385*, 234.

(242) Jia, J. B.; Zhang, P. Y.; Chen, L. *Catal Sci Technol* **2016**, *6*, 5841.

(243) Lu, F. L.; Sui, J.; Su, J. M.; Jin, C.; Shen, M.; Yang, R. Z. *J Power Sources* **2014**, *271*, 55.

(244) Ma, X.; Wang, B.; Xhafa, E.; Sun, K.; Nikolla, E. *Chem Commun* **2015**, *51*, 137.

(245) Read, M. S. D.; Islam, M. S.; Watson, G. W.; Hancock, F. E. *J Mater Chem* **2001**, *11*, 2597.

(246) Castro, M.; Burriel, R. *Thermochim Acta* **1995**, *269–270*, 537.

(247) Čebašek, N.; Haugsrud, R.; Norby, T. *Solid State Ionics* **2013**, *231*, 74.

(248) Hu, Y. X.; Han, X. P.; Cheng, F. Y.; Zhao, Q.; Hu, Z.; Chen, J. *Nanoscale* **2014**, *6*, 177.

(249) Younesi, R.; Hahlin, M.; Bjorefors, F.; Johansson, P.; Edstrom, K. *Chem Mater* **2013**, *25*, 77.

(250) Gray, H. B. *Nat Chem* **2009**, *1*, 7.

(251) Denholm, P.; Ela, E.; Kirby, B.; Milligan, M. *The Role of Energy Storage with Renewable Electricity Generation* **2010**.

(252) Whitesides, G. M.; Crabtree, G. W. *Science* **2007**, *315*, 796.

(253) Winter, M.; Brodd, R. J. *Chem Rev* **2004**, *104*, 4245.

(254) Lin, Z. Y.; Waller, G.; Liu, Y.; Liu, M. L.; Wong, C. P. *Adv Energy Mater* **2012**, *2*, 884.

(255) Liang, Y. Y.; Wang, H. L.; Zhou, J. G.; Li, Y. G.; Wang, J.; Regier, T.; Dai, H. J. *J Am Chem Soc* **2012**, *134*, 3517.

(256) Rios, E.; Gautier, J. L.; Poillerat, G.; Chartier, P. *Electrochim Acta* **1998**, *44*, 1491.

(257) Stoerzinger, K. A.; Risch, M.; Suntivich, J.; Lu, W. M.; Zhou, J.; Biegalski, M. D.; Christen, H. M.; Ariando; Venkatesan, T.; Shao-Horn, Y. *Energ Environ Sci* **2013**, *6*, 1582.

(258) Gorlin, Y.; Chung, C. J.; Nordlund, D.; Clemens, B. M.; Jaramillo, T. F. *Acs Catal* **2012**, *2*, 2687.

(259) Suntivich, J.; May, K. J.; Gasteiger, H. A.; Goodenough, J. B.; Shao-Horn, Y. *Science* **2011**, *334*, 1383.

(260) Crumlin, E. J.; Ahn, S. J.; Lee, D.; Mutoro, E.; Biegalski, M. D.; Christen, H. M.; Shao-Horn, Y. *J Electrochem Soc* **2012**, *159*, F219.

(261) Crumlin, E. J.; Mutoro, E.; Hong, W. T.; Biegalski, M. D.; Christen, H. M.; Liu, Z.; Bluhm, H.; Shao-Horn, Y. *J Phys Chem C* **2013**, *117*, 16087.

(262) Feng, Z. X.; Crumlin, E. J.; Hong, W. T.; Lee, D.; Mutoro, E.; Biegalski, M. D.; Zhou, H.; Bluhm, H.; Christen, H. M.; Shao-Horn, Y. *J Phys Chem Lett* **2013**, *4*, 1512.

(263) Han, B. H.; Risch, M.; Lee, Y. L.; Ling, C.; Jia, H. F.; Shao-Horn, Y. *Phys Chem Chem Phys* **2015**, *17*, 22576.

(264) Jung, J. I.; Risch, M.; Park, S.; Kim, M. G.; Nam, G.; Jeong, H. Y.; Shao-Horn, Y.; Cho, J. *Energ Environ Sci* **2016**, *9*, 176.

(265) la O', G. J.; Ahn, S. J.; Crumlin, E.; Orikasa, Y.; Biegalski, M. D.; Christen, H. M.; Shao-Horn, Y. *Angew Chem Int Edit* **2010**, *49*, 5344.

(266) la O', G. J.; Shao-Horn, Y. *Electrochem Solid St* **2009**, *12*, B82.

(267) May, K. J.; Carlton, C. E.; Stoerzinger, K. A.; Risch, M.; Suntivich, J.; Lee, Y. L.; Grimaud, A.; Shao-Horn, Y. *J Phys Chem Lett* **2012**, *3*, 3264.

(268) Mutoro, E.; Crumlin, E. J.; Biegalski, M. D.; Christen, H. M.; Shao-Horn, Y. *Energ Environ Sci* **2011**, *4*, 3689.

(269) Scholz, J.; Risch, M.; Stoerzinger, K. A.; Wartner, G.; Shao-Horn, Y.; Jooss, C. *Journal of Physical Chemistry C* **2016**, *120*, 27746.

(270) Yu, J.; Sunarso, J.; Zhu, Y. L.; Xu, X. M.; Ran, R.; Zhou, W.; Shao, Z. P. *Chem-Eur J* **2016**, *22*, 2719.

(271) Vashook, V. V.; Trofimenko, N. E.; Ullmann, H.; Makhnach, L. V. *Solid State Ionics* **2000**, *131*, 329.

(272) Read, M. S. D.; Islam, M. S.; King, F.; Hancock, F. E. *Journal of Physical Chemistry B* **1999**, *103*, 1558.

(273) Ramaswamy, N.; Mukerjee, S. *Advances in Physical Chemistry* **2012**, *2012*, 1.

(274) Mayrhofer, K. J. J.; Crampton, A. S.; Wiberg, G. K. H.; Arenz, M. *J Electrochem Soc* **2008**, *155*, P78.

(275) Srejic, I.; Rakocevic, Z.; Nenadovic, M.; Strbac, S. *Electrochim Acta* **2015**, *169*, 22.

(276) Karppinen, M.; Fukuoka, A.; Niinisto, L.; Yamauchi, H. *Supercond Sci Tech* **1996**, *9*, 121.

(277) Borlera, M. L.; Abbattista, F. *J Less-Common Met* **1983**, *92*, 55.

(278) Wang, W. H.; Geng, J.; Kuai, L.; Li, M.; Geng, B. Y. *Chem-Eur J* **2016**, *22*, 9909.

(279) Huang, L. F.; Hutchison, M. J.; Santucci, R. J.; Scully, J. R.; Rondinelli, J. M. *J Phys Chem C* **2017**, *121*, 9782.

(280) Wroblowa, H. S.; Pan, Y. C.; Razumney, G. *J Electroanal Chem* **1976**, *69*, 195.

(281) *Energy Efficiency and Renewable Energy*, The US Department of Energy (DOE).

(282) Gallant, B. M.; Kwabi, D. G.; Mitchell, R. R.; Zhou, J. G.; Thompson, C. V.; Shao-Horn, Y. *Energ Environ Sci* **2013**, *6*, 2518.

(283) Nagasubramanian, G.; Attia, A. I.; Halpert, G. *J Electrochem Soc* **1992**, *139*, 3043.

ABSTRACT

FUNDAMENTAL INVESTIGATION OF THE ELECTROCATALYTIC ACTIVITY OF LAYERED MIXED METAL OXIDES FOR LOW TEMPERATURE OXYGEN ELECTROCATALYSIS

by

AYAD M. NACY

December 2017

Advisor: Dr. Eranda Nikolla

Major: Chemical Engineering

Degree: Doctor of Philosophy

Li–O_2 (Li–air) batteries are among the most promising energy storage technologies due to their high theoretical specific capacity and energy density. Key challenges with this technology include high overpotential losses associated with catalyzing the electrochemical reactions (i.e., oxygen reduction and evolution reactions) at the cathode of the battery. One way to address this challenge is to incorporate an active electrocatalyst, such as first-order Ruddlesden-Popper series of layered oxides. We show that the composition of the A-site in first-order Ruddlesden-Popper series of layered oxides (A_2BO_4) has a significant effect in the electrochemical activity of Li-O_2 cathodes. Among the oxides composed of lanthanides (La, Pr, Nd) that form stable structures, La_2NiO_4 exhibits the best electrochemical performance when incorporated in Li-O_2 cathodes. Furthermore, we find that the electrochemical performance of La_2NiO_4 could be further improved by doping the La site with an alkaline earth metal, such as Ba. We show that $Ba_{0.25}La_{1.75}NiO_4$ exhibits the best discharge capacity and lowest OER potential when compared to undoped La_2NiO_4, $Sr_{0.25}La_{1.75}NiO_4$ and $Ca_{0.25}La_{1.75}NiO_4$. Stability of these oxide electrocatalysts is demonstrated under electrochemical conditions. We anticipate that these findings will further

enhance the driving force for utilizing first-order Ruddlesden-Popper series of layered oxides as efficient non-precious metal-based cathode electrocatalysts for high-energy storage systems.

In the second portion of this study, we report through the example of $La_2NiO_{4+\delta}$ that layered nickelate oxide materials with rod-shaped nanostructure exhibit promising electrochemical performance as cathode electrocatalysts for Li–O_2 batteries. We demonstrate the ability to control the nanostructure of $La_2NiO_{4+\delta}$ electrocatalyst at the nanoscale level using a reverse-microemulsion synthesis approach. We show that Li–O_2 batteries with cathodes containing rod-shaped $La_2NiO_{4+\delta}$ electrocatalyst exhibit lower charging potentials and higher reversible capacities when compared to batteries with carbon-only cathodes. Our studies indicate that the enhancement in the battery performance induced by the rod-shaped $La_2NiO_{4+\delta}$ electrocatalyst can be attributed to the fact that $La_2NiO_{4+\delta}$ nanorods (i) facilitate the formation of nanosized Li_2O_2 particles during discharge, and (ii) promote the electrocatalytic activity toward the oxygen evolution reaction during charging. These findings open up avenues for the utilization of (i) reverse-microemulsion method for controlling the nanostructure of layered oxide materials, and (ii) nanorod-structured nickelate oxides as efficient cathode electrocatalysts for Li–O_2 batteries.

In the third part of this thesis, we explore the potential of the aforementioned electrocatalysts as promising, non-precious metal based electrocatalysts for ORR in alkaline media. We systematically study the effect of the transition metal site composition using well-defined nanostructures of these oxides terminated by (001) surface facets. Using rotating ring disk electrode voltammetry studies, we show that doping the Ni site with Mn ($La_2Ni_{0.875}Mn_{0.125}O_{4+\delta}$) leads to the best ORR activity among all the oxide compositions considered. Detailed kinetic analyses demonstrate that nanostructured Mn-doped LNO also exhibits the highest selectivity toward the desired, direct 4e- pathway for ORR. Furthermore, stability tests via cyclic voltammetry

scans, show that Mn-LNO is stable over the course of cycling with minimal change in activity induced by degradation of the carbon support.

AUTOBIOGRAPHICAL STATEMENT

EDUCATION

M.S. Chemical Engineering, Wayne State University, December 2014

B.S. Chemical Engineering, University of Technology, June 2006

PUBLICATIONS

1. **Ayad Nacy**, Xianfeng Ma, Eranda Nikolla. "Nanostructured Nickelate Oxides as Efficient and Stable Cathode Electrocatalysts for Li-O_2 Batteries", Topics in Catalysis 58 (2015) 513-521.
2. **Ayad Nacy**, Samji Samira, Suzana Meira, Mariana de Souza, Eranda Nikolla. "Layered, Nickelate Oxides as Cathode Electrocatalysts for Li-O_2: Effect of A-site composition on the electrocatalytic activity", to be submitted to Journal of Electrochemical Society.
3. **Ayad Nacy**, Xiangkui Gu, John Carl Camayang, Samji Samira, Montserrat Diaz, Suzana Meira, Eranda Nikolla. "Tuning the Activity of Nanostructured, Non-Precious Metal Oxides for Low Temperature Electrochemical Oxygen Reduction", to be submitted to Nature Catalysis.